



Kent Academic Repository

Walczowski, L.T. (1981) *The low frequency structure of Cassiopeia*. Doctor of Philosophy (PhD) thesis, University of Kent.

Downloaded from

<https://kar.kent.ac.uk/94712/> The University of Kent's Academic Repository KAR

The version of record is available from

This document version

UNSPECIFIED

DOI for this version

Licence for this version

CC BY-NC-ND (Attribution-NonCommercial-NoDerivatives)

Additional information

This thesis has been digitised by EThOS, the British Library digitisation service, for purposes of preservation and dissemination. It was uploaded to KAR on 25 April 2022 in order to hold its content and record within University of Kent systems. It is available Open Access using a Creative Commons Attribution, Non-commercial, No Derivatives (<https://creativecommons.org/licenses/by-nc-nd/4.0/>) licence so that the thesis and its author, can benefit from opportunities for increased readership and citation. This was done in line with University of Kent policies (<https://www.kent.ac.uk/is/strategy/docs/Kent%20Open%20Access%20policy.pdf>). If you ...

Versions of research works

Versions of Record

If this version is the version of record, it is the same as the published version available on the publisher's web site. Cite as the published version.

Author Accepted Manuscripts

If this document is identified as the Author Accepted Manuscript it is the version after peer review but before type setting, copy editing or publisher branding. Cite as Surname, Initial. (Year) 'Title of article'. To be published in *Title of Journal*, Volume and issue numbers [peer-reviewed accepted version]. Available at: DOI or URL (Accessed: date).

Enquiries

If you have questions about this document contact ResearchSupport@kent.ac.uk. Please include the URL of the record in KAR. If you believe that your, or a third party's rights have been compromised through this document please see our [Take Down policy](https://www.kent.ac.uk/guides/kar-the-kent-academic-repository#policies) (available from <https://www.kent.ac.uk/guides/kar-the-kent-academic-repository#policies>).

THE LOW FREQUENCY STRUCTURE OF
CASSIOPEIA A

L.T. WALCZOWSKI

A thesis submitted for the degree of Doctor of
Philosophy of the University of Kent at Canterbury

ABSTRACT

The general structure of the supernova remnant Cassiopeia A is described, with particular reference to the optical jet of fast moving knots, the low frequency anomaly and previous VLBI results. The implementation of a three station interferometer system, measuring the visibility function of the nebula at 38MHz along a mean position angle of 83° , is described; both the closure results and the reconstructed visibility function are presented, from which a significant asymmetry in the source structure is evident. The results are interpreted by Fourier transforming the weighted visibility data, regularly gridded by interpolation of the reconstructed visibility function. The resultant, convolved brightness distribution of the nebula is compared with distributions synthesized to the same resolution, from the results of Jennison and Latham, and Matheson.

A model fitting procedure is described, based on a two component, four parameter model, from which it is concluded that the results are consistent with a symmetrical nebula of radius 135 ± 3 arcsec. with a jet, of indeterminate width, containing between 4% to 6% of the total flux at a distance of 200 ± 20 arcsec. east of the source phase centre.

The remarkable coincidence of the point source solutions of the model fitting procedure with some of Hutton et. al.'s results at slightly higher frequencies is pointed out, and the likelihood of a relationship between the new asymmetrical component and the optical and X-ray jet is commented on. A brief discussion of the astrophysical consequences of the asymmetrical component follows, with reference to a possible association between the jet and the low frequency anomaly.

DEDICATION

To my wife, Elżbieta, without whose patience and understanding this work would never have been completed.

ACKNOWLEDGEMENTS

I would like, above all, to thank Prof. R.C.Jennison for his continual encouragement and enthusiasm throughout the course of this project.

It is also a pleasure to thank Dr. K.L.Smith for the design of both the r.f. and i.f. stages of the basic receiver, and the Staff of the Mechanical Workshop for their help in both the construction and erection of the aerials.

Finally, I would like to acknowledge the kindness of Kent College, Wealden and Woodlands, Mr. G.Gibb and Mr. S.Hutchings for permission to erect outstations on their land.

CONTENTS

CHAPTER 1.	INTRODUCTION	1
1.1	The Radio Source Cassiopeia A	1
	1. General Structure	1
	2. The Optical Jet	3
	3. The Low Frequency Anomaly	5
	4. VLBI Results	8
1.2	Choice of Frequency	9
1.3	Choice of Method	11
PART ONE	- THE THREE STATION INTERFEROMETER SYSTEM	13
CHAPTER 2.	SYSTEM COMPONENTS	13
2.1	Introduction	13
2.2	Aerials	16
	1. The Homestation	16
	2. The Yagi Outstation	16
	3. The Dipole Outstation	18
2.3	Receiver Design	18
	1. The Homestation Receiver	18
	2. The Outstation Receivers	21
2.4	The Radio Links	26
2.5	The Delay Lines	27
2.6	The Multipliers	29

CHAPTER 3.	THE OPERATION OF THE INTERFEROMETER	33
3.1	Measurement of Phase	33
3.2	Measurement of Amplitude	38
3.3	Preliminary Tests	41
1.	Bandwidths	41
2.	Check of Closure Amplitude	44
3.	Check of Closure Phase	44
4.	Check of Cross-Talk between Channels	45
3.4	Sampling of the Visibility Function	47
3.5	The Effect of Interference and Scintillation	53
3.6	Other Tests	53
CHAPTER 4.	ERRORS IN THE MEASUREMENT OF THE VISIBILITY FUNCTION	58
4.1	Introduction	58
4.2	The Cygnus A Effect	59
4.3	The Bandwidth Effect	65
4.4	Other Miscellaneous Errors	69
4.5	Summary of the Sources of Error	71
PART TWO -	THE LOW FREQUENCY STRUCTURE OF CASSIOPEIA A	73
CHAPTER 5.	RESULTS OF THE MEASUREMENT OF THE VISIBILITY FUNCTION	73
5.1	The Results	73
5.2	Reconstruction of the Visibility Function	75
5.3	Application of Fourier Transforms to the Analysis	81

5.4	Comparison with Previous Work	88
CHAPTER 6.	SOME MODEL FITTING	94
6.1	Introduction	94
6.2	The 2-Component, 4-Parameter Model	96
6.3	The Model Fitting Implemented	99
6.4	Mapping based on Closure Data	103
6.5	Mapping based on Reconstructed Visibility Data	111
6.6	Mapping based on Gridded Data	117
6.7	Temporal Limitations of the Present Study	123
CHAPTER 7.	CONCLUSIONS	127
7.1	The Low Frequency Structure of Cassiopeia A	127
7.2	Further Work in Progress	136
APPENDICES		137
APPENDIX 1	Circuit Diagrams	137
APPENDIX 2	Theory of the 2-station Interferometer	144
APPENDIX 3	Fourier Transform Program	148
APPENDIX 4	The Model Fitting Program	150
REFERENCES		172

CHAPTER 1

INTRODUCTION

1.1 THE RADIO SOURCE CASSIOPEIA A

1.1.1 General Structure

The supernova remnant Cassiopeia A (3C 461) is one of the most powerful radio sources in the sky. The optical investigations, originally by Baade and Minkowski (1954) and later those of Van der Bergh and Dodd (1970), Van der Bergh (1971) and Kamper and Van der Bergh (1976) have shown the nebulosity to consist of an incomplete shell of radius approximately 2 arcmin. This shell is composed of two major components: 1) a system of fast moving knots, which on the basis of their abnormal chemical compositions are believed to represent supernova ejecta (Peimbert and Van der Bergh 1971), and 2) a number of quasi-stationary flocculi, possibly composed of matter ejected long before the supernova explosion (Van der Bergh et. al. 1973).

An analysis of the proper motions of the quasi-stationary flocculi has led to an estimate of a time-scale of about 11,000 years to be associated with their expansion, suggesting the possibility of a slowly expanding circumstellar shell (Kamper and Van der Bergh 1976). A similar analysis of the proper motions of the fast moving knots has shown that their expansion can be extrapolated to an origin at the centre of

the remnant, and gives rise to a date for the explosion in the year 1657 ± 3 AD, assuming the ejected mass has suffered little deceleration (Kamper and Van der Bergh 1976).

Recently it has been reported that Flamsteed observed the supernova in 1680 AD (Ashworth 1980), which would support the above assumption. However Kamper (1980) has cast doubt whether Flamsteed did indeed observe the supernova.

The moving knots have lifetimes of the order of a decade (Van der Bergh and Dodd 1970), diameters of approximately 2 arcsec. and comparison of their radial velocities with their proper motions has led to an estimate of about 2.8kpc. for the distance to Cassiopeia A (Van der Bergh 1971). With this estimate, the space velocities of the knots vary from 4,000 to 8,000 kms^{-1} . This range can be contrasted with the expansion velocities of 1,600 and 2,100 kms^{-1} , derived by Dickel and Greisen (1979) for the expansion of the radio shell.

Jennison and Das Gupta (1956) were the first to determine that the radio structure was roughly circular, and Jennison and Latham (1959) showed that the source was limb-brightened. In general, the radio maps of the source e.g. Hogg et. al.'s (1969) at 2.7GHz with a resolution of 8arcsec. by 11 arcsec., Rosenberg's (1970i) at 2.7GHz with a beam 12 arcsec. by 14 arcsec. and Bell et. al.'s (1975) at 5.0GHz with a beam 2 arcsec. by 4 arcsec., all show an incomplete shell with a complex and irregular structure. Rosenberg (1970 i and ii) summarises that most of the observed emission comes from a shell of outer radius 130 arcsec. and thickness 30 arcsec. Surrounding this ring-like structure is a weak plateau of

emission (Bell 1977) which corresponds well with the plateau of emission of outer radius about 170 arcsec. and thickness 30 arcsec. observed in X-ray maps (Murray et. al. 1979).

The many compact features or knots visible on the high frequency radio maps are distributed in a regular way around the shell and amount to about one third the total flux density of the emission (Dickel and Greisen 1979). However there does not seem to be any correlation between these radio knots and the fast moving optical knots and quasi-stationary flocculi, and therefore it may be possible that the optical condensations are caused by substantially different processes compared to the radio features (Dickel and Greisen 1979). In particular, this may be of importance when considering the lack of radio observations associated with the optical jet discussed below.

1.1.2 The Optical Jet

Of particular interest is the distribution of the fast moving knots in which $[SII]$ is strong relative to $[OIII]$ as shown in Fig. 2 of Kamper and Van der Bergh (1976). This distribution shows the emission to arise from two distinct regions: the supernova remnant shell and a jet extending for over 1 arcmin. beyond the shell emission, where in fact the shell itself shows a gap. An analysis of the proper motions of the knots in the jet leads to an explosion date of 1671 AD, the knots outside the shell moving faster than expected (Kamper and Van der Bergh 1976). This prominent optical jet,

originally discovered on the plates of Baade and Minkowski (1954), bears no obvious counterpart on any of the high frequency radio maps (e.g. Hogg et. al. 1969; Dickel and Greisen 1979) although the gap is evident in all of them. However, at approximately the same position angle as the gap, a small, very weak projection is visible on some maps (Ryle et. al. 1965; Strom and Duin 1973 and Rosenberg 1970ii). Whether there is any relationship between the weak projections and the optical jet is open to question and would seem unlikely. For instance, Strom and Duin (1973) observing at a wavelength of 21cm with a beam approximately 25 arcsec. by 29 arcsec., found the projected source to be only partially resolved and elongated north-south rather than east-west as in the case of the optical jet. Attention must also be drawn to the weak +Q feature in the polarization maps of Baldwin et. al. (1970) which coincides with the optical jet and lies 165 arcsec. from the extrapolated centre of expansion of the optical knots.

In general, however, there is no obvious high frequency radio jet associated with the optical flare although it is interesting to note that an area of localized X-ray emission is coincident with the optical jet (Fabian et. al. 1980), emphasizing the strangeness that no such high frequency jet has been discovered. The latter association is not surprising since there is a general correlation over the whole remnant between the X-ray emission and the fast moving knots in which [SII] is strong relative to [OIII] (Murray et. al. 1979).

To add to the confusion, Jennison and Latham (1959),

observing at 127MHz along an east-west baseline, reported a brightness distribution consisting of a limb-brightened disc 4.1 arcmin. across with a spur to the east about 4 arcmin. in length. The contribution of the spur to the total flux density at 127MHz was estimated at about 10 to 15%, which incidently can be compared with the 0.2% contribution of the weak projection coincident with one of the fast knots in the optical jet reported by Rosenberg (1970ii) at a frequency of 5.0GHz. Unless the radio jet should have a secular variability, it would appear necessary to postulate a source with a very steep spectrum to explain the observed results.

The only other unambiguous attempt to determine the low frequency structure of Cassiopeia A, by measuring both the phase and amplitude of the visibility function, was that of Matheson's (1974) who, observing at a position angle of 75° at 150MHz, found his results were consistent with a spur of not more than 2% of the total flux density. He concluded that the spur had either decayed considerably or that Jennison and Latham's interpretation was not justified.

1.1.3 The Low Frequency Anomaly

The radio spectrum of Cassiopeia A has been well established, in particular by the work of Baars and Hartsuijker (1972) and that of Baars et. al. (1977). The earlier work is the first to take note of the frequency dependence in the secular decrease of flux density, and the latter, taking

account of this dependence establishes the spectrum to an accuracy of 2%. However the derived spectrum cannot be used at frequencies below about 50MHz, due to the low frequency anomaly described below.

It was in 1975 that Erickson and Perley reported an unexpectedly high flux density at 38MHz, compared with Parker's determination in 1966 extrapolated to 1974 by applying the secular decrease correction of 1.29% per year determined by Scott et. al. (1969). This low frequency anomaly was confirmed by Read (1977i) who also found, on making further measurements a year later, that the flux density was significantly lower than the two previous values, indicating a time-scale of 2 to 6 years for the low frequency variability of the emitting region (Read 1977ii).

The reasons for the anomaly are still very much uncertain and several models for the supernova remnant have been suggested which attempt an explanation of its anomalous low frequency behaviour. Most of these models include some form of particle injection and/or acceleration. Peterson's model postulates a central pulsar with an injection of particles with a non-power law spectrum of energies (Peterson 1976). However no stellar remnant has so far been detected near the centre of expansion (Kamper and Van der Bergh 1976) nor have any of the pulsar searches proved positive: neither in the radio band (Davies and Large 1970; Reifenstein et. al. 1969), the optical band (Horowitz et. al. 1971) nor the X-ray band (Holt et. al. 1973). In particular no point source of soft X-ray radiation has been detected (Murray et. al. 1979),

although a neutron star, if it had formed, could not have cooled down to less than $3 \times 10^6 \text{K}$ in 300 years (Shklovsky 1979). In view of the above it would seem rather exotic to accept Peterson's model in preference to either Fedorenko's (1979) based on the acceleration of particles due to Alfvén waves, which concludes with a possible pulsation of the flux density at low frequencies with a period of 2 to 6 years (hence the anomaly), or, that of Chevalier et. al. (1978) based on adiabatic expansion losses, continuous second order Fermi-acceleration and a variable relativistic particle injection. However, the model presented by Chevalier et. al. seems inconsistent with the rapid decrease of the flux density reported by Read (1977 i and ii) after the initial increase (Erickson and Perley 1975). Nevertheless all three models do explain the frequency dependence of the secular decrease of the radio emission which, in fact, is the normal result of stochastic acceleration processes (Cowsik 1979) which must be present in some form or other in the shell.

It should also be noted that the low frequency anomaly is not the first instance of decametric variability that has been detected in the source. One previous study by Braude et. al. (1969) has also indicated severe low frequency changes in Cassiopeia A, of the order of 2.5db at 12.5MHz. However these results have been questioned by Bridle and Caswell (1970) who report that the short period variations of about 2 to 3 months observed by Braude et. al., were due to ionospheric effects. Another study, monitoring the flux density at 26.3MHz, has provided further evidence that there is no systematic variation over a period of a few months to

within 3.5% RMS deviation of the flux density (Viner 1975). However, by comparing the Cassiopeia A to Cygnus A flux density ratio derived by Erickson and Perley (1975) to that derived by Read (1977ii) thirty months later, a decrease in flux density of just under 1% per month can be calculated, suggesting that the low frequency anomaly would not have been detected in the work of Viner.

1.1.4 VLBI Results

A number of attempts have been made at low frequencies to detect fine structure in Cassiopeia A by VLBI observations. The attempts by Slee and Wraith (1967) at 38MHz with a baseline of approximately $15,000\lambda$, giving a lobe spacing of the order of 14 arcsec. and by Erickson et. al. (1972) at 121.6MHz with a baseline of $92,000\lambda$ (2.2 arcsec. lobe separation) did not detect fringes. In a high resolution study at 26.3MHz with a baseline of $22,000\lambda$ (9.38 arcsec. lobe separation), fringes were detected by Hutton et. al. (1973), with the interpretation that either the fringes arose from the same structure of compact features observed at higher frequencies, or that a single compact source with a very steep spectrum had been observed. A further study by Hutton et. al. (1974) seemed to confirm the possibility of a compact source. Observing at two frequencies, 74MHz with a $12,000\lambda$ baseline and 111MHz with a $18,500\lambda$ baseline, Hutton et. al. found the fringe amplitudes to vary strongly on a time-scale of 15 to 30 minutes. By comparing their visibility curves with visibility curves generated by

computer 'observation' of the high frequency radio map of Hogg et. al. (1969), Hutton et. al. were able to conclude that their results were consistent with higher frequency observations plus one other compact source. Due to poor (u,v) plane coverage they could not isolate the location of the extra source unambiguously, but suggested that it had to lie outside the shell, possibly north of the shell or, coincident with the optical jet outside the gap. Hutton et.al. limited the flux density of the compact source to less than 10% of the total flux density and suggested it had a very steep spectrum with spectral index about -2.5.

However, the above interpretation has been queried by Bell and Gull (Read 1977i), who suggest that the postulation of an extra compact source is unnecessary and the difference in interpretation is due to the poor (u,v) plane coverage of the 2.7GHz map of Hogg et. al., used by Hutton et. al. in their analysis.

1.2 CHOICE OF FREQUENCY

With the many interesting results of previous determinations of Cassiopeia A's structure, including, the low frequency anomaly (Erickson and Perley 1975), the possibility of a compact source with a steep spectral index (Hutton et.al. 1974), the absence of a high frequency jet where there exists an optical flare (Minkowski 1959) and the possibility of a low frequency spur (Jennison and Latham 1957), it was decided to investigate the structure of the source and, in

particular, search for any asymmetry, at a low frequency.

The preliminary equipment included a variable frequency receiver to test for interference free bands in the range 30 to 100MHz. The aerial used was the 30m paraboloid dish mounted above the Electronics Laboratories, illuminated by suitable Yagi feeds. Unfortunately at these low frequencies it was found that the dish aerial, constructed of chicken mesh, did not screen the feed from the interference generated by the computer in the laboratory below. Hence, for the duration of the preliminary tests the computer was switched off. In particular, two frequencies were investigated, 78.8MHz and 38.0MHz, both of which were found to be reasonably free of interference (but not entirely so).

The absence of any structural information on the source at 38MHz and the fact that an asymmetrical component of steep spectral index, if such a source existed, would be that much more detectable at 38MHz, governed the final choice of receiving frequency.

One effect, further referred to in Section 3.5, which was not noticed in the preliminary tests, was the interference received at 38MHz due to reflection of man-made signals in the F2 layer of the ionosphere. Had the 78.8MHz band been chosen, it is very likely that the percentage of analysable runs would have been greater.

1.3 CHOICE OF METHOD

The work presently described attempted to determine the complex visibility structure of Cassiopeia A at 38MHz along a position angle of approximately 80° , since the structure of a radio source can only be determined unambiguously by measuring both the amplitude and phase of the visibility function. In principle the data can then be Fourier transformed and the brightness distribution derived, though in reality this is rather difficult since the sampling in baseline space may be irregular and the component visibilities measured only up to some maximum value of baseline, n_{\max} . Even if the sampling is regular, the calculated brightness distribution is still a convolution of the true brightness distribution with a beam of width $1/n_{\max}$ radians, with grating sidelobes spaced $1/n_{\text{int}}$ radians from the map phase centre, where n_{int} is the interval in wavelengths between consecutive samples of the spatial-frequency spectrum (e.g. Bracewell 1958; Swenson 1969). The problems of data reduction are further considered in Chapters 5 and 6.

The method adopted to map the visibility function was originally described by Jennison (1953, 1958) and Latham (1957). Low frequency interferometric visibility data tends to suffer greatly from 1) large systematic amplitude errors due to ionospheric scintillation, variations and uncertainties in aerial gains, and variations in receiver gain; and 2) large phase errors due to ionospheric irregularities, receiver instabilities and oscillator drifts, particularly if radio links are used to transmit data from one station to another.

The method developed by Jennison and Latham, originally called the triple interferometer method, uses three aerials forming three simultaneous baselines, and sums the resultant data in a loop such that all systematic phase and amplitude errors and uncertainties cancel (as summarised for completeness in Sections 3.1 and 3.2).

Now referred to as the closure visibility method, the triple interferometer system was used by Twiss et. al. (1960 and 1962) and by Matheson (1974) in the field of radio astronomy and by Rogstad (1968) and Rhodes and Goodman (1973) in optics. Since then closure phase has been widely applied in the analysis of VLBI observations (e.g. Rogers et. al. 1974; Wittels et. al. 1976 and Wilkinson et. al. 1979). Recently the inclusion of closure amplitude methods in the analysis of VLBI observations has been suggested by Readhead et. al. (1980) who base their method on that adopted by Twiss et. al. employing four telescopes. The closure visibility is then formed around a quadrilateral (c.f. the analysis of Chapter 3) and is given by:

$$A_{pqrs} = \frac{V(\underline{b}_{pq}) V^*(\underline{b}_{rs})}{V(\underline{b}_{pr}) V^*(\underline{b}_{qs})} \quad (1.1)$$

.....from Readhead et. al. (1980)

where $V(\underline{b}_{ij})$ is the complex visibility for a baseline between telescopes i and j .

PART ONE

THE THREE STATION INTERFEROMETER SYSTEM

CHAPTER 2

SYSTEM COMPONENTS

2.1 INTRODUCTION

The basic structure of the triple interferometer system is outlined in Fig. 2.1. A base-station, consisting of a large fixed array of dipoles linked to the Electronics Laboratories by cable, and two outstations, linked by radio, formed the basis of three colinear interferometer pairs, the outputs of which were registered on a three-pen chart recorder to facilitate analysis of the fringes.

Fundamentally each receiving channel consisted of a superheterodyne receiver with an i.f. of 10.7MHz, the output of which was fed into buffer amplifiers, through suitable delays which compensated for differences in the time of travel from each station to the laboratory. However, because of the need to preserve coherence between each channel, the structure of the two outstations was modified such that the radio-link carried the corresponding outstation oscillator signal, as well as the signal caused by source radiation,

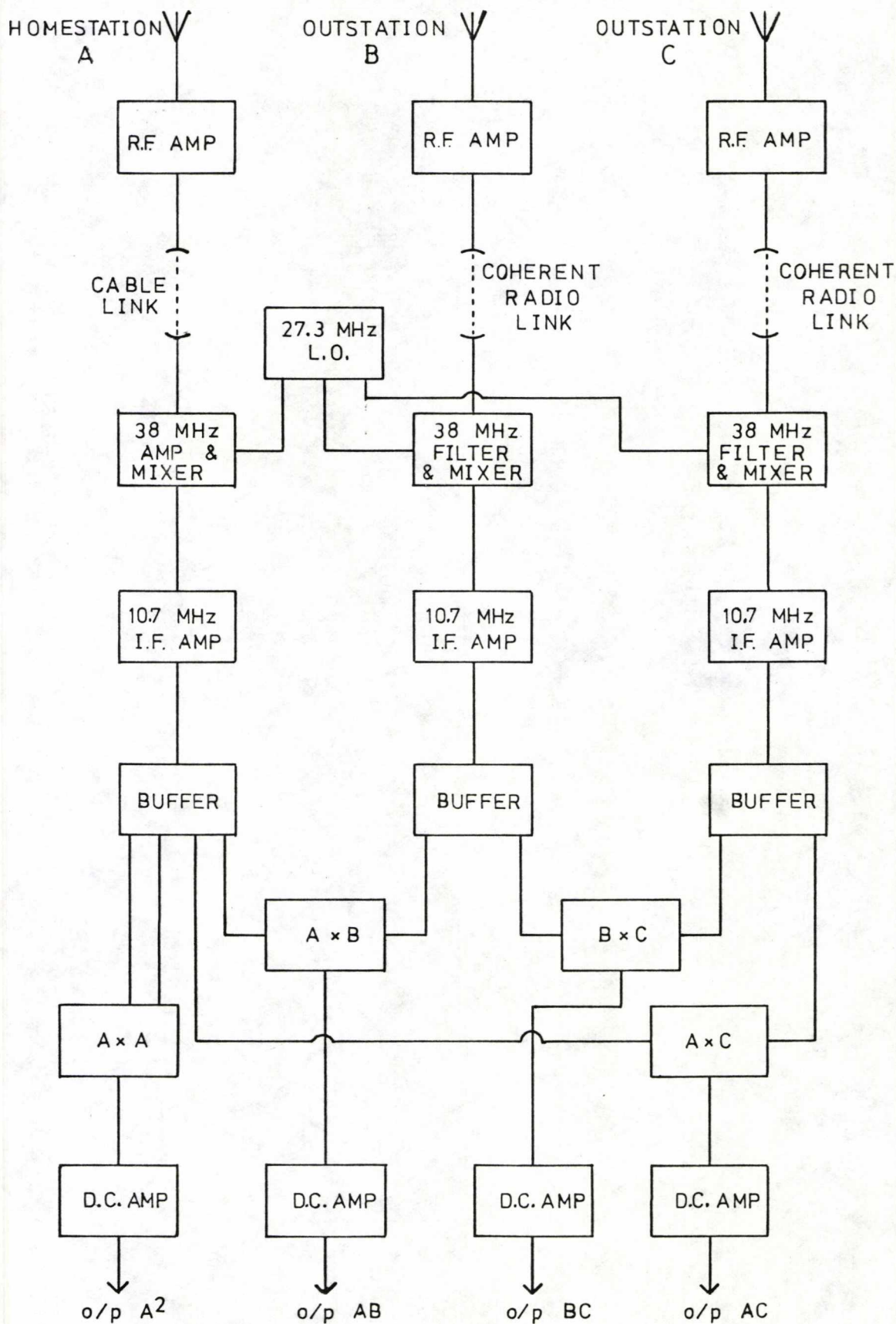


FIG 2.1 Schematic Diagram Of The Triple Interferometer System

enabling the latter to be reconstructed coherently in the laboratory.

The buffer amplifiers, consisting of emitter follower devices, provided outputs which were correlated in pairs in three multipliers. Two extra outputs provided on the base-station buffer, were also correlated to produce a total power output necessary for closure amplitude.

The output from each multiplier was fed to an integrator and d.c. amplifier, each consisting of a 741 operational amplifier and peripheral circuitry similar to the circuit used by Matheson (1973). Integration constants used were of the order of 1 second for the fringe outputs and 10 seconds for the total power output. The longer constant in the latter case facilitated analysis of the recorded output since the effect of very fast scintillations tended to be smoothed out. The total power output was displayed on a Vitatron UR401 pen recorder, whilst the three interferometer outputs were displayed on a JJ CR503 triple pen recorder. The automatic switching on and off of the CR503, during the transit of Cassiopeia A, triggered a relay which produced calibration marks on the output of the UR401 pen recorder such that synchronisation of the two charts was possible.

2.2 AERIALS

2.2.1 The Homestation

The homestation array was situated approximately 220m from the Electronics Laboratories, in a field specifically used for aerial assemblies. The homestation antenna, necessarily a permanent installation, consisted of one broadside array of eighteen horizontal full-wave dipoles arranged in an east-west direction. Each dipole was separated by a distance of $\lambda/2$ from the next and approximately $\lambda/6$ from the ground reflector plane. The array was connected by 75Ω low-loss cable (URM203) to the "aerial hut" where a pre-amplifier was located.

For a uniform linear aperture field distribution, the half-power beam width is given by $51^\circ/L_\lambda$ (e.g. Krauss 1966) where L_λ is the length of the aperture in wavelengths. Therefore:

$$\text{HPBW} = 51^\circ / 9 = 5.67^\circ$$

Hence the array had half power beam widths of approximately 6° in right ascension and 120° in declination, which corresponded to a transit time of 1hr 26min between nulls for Cassiopeia A.

2.2.2 The Yagi Outstation

Two semi-permanent outstations were necessary for 1) testing the system and 2) short baseline work. These needed

to be strong and reliable, and above all, have a good land area to gain ratio since the sites available, surrounding the laboratory, were of minimal dimensions.

In view of the above, a square array of four Yagis was used, the dimensions and spacings of the four elements of each Yagi scaled up in size from similar Yagi aeriels of higher frequency (Evans and Jessop 1976). Final adjustments on the Yagi design were performed by altering the spacings between each of the parasitic elements until an impedance of 50Ω was observed on an impedance bridge at the end of the 4:1 impedance step-down coaxial balun feeder. The final Yagi dimensions are as tabulated below in Table 2.1.

Element	Length	Spacing
1st director	3.43m (0.44 λ)	1.68m (0.21 λ)
2nd director	3.33m (0.42 λ)	
Folded dipole	3.66m (0.46 λ)	1.22m (0.15 λ)
Reflector	4.17m (0.53 λ)	1.98m (0.25 λ)

TABLE 2.1 : Yagi Specification

Since the gain, G , of a simple 4-element Yagi is approximately 7db relative to a half-wave dipole, its capture area is given by:

$$A_e = \frac{3}{2} \frac{\lambda^2}{4\pi} G \approx 37.15\text{m}^2$$

Hence the optimum spacing between each Yagi, such that their capture areas do not overlap, was calculated to be approximately

6m. Cassiopeia A was found to transit between nulls for approximately 8 hours, corresponding to a half-power beamwidth of 32° in right ascension.

2.2.3 The Dipole Outstation

For the longer baselines, with sites situated on private land, a compact, easily portable antenna system was desirable. Hence a broadside array of four full-wave dipoles, similar to the base-station, was used. The array had a half-power beamwidth of approximately 25.5° corresponding to a Cassiopeia A transit between nulls of 6 hours 25 minutes.

Because of the width of the main lobe, great care was taken to ascertain the effect on the results of the sidelobe which lay on the source Cygnus A during a meridian transit of Cassiopeia A. This effect, only of significance in the output of two dipole outstations correlated together, is considered in Section 4.2.

2.3 RECEIVER DESIGN

2.3.1 The Homestation Receiver

Several designs for the basic superheterodyne receiver were considered, and finally a design suggested by Dr. K.L. Smith (private communication) based on low noise, dual-gate mosfets was chosen for the r.f., mixer and i.f. stages.

A schematic diagram of the homestation is displayed in Fig. 2.2. A 38MHz preamplifier, connected to the fixed array, employing two dual-gate mosfets and five tuning coils was constructed and tuned to give a rectangular stop-band of width 1MHz centered on 38MHz. The gain of the unit was set to 45 db, by applying a constant 1.1V to the gain control line. A similar unit was placed in the Electronics Laboratories, to which the first preamplifier was connected by 220m of cable of velocity factor 0.66, giving a delay of 1.08 μ sec relative to the fixed array. Constructed within the unit was a mixer employing a third dual-gate mosfet, particularly suitable due to the near square-law characteristics of the device and almost 20db conversion gain. The stop-band of the unit was tuned to give a rectangular band-pass of width 480kHz, and the gain was found to vary from 29 to 54 db, depending on the value of the small voltage applied to the gain control line.

The 27.3MHz crystal oscillator, situated at the base-station, was buffered by emitter followers to produce three isolated outputs feeding each of the receiving channels. The output of the mixer was connected by suitable delays to the 10.7MHz i.f. amplifier which defined the overall bandwidth of the interferometer system. The bell-shaped response of the i.f. amplifier was governed by the TOKO BBR 3132A 6 pole linear phase filter (3db bandwidth : 240kHz) and four TOKO KALS 4520 10.7MHz i.f. transformers, which reduced the bandwidth to approximately 110kHz. Similar to the preamplifiers, gain was provided by four dual-gate mosfets, the first of which buffered the linear phase filter. Gain was varied by

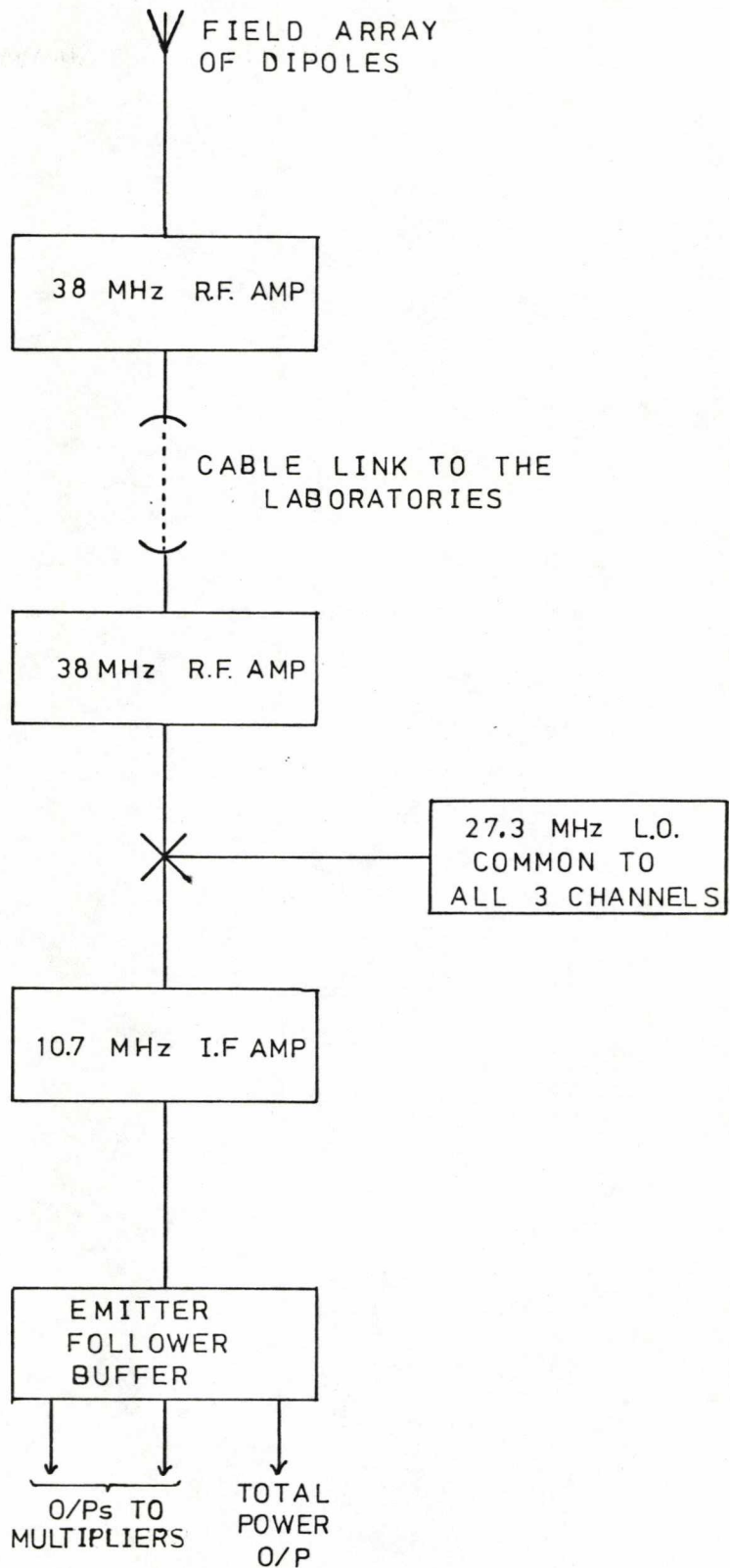


FIG. 2.2

Schematic Diagram Of The
Homestation Receiver

by the application of a small voltage, between 0 and 1V, to the gain control line.

The bandwidth of the system was reduced to that defined by the linear phase filters primarily for two reasons. Firstly, so that the coherence time, inversely proportional to the bandwidth, would be as long as possible within limits set by signal to noise considerations, and secondly, tests had shown a number of interfering signals very close to the 38MHz receiving frequency. To reduce the probability of significant interference, the stop-band of each receiver was designed to give at least 70db attenuation at frequencies 400kHz either side of 38MHz. The overall response of the homestation receiver is illustrated in Fig. 2.3.

Latham (1957) shows that if the bandwidths of the channels are not identical, false results are obtained. To facilitate identical tuning of the i.f. amplifiers each of the four tuning coils was slug tuned until maximum output of the unit was observed on the polyscope. It was found that this method did indeed give the required bandwidth of 110kHz and minimum bandwidth deviation between the three channels as illustrated in Section 3.3.1.

2.3.2 The Outstation Receivers

It was mentioned in Section 2.1 that the structure of the basic receiver was modified to preserve coherence. For the two outstation channels, the r.f. stage and i.f. stage

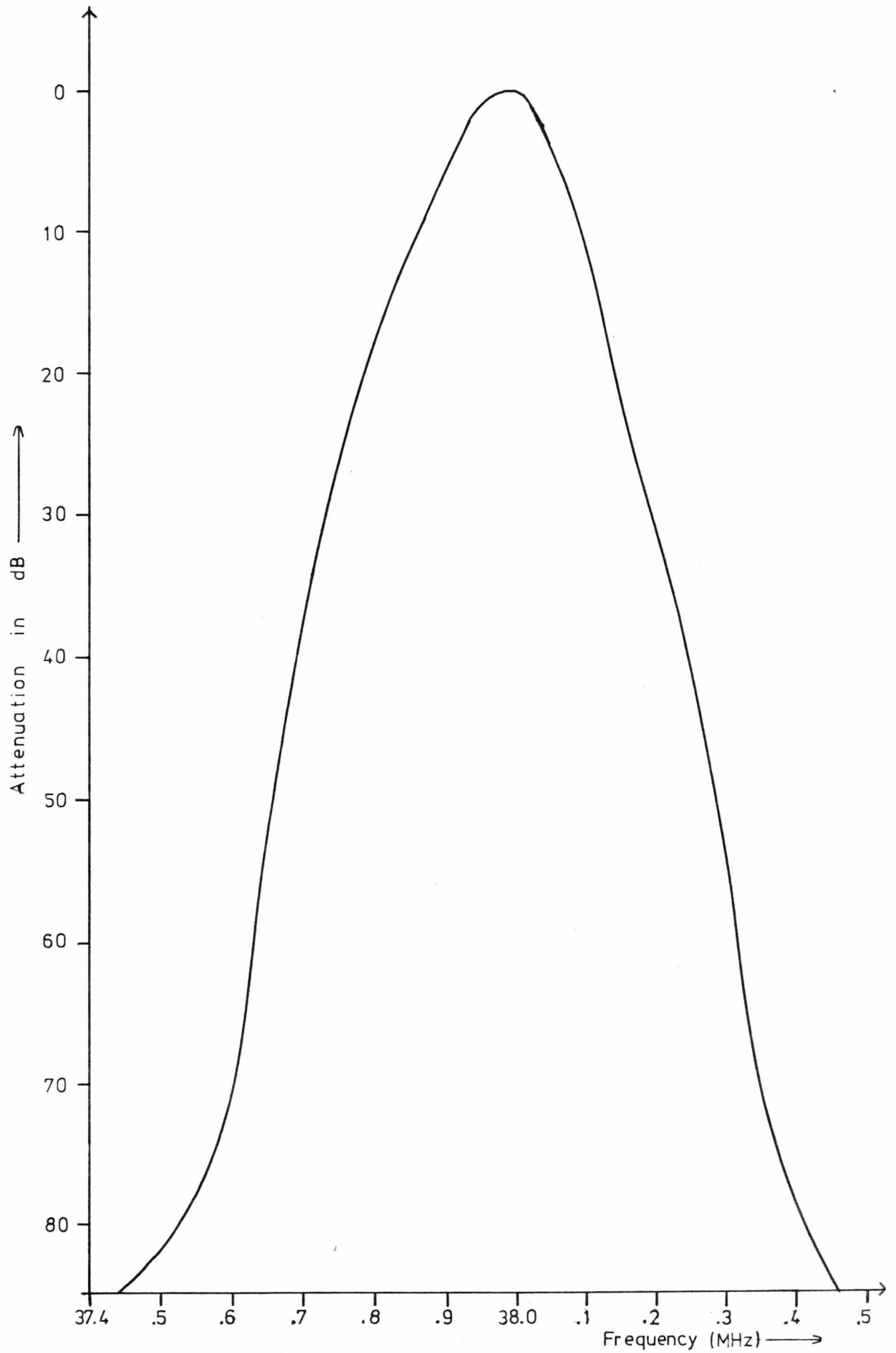


FIG 2.3 Overall Response Of The Homestation

were separated and a new crystal oscillator frequency introduced, 27.095MHz and 27.045MHz for the two stations respectively. The corresponding output from each mixer was connected to a wide-band i.f. amplifier, two Plessey SL560C integrated circuits cascaded together in 50Ω line driver modes. The output of each amplifier was used to frequency modulate a radio link broadcasting to the top of the Electronics Laboratories. To be able to coherently reproduce the signal caused by source radiation, the oscillator signal was connected to a buffer amplifier and also used to modulate the radio link. The overall gains of the outstation receivers were measured to be 85 and 87 db for the two outstations respectively, the r.f. gain control set to a maximum of 1.5V in both cases.

The signal received at the Laboratories was passed to a filter chain which provided two outputs : the original i.f. and oscillator signals reproduced. The filter chain was designed to separate the input into its two component parts with as little attenuation as possible and reproduce the oscillator frequency cleanly. To further the latter aim, a simple crystal filter was employed. Unfortunately, in the case of outstation B the two crystals did not align as well as was hoped for and an attenuation of 8db resulted compared with 3db for the second outstation channel. A summary of the filter chain performance is tabulated in Table 2.2 below.

Due to the bad performance of the link at frequencies above 14MHz, the oscillator signal had to be boosted by a narrow bandwidth amplifier, to a level high enough to drive

	Outstation A	Outstation B
Insertion loss : i.f. port	0.5db	0.5db
Insertion loss : L.O. port	8.0db	3.0db
L.O. - i.f. port isolation	66db	66db
i.f. - L.O. port isolation	60db	55db

TABLE 2.2 : Radio Link o/p Filter Specification

a double balanced mixer. A Texas Instruments SN76514, similar to the devices used in the multipliers, was used to coherently reproduce the original 38MHz signal.

The signal thus coherently reconstituted in the hut at the top of the Electronics Laboratories, was passed by cable to the temperature stabilised control room in the heart of the laboratories, where the rest of the system was situated. The remainder of each outstation channel consisted of a 38MHz filter and mixer assembly driven by the common 27.3MHz buffered crystal oscillator, and the corresponding i.f. amplifier, identical to that of the base-station.

The basic structure of each outstation is summarised in the schematic diagram of Fig. 2.4.

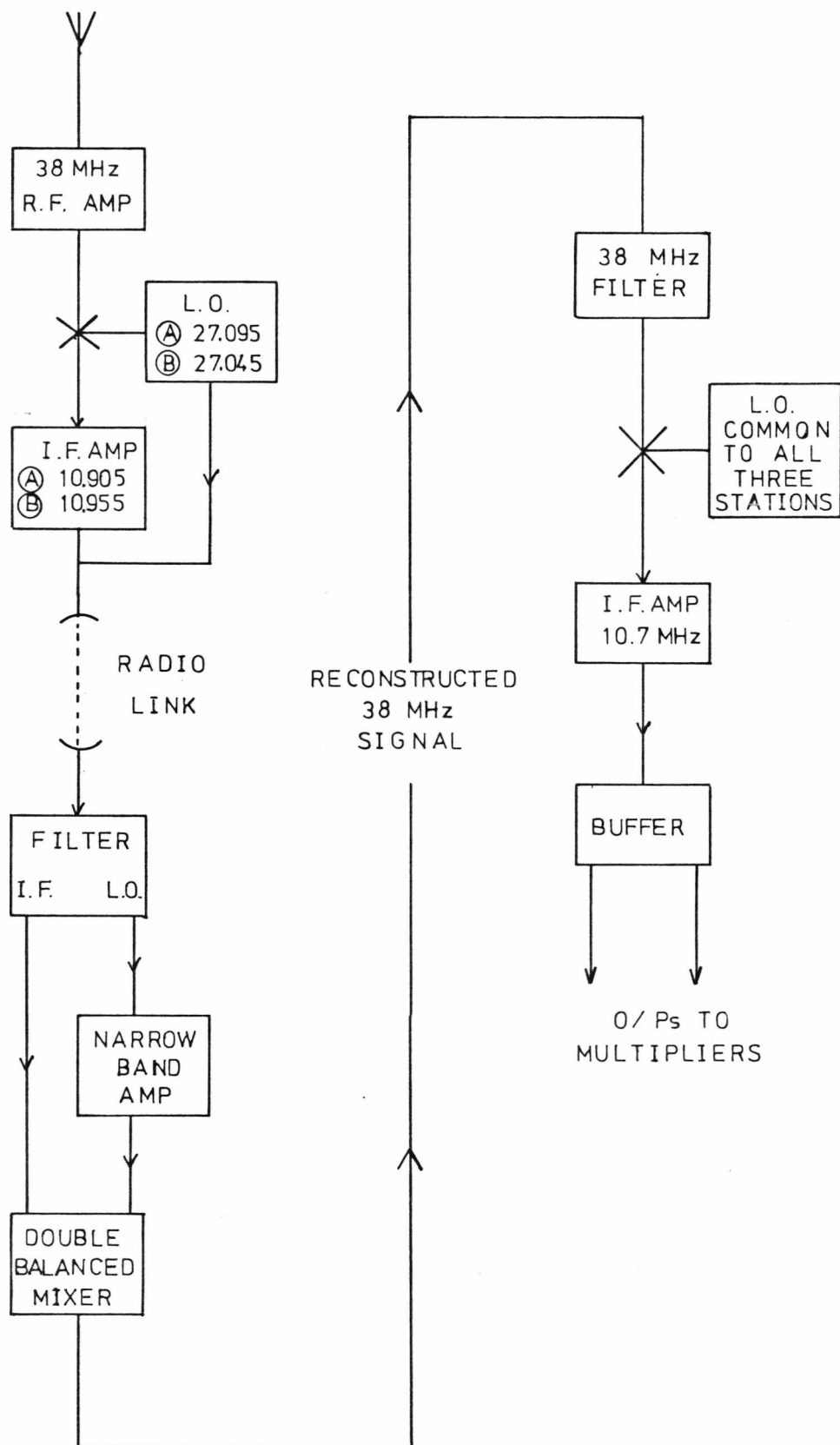


FIG. 2.4 Schematic Diagram Of An Outstation

2.4 THE RADIO LINKS

Two Microwave Associates MA-13CP portable FM microwave links operating at 12,940.5MHz and 13,206.5MHz respectively, were used to transmit the received signals at the outstations back to the Electronics Laboratories. Each system employed a horn antenna of gain 18db at the transmitter end and a 1.22m dish of gain 41db mounted at the top of the laboratories. Both transmitters had a power output rated at 17dbm, giving the links ranges of about 32km for a 10db fade margin to 33db S/N.

Because of the nature of the countryside surrounding the laboratories, mainly large expanses of tall woodland, two 18.5m masts, manufactured by C & S Antennas, were used to mount each transmitter. The outstation dipole array could then be erected carefully next to the mast.

Pointing of the transmitter did not present any problem, since the half-power beamwidth of the horn antenna was of the order of 19° , whereas the location of the Electronics Laboratories was known to within 1° from Ordnance Survey maps. Pointing of the 1.22m paraboloid dish antenna was a somewhat greater problem due to the narrowness of the beam, 1.3° . For approximate pointing, the dish was swept horizontally and vertically using the coarse adjustment on the dish mounting, until a signal had been detected, as indicated on the meter fixed to the receiver front panel. The signal level was then optimized by turning the fine adjustment screws until a maximum, steady deflection was observed.

The transmitter was powered by a 48V Gell/cell battery which needed recharging after 4 hours operation. A digital sidereal clock was used to switch a 12V battery that operated both the outstation receiver and a relay which in turn performed the switching of the 48V battery. The on time could be regulated to any time up to 40 minutes in 5 minute steps, but was usually set at half an hour providing a series of 8 consecutive runs before the 48V battery needed recharging.

Since the MA-13CP was specifically designed for outside broadcast television work, care was taken to ensure that the video frequency response was reasonable at the outstation receiver i.f. of just below 11MHz. In fact, the response of the radio link was found to be flat up to 10MHz and 2db down at 11MHz, with the gain varying by only 0.2db across the i.f. band of the outstation. Hence dispersion effects due to the radio link were considered negligible. The response at the outstation oscillator frequencies of 27.095 and 27.045 MHz respectively was found to be 57db down. However, using a crystal filter and amplifier, a noise free oscillator signal could still be reconstituted.

2.5 THE DELAY LINES

At an i.f of 10.7MHz and for moderate baselines up to about 6.5km, it was decided that cable delay lines would be satisfactory, although this required rather long lengths of cable in the control room. The greatest effect of using such

long lines was the variation of the response of the total power channel with temperature, which by virtue of being the home channel always needed the greatest delay. To remove this effect, noted to be a variation of $0.3\text{db}/^{\circ}\text{C}$, the control room was temperature stabilised to a steady 26.6°C regulated to within an estimated 0.1°C by a thermistor controlling the temperature balance of the heating system. This produced a net temperature effect in the total power channel of $0.015\text{db}/^{\circ}\text{C}$ for a total cable delay of $13\mu\text{sec}$, a twentyfold improvement in performance.

Two types of cable were available for use as delay lines, both of characteristic impedance 75Ω . For most baselines URM 203 cable, velocity ratio 0.78 and attenuation $2.5\text{db}/100\text{m}$ at 10.7MHz , was found suitable. At longer baselines, the extra delay was made up using BICC T3116 cable, velocity ratio 0.845 and attenuation $2.2\text{db}/100\text{m}$ at 10.7MHz .

To counter the effect of the considerable attenuation, as much as 110db for a 715λ baseline, Plessey SL560C integrated circuits operating in line driver modes were placed at intervals of 500m along the length of delay line. Since each such unit was measured to have a gain of the order of 12db , only a small proportion of the attenuation had to be made up using the gain control of the i.f. amplifier.

The lengths of delay line necessary to equalize the propagation delay over the three paths to the multiplier units, were calculated from Ordnance Survey maps, due

allowance being made for the various cables connecting apparatus together. It was estimated that such calculations were accurate to better than 100nsec, equivalent to a cable length of approximately 25m. The propagation delays are summarised in Section 3.4 and the effect of a differential time delay error between two limbs of the interferometer is considered in Section 4.4.

2.6 THE MULTIPLIERS

Since all the results depend on the accuracy of the multiplier's performance, particular care has to be taken to ensure a device with negligible spurious correlation and good linearity is used. Hence in designing an analogue multiplier, attention has to be paid to carefully matching the components. Since this can be somewhat time consuming a multiplier system based on an integrated circuit was investigated. Initially the RCA CA3091D four quadrant multiplier was tested and found to satisfy the above criteria. Now the transfer characteristic of the device is given by:

$$V_{\text{out}} = .1 V_x V_y$$

where V_x and V_y are the input voltages. Since the emitter follower buffers could only be driven before limiting to give output voltages of the order of 300mV rms, it was clear that at most a 9mV multiplier output would be available - of the same order as the noise level of the device itself. Hence the device was replaced by a system utilising a Texas

Instruments SN76514 double balanced mixer. The transfer characteristic of the device is:

$$V_{\text{out}} = K_1 V_x \tanh K_2 V_y$$

where K_1 and K_2 are constants (Norris 1976). Thus for small values of V_y the device acts as a linear analogue multiplier.

The peripheral circuitry around the device was based on that suggested by Norris (1976). However, for the differential output to be referenced to a nominal 0V for no signal input, the supply voltages were altered to levels around +3.6V on pin2 and -10.0V on pin6 until a reasonable balance occurred.

To guarantee as little differential phase delay as possible between input ports, the impedance of the six inputs of the three correlators was measured using an impedance bridge and a resistor/inductor parallel network connected to earth on the higher impedance port of each multiplier until all ports showed similar impedances of 80Ω in parallel to 45pf.

The non-inverted output of the multiplier was connected to an inverting d.c. amplifier, the gain of which was adjusted until both the multiplier outputs were identical for a calibrating input signal. This had the effect of cancelling the d.c. drift of the output with temperature variations. The two outputs, both negative with respect to earth, were then inverted in a second d.c. amplifier of gain x2.

A check of the linearity of the final multiplier system was performed by testing the unit as a square-law detector. The two input ports were connected together and a 10.7MHz signal, monitored on an oscilloscope of 200MHz bandwidth, was injected. The output was registered on a digital voltmeter. Each unit was found to be linear for input voltages in excess of 200mV p-p. The linearity of unit AxB is plotted in the graph reproduced in Fig. 2.5.

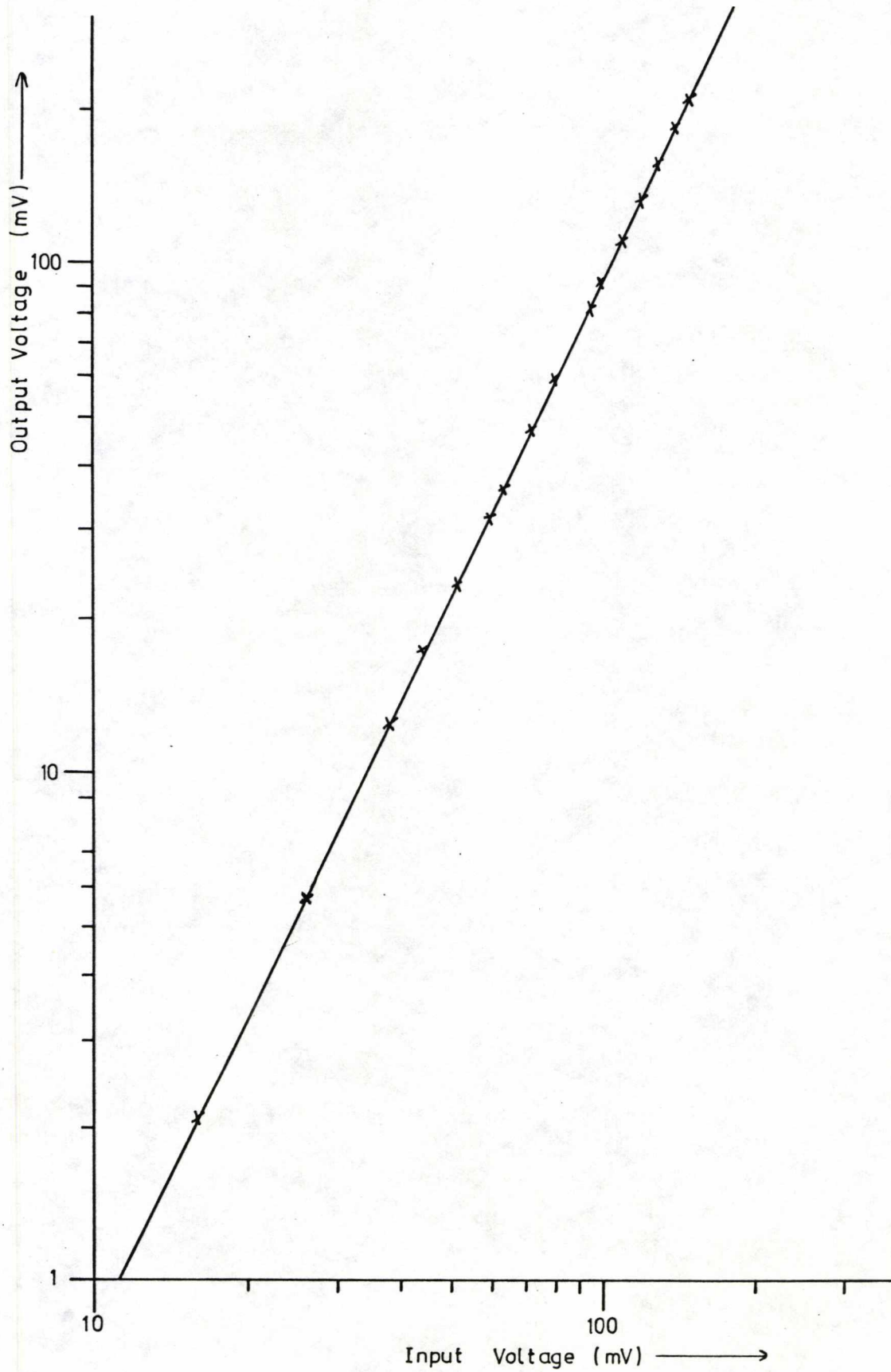


FIG. 2.5 Linearity Of Multiplier Unit $A \times B$

CHAPTER 3

THE OPERATION OF THE INTERFEROMETER

3.1 MEASUREMENT OF PHASE

Referring to Appendix 2, where a brief theory of the two station interferometer is presented, equation (A2.5) can be rewritten:

$$R_k(t) = g_k A_i A_j F(n_{ij}) \cos [2\pi n_{ij} \cos \delta \sin h - 2\pi \nu \tau_k - \psi_i + \psi_j + \Psi(n_{ij})] \quad (3.1)$$

where $R_k(t)$ = output of the k-th interferometer,
 g_k = multiplier constant of the k-th interferometer,
 A_i, A_j = constants representing aerial and receiver gains of the i-th and j-th receivers,
 n_{ij} = baseline length in wavelengths,
 δ, h = declination and hour angle of the source,
 τ_k = error in equalizing the time delays,
 ψ_i, ψ_j = phase errors in each limb of the interferometer,
 $F(n_{ij})$ = amplitude of the visibility function,
 and $\Psi(n_{ij})$ = phase of the visibility function.

Considering three colinear East-West stations, as in the three station interferometer, three outputs result:

$$R_{12} = g_1 A_1 A_2 F(n_{12}) \cos [2\pi n_{12} \cos \delta \sin h - 2\pi \nu (\tau_2 - \tau_1) - \psi_1 + \psi_2 + \Psi(n_{12})] \quad (3.2)$$

$$R_{23} = g_2 A_2 A_3 F(n_{23}) \cos [2\pi n_{23} \cos \delta \sin h - 2\pi \nu (\tau_3 - \tau_2) - \psi_2 + \psi_3 + \Psi(n_{23})] \quad (3.3)$$

$$R_{13} = g_3 A_1 A_3 F(n_{13}) \cos [2\pi n_{13} \cos \delta \sinh - 2\pi \nu (\tau_3 - \tau_1) - \psi_1 + \psi_3 + \Psi(n_{13})] \quad (3.4)$$

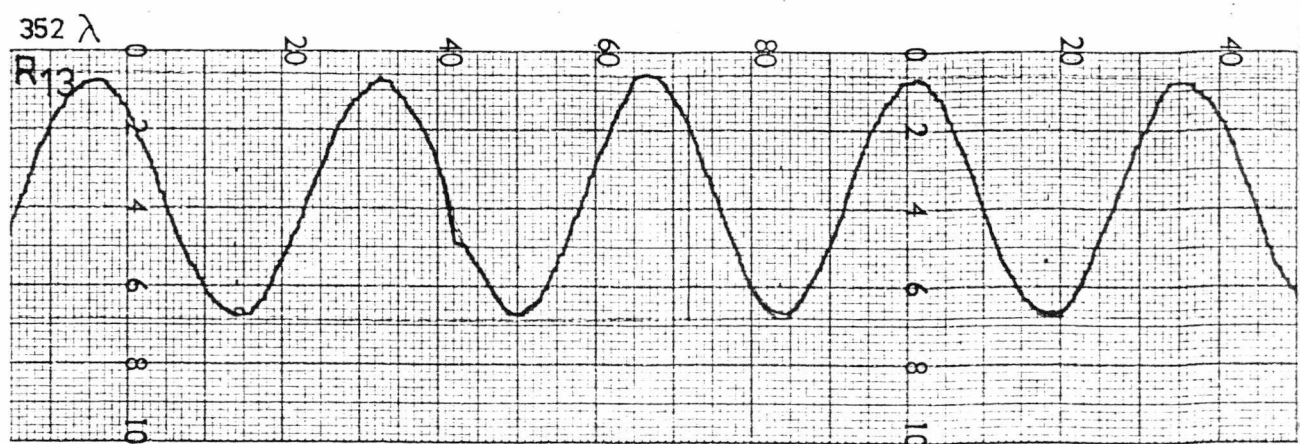
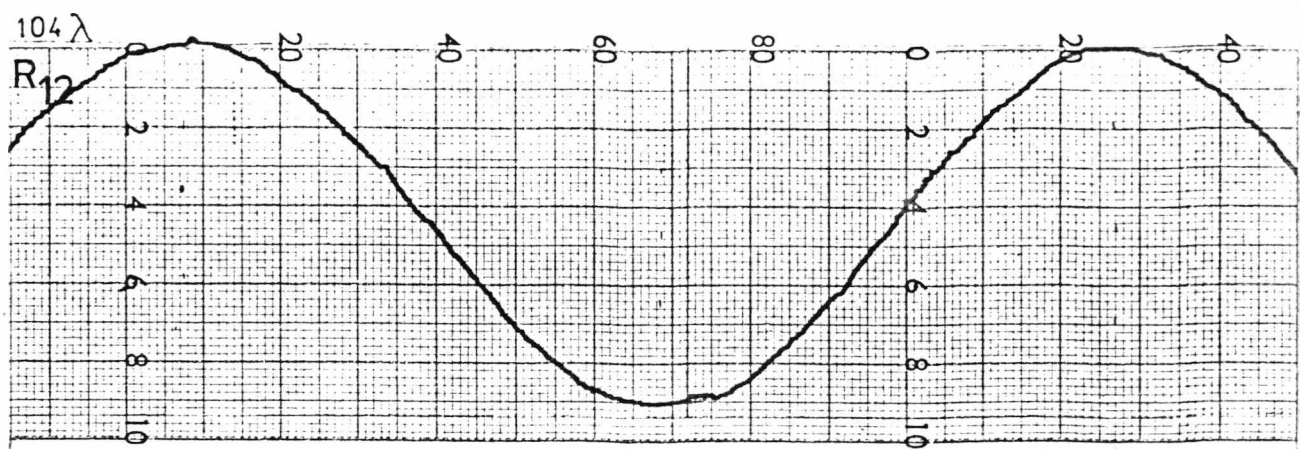
Figs. 3.1 and 3.2 illustrate typical runs as defined by the three equations. Jennison (1953 and 1958) and Latham (1957) have shown that there exists a closure phase relationship between baselines which is independent of all phase errors in each channel. This relationship can be represented by Ψ_{123} , the closure phase, given by:

$$\Psi_{123} = \text{Arg}(R_{13}) - \text{Arg}(R_{12}) - \text{Arg}(R_{23}) \quad (3.5)$$

where $\text{Arg}(R_{ij})$ represents the argument of the interferometer pair formed by the correlation of the i -th and j -th channels. By substituting the arguments of the fringes given by equations (3.2 - 3.4) into equation (3.6), Ψ_{123} can be rewritten:

$$\Psi_{123} = \Psi(n_{13}) - [\Psi(n_{12}) + \Psi(n_{23})] \quad (3.6)$$

Hence the closure phase for a set of three baselines is solely a function of the phases of the Fourier transform of the source brightness distribution at the respective component spacings. If therefore the complex visibilities at the two shorter baselines are known, the value at the longest baseline can be measured directly. Hence the phase can be mapped unambiguously in terms of the phase Ψ_{MIN} , associated with the minimum spacings. If these are chosen short enough, Ψ_{MIN} can be assumed to be equal to zero, since $\Psi(n)$ is zero at $n = 0$ and varies slowly with increasing n . However, it is clear that this method does give rise to a



↔
20 sec

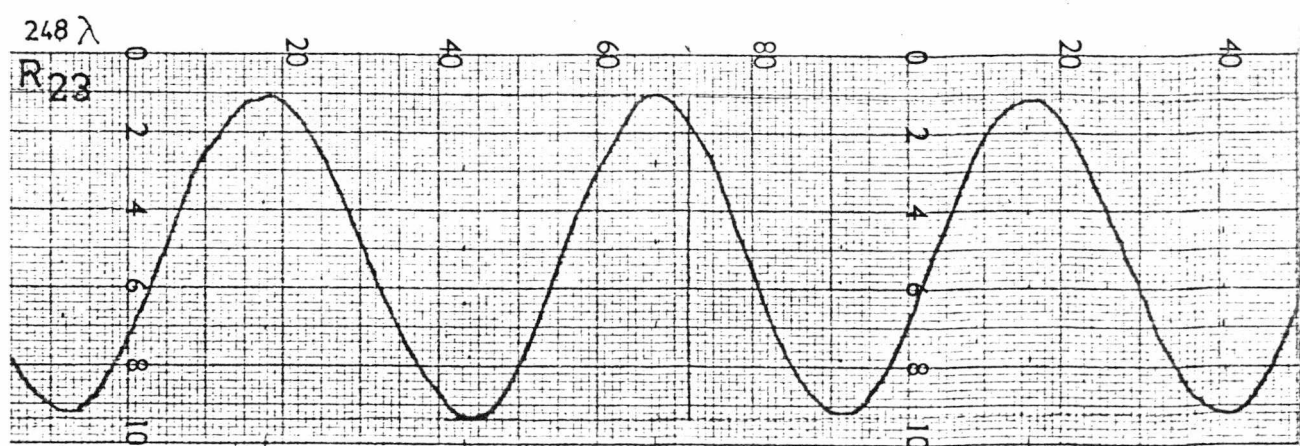
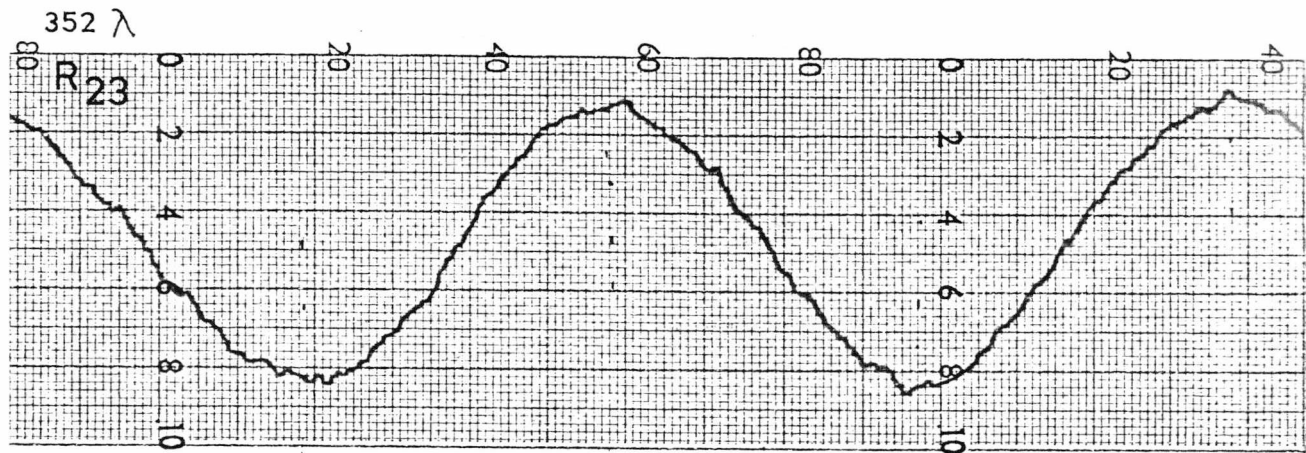
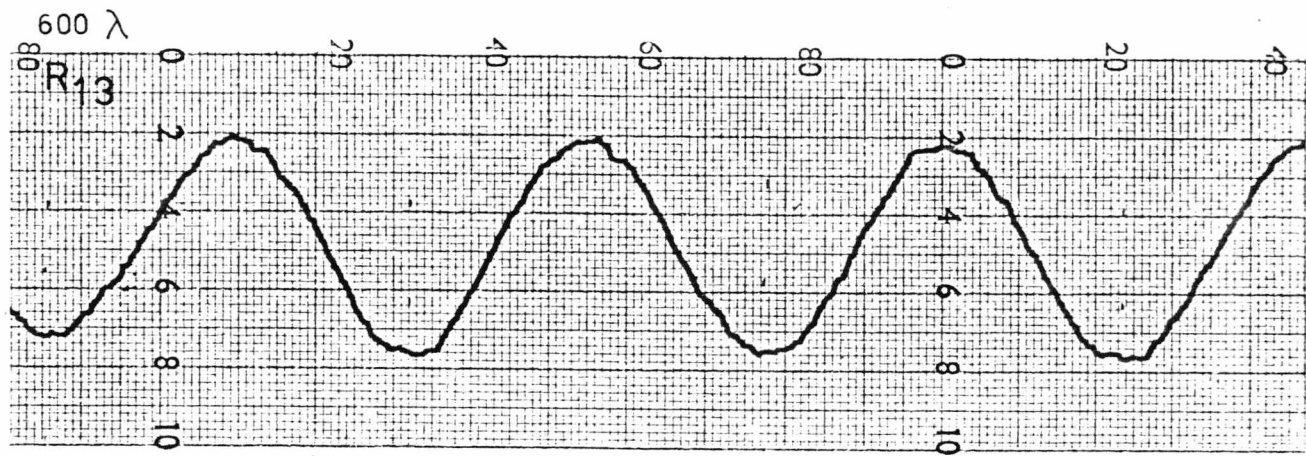


FIG. 3.1 Triple Interferometer Fringes Of Cassiopeia A — May 10th 1980



↔
10 sec

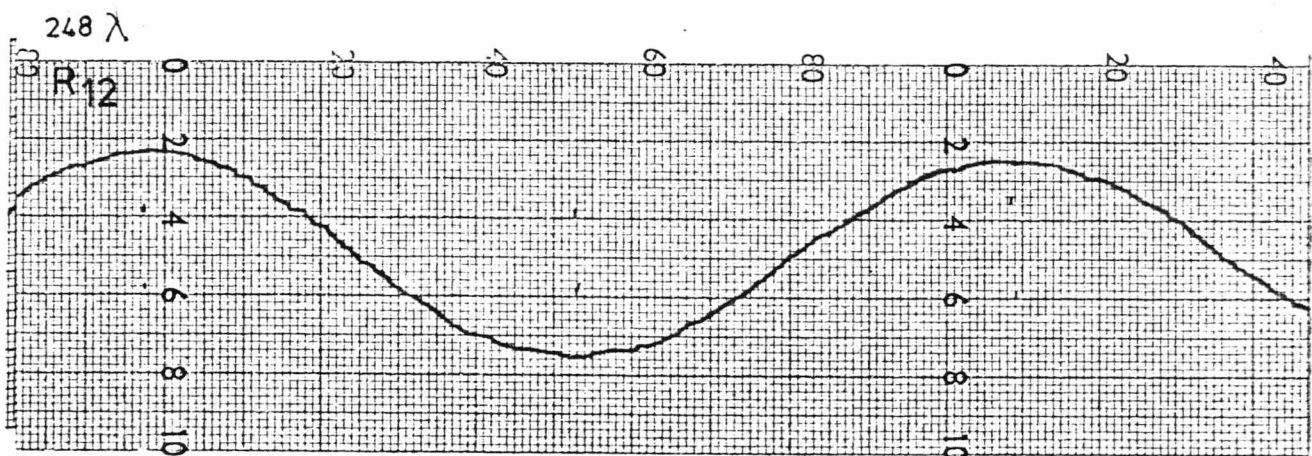
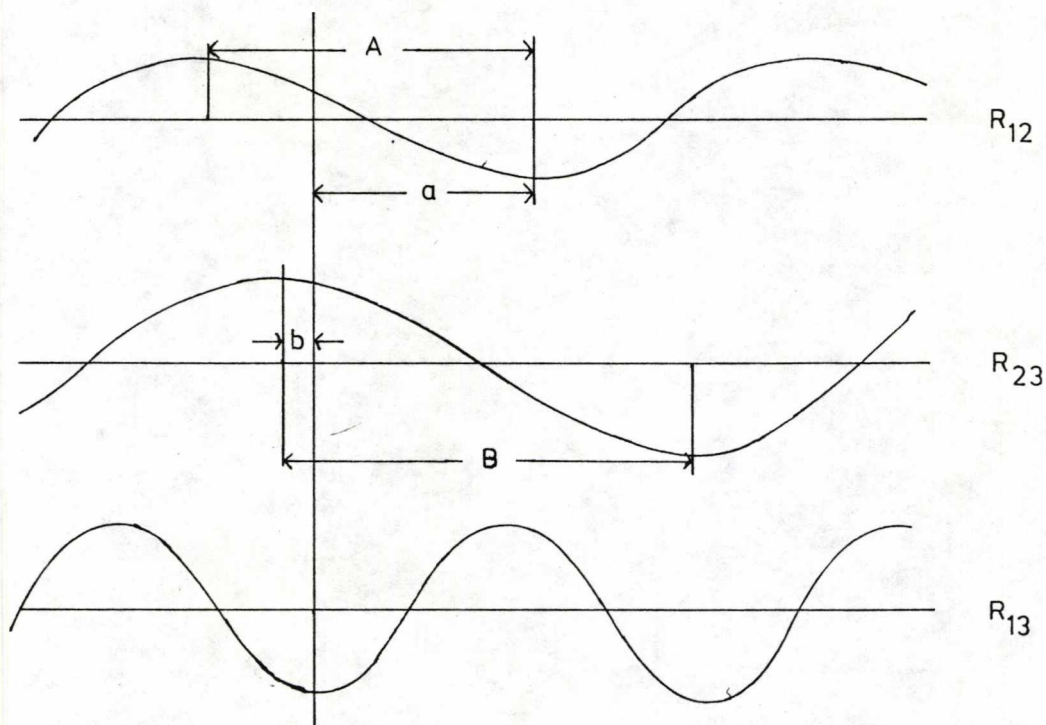


FIG. 3.2 Triple Interferometer Fringes Of Cassiopeia A — October 26th 1980

cumulative error, and therefore it is wise to develop model fitting procedures to interpret independently the closure results (see Chapter 6).

To calculate the closure phase, the method used by Latham (1957) and Matheson (1973) was adopted. It is illustrated below in Fig. 3.3. For each of the maxima of interferometer output ' R_{13} ', a , A , b and B were formed and measured. Using the sign convention that a positive phase angle corresponds to a shift in the centre of gravity of the source to an earlier right ascension, the closure phase can be formed as given by equation (3.7). This particular



$$\Psi_{123} = (a/A - b/B) \times 180^\circ \quad (3.7)$$

FIG. 3.3 Calculation Of The Closure Phase

sign convention was adopted for consistency with the earlier work of Jennison and Latham (1959) and Matheson (1974). However, it should be noted that the usual sign convention used in interferometry is that the phase increases for a source displacement towards the north and east (Fomalont and Wright 1974) i.e. a later right ascension.

In forming the closure phase, particular care has to be taken in the alignment of the triple-pen recorder since considerable errors can result if the pens are misaligned. To further this aim, the system was calibrated regularly at the beginning and end of every run, and any misalignment allowed for in the calculations referred to above.

3.2 MEASUREMENT OF AMPLITUDE

Latham (1957) and Jennison (1958) have also shown that a second, closure amplitude, relationship can be formed for a triplet of baselines which is independent of receiver and aerial gains of each channel, as long as a fourth multiplier is used as a total power unit correlating one channel with itself. An example of a typical total power run, the time scale compressed by a factor of five compared with the normal chart speed utilised, is illustrated in Fig. 3.4. Following the notation used above, the output of the fourth multiplier can be expressed by:

$$R_{11} = g_4(A_1)^2 \quad (3.8)$$

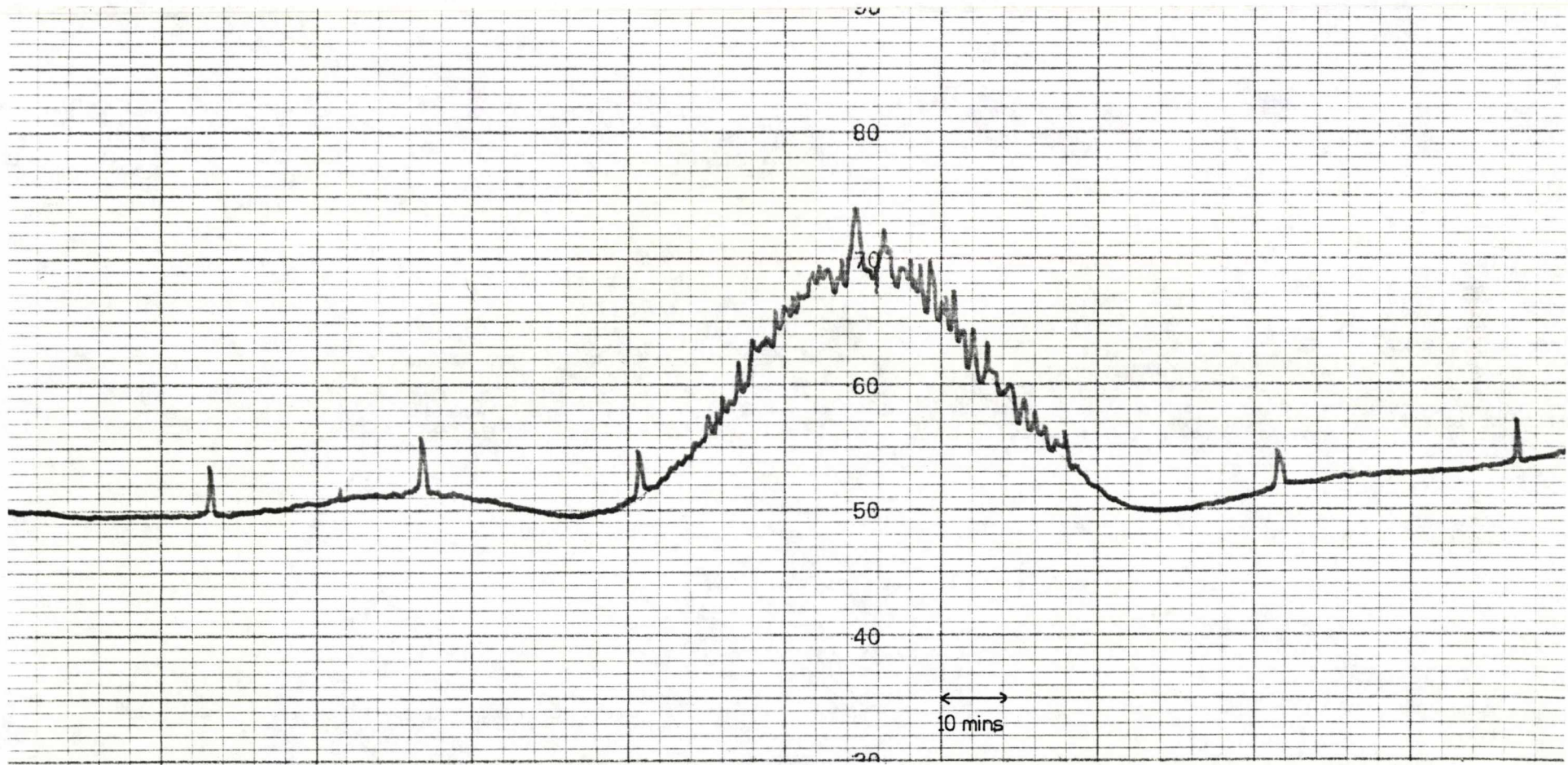


FIG. 3.4 Total Power Run : 1/5th Normal Chart Speed

The closure amplitude relationship can be represented by a function F'_{123} where

$$F'_{123} = \frac{|R_{12}| |R_{13}|}{|R_{11}| |R_{23}|} \quad (3.9)$$

$|R_{ij}|$ represents the modulus of each set of fringes formed by the correlation of the i -th and j -th channels, or in the case of $|R_{11}|$ the height of the deflection caused by the transit of the source in the homestation beam.

By substituting the moduli of the outputs given by equations (3.2 - 3.4) and (3.8), into equation (3.9), F'_{123} can be written:

$$F'_{123} = \frac{g_1 g_3}{g_2 g_4} \frac{F(n_{12}) F(n_{13})}{F(n_{23})} \quad (3.10)$$

By a simple calibration procedure of injecting a coherent signal into all the multiplier ports connected together, the constant of equation (3.10) can easily be found and hence the closure amplitude, F_{123} , calculated where

$$F_{123} = \frac{F(n_{12}) F(n_{13})}{F(n_{23})} \quad (3.11)$$

From equation (3.11), it is clear that the amplitude of the complex visibility function can be measured directly if the corresponding values at shorter baselines are known. In particular, if $n_{12} = n_{23}$, $F(n_{13})$ can be found without any prior knowledge of the amplitude visibility function.

3.3 PRELIMINARY TESTS

3.3.1 Bandwidths

In Section 2.1, it was stated that fundamentally each receiving channel consisted of a superheterodyne receiver with an i.f. of 10.7MHz, but that the r.f. and i.f. stages were later separated in the case of the two outstations to enable two stations to function remotely. In the initial construction the receivers were tested independently and a summary of the performance characteristics is presented in Table 3.1 below.

		units	STATION		
			A	B	C
-centre frequency-		MHz	37.990	37.992	37.989
intermediate frequency		MHz	10.690	10.692	10.689
r.f. & mixer	3db bandwidth	kHz	480	520	520
	gain - 0V g.c.	db	29	21	27
	gain - 1.5V	db	54	51	57
	current drain	mA	7.0	8.2	7.5
i.f.	3db bandwidth	kHz	110	106	118
	gain - 0V g.c.	db	36	25	29
	gain - 0.75V	db	85	77	87
	current drain	mA	9.0	9.8	7.5
noise figure		db	4.4	2.6	4.4
overall gain - 0V g.c.		db	65	46	56
supply voltage		V	12	12	12

TABLE 3.1 : Basic Receiver Characteristics

Matheson (1973) shows that frequency dispersion can be responsible for considerable errors in phase closure, since any frequency dependent terms will not cancel on performing closure. However, from the three centre receiving frequencies, the deviation of the outstation frequencies (stations B & C in Table 3.1) from that of the homestation were calculated to be 0.005% and 0.003% respectively, percentages small enough to assume dispersive effects on the phase to be negligible. For confirmation Matheson's equation (6.3) was used to evaluate the effect. A negligible error of less than 0.2° was estimated.

The more important effect is that of the bandwidths of each receiver, and these are plotted in Fig. 3.5. Although channels A and B were found to be reasonably identical, channel C indicated approximately 2% deviation from the homestation channel. Latham (1957) has reported that it is important that the bandwidths should be as identical as possible, since each of equations (3.2 - 3.4 & 3.9) should strictly be multiplied by integrals over their respective bandwidths. Hence bandwidth deviations between the channels can lead to imperfect closure. As a check of any possible error introduced by unidentical bandwidths, the amplitude of the visibility function at the very short spacing of 44λ was measured as described below in Section 3.3.2.

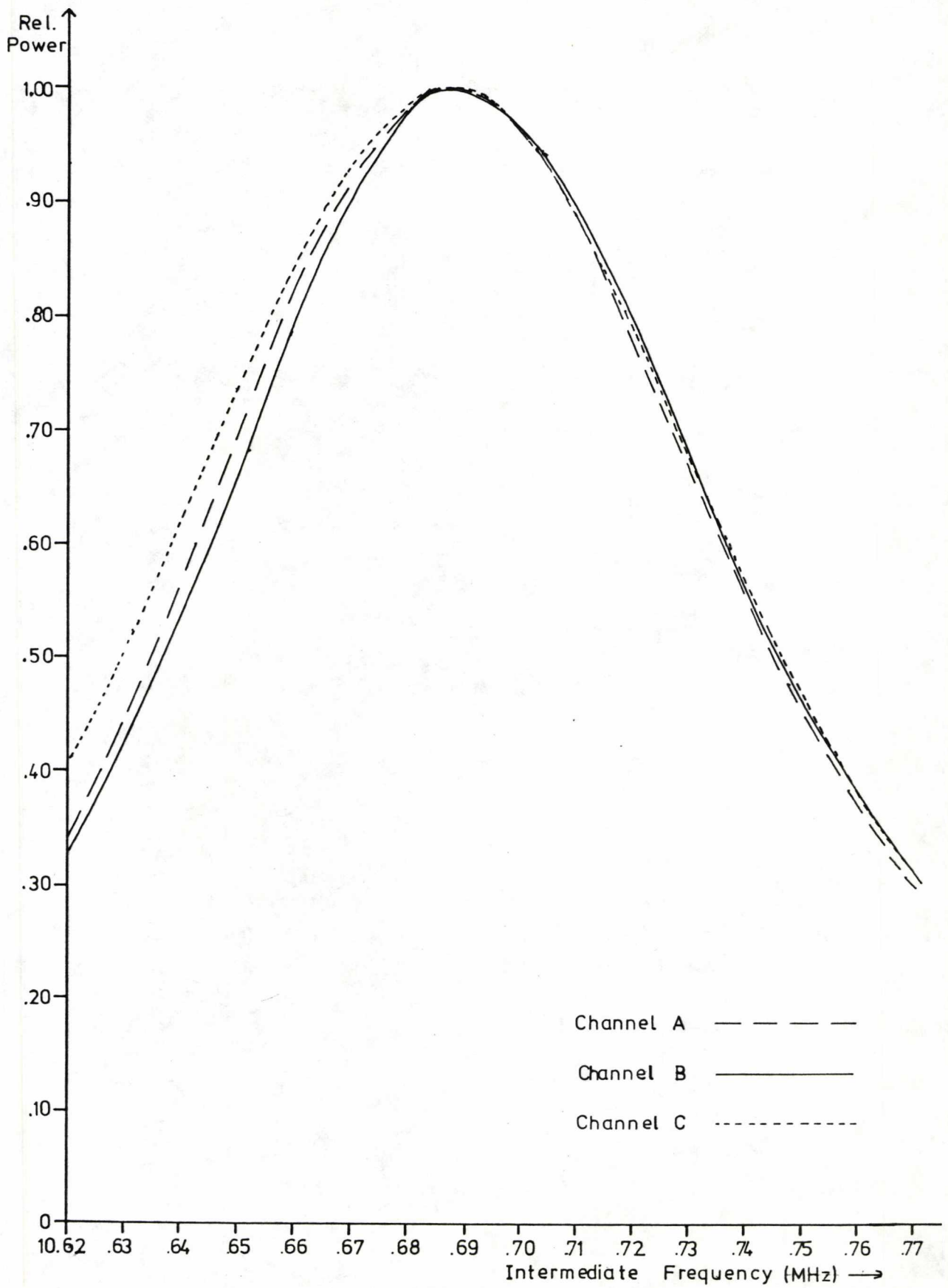


FIG. 3.5 Comparison Of Receiver Bandwidths

3.3.2 Check of Closure Amplitude

Using the homestation, a single dipole 24λ away and a third station a further 23λ from the dipole, a test of closure amplitude was performed. Unfortunately, due to the position of the base-station, availability of suitable sites for short baseline work was severely limited. Hence the final baselines used lay at significantly different angles to the east-west axis, 22.9° and -11.9° respectively, resulting in a baseline of 44λ , inclined at 5.8° to east-west, between the outer two aerial systems.

Nevertheless, a closure amplitude of 0.992 ± 0.007 was measured suggesting that any errors due to dispersion were negligible compared to the errors accounted for in deriving the error bars (see Chapter 4).

3.3.3 Check of Closure Phase

Closure phase was checked by using phase rotators to artificially generate fringes. Rotating the i.f., such that the fringe frequency was of the same order of magnitude as the rate expected at the longest baselines, closure phase was performed on the outputs, care taken to ascertain that the pens were perfectly aligned. Initially the fringes were found to be slightly misaligned and an error of the order of 6° was evaluated in the prototype system.

Since the phase closure method eliminates any errors

prior to the signals splitting in the emitter follower buffer amplifiers, it was assumed that the error was a combination of small phase delays taken to the multiplier units after the split in the buffer amplifiers. Even a small differential phase shift between two ports of the same buffer amplifier could have explained the effect. It was therefore decided to cancel the effect and equalize the small differential phase shifts between ports rather than redesign the system. Hence the leads between emitter follower units and the multipliers were systematically rotated until a system with precisely aligned fringes resulted. The output of the final tests is reproduced in Fig. 3.6.

The system layout was carefully marked such that no accidental removal of leads would produce an uncertainty in inter-unit connections. (Despite this care the leads were at a later date wrongly connected for the duration of two baselines, as reported in Sections 3.6 and 6.5!)

3.3.4 Check of Cross-talk between Channels

The final preliminary test to be performed was a check of the isolation of each channel. Three independent, incoherent noise sources were connected to each of the three i.f. amplifiers. Each of the outputs was rotated in turn by a phase rotator and the resultant trace investigated for residual fringes due to cross-talk between the channels.

With the amplifier gains and pen-recorder scale set at

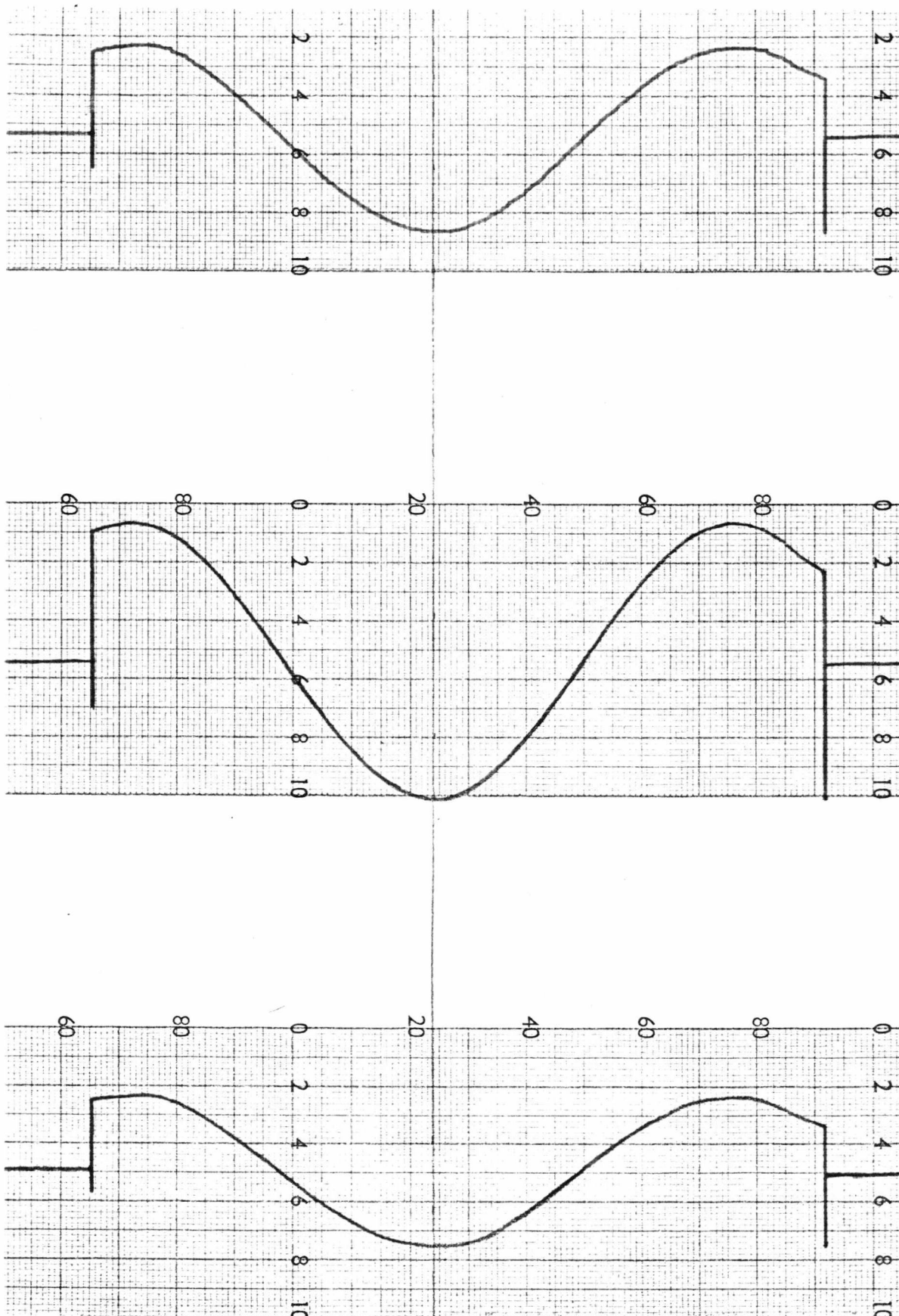


FIG. 3.6

Check Of Closure Phase

their usual levels, no fringes were observed. With the amplifier set approximately 3db above its normal output level and the chart sensitivity increased by a factor of ten, the experiment was repeated. Some residual fringing was noted, as illustrated in Fig. 3.7 for channel LX3. Since the modulus of the fringes was of the same order as the inherent noise of the channel, and, transposed back to the usual operational conditions, equivalent to about one-fifth the width of the line tracing the fringes, the effect of cross-talk was considered negligible.

3.4 SAMPLING OF THE VISIBILITY FUNCTION

A total of nine sites were used, including that of the close baseline station next to the laboratories which utilised a single dipole. The sites and their corresponding Ordnance Survey map reference number are summarised in Table 3.2 (see page 49). Each of the sites listed, was chosen more by its availability and reasonable access than by radio astronomical considerations, although a more accurate gridding in baseline space would have served the mapping of the visibility function rather better. A list of all 17 baselines used, with their corresponding parameters is listed below in Table 3.3 (see page 50). The two baselines utilising the 'workshop' dipole are included although their primary use was in checking the operation of closure amplitude, and hence, calibration of the system at short baselines. The mean position angle for the sampled visibility function was 83° .

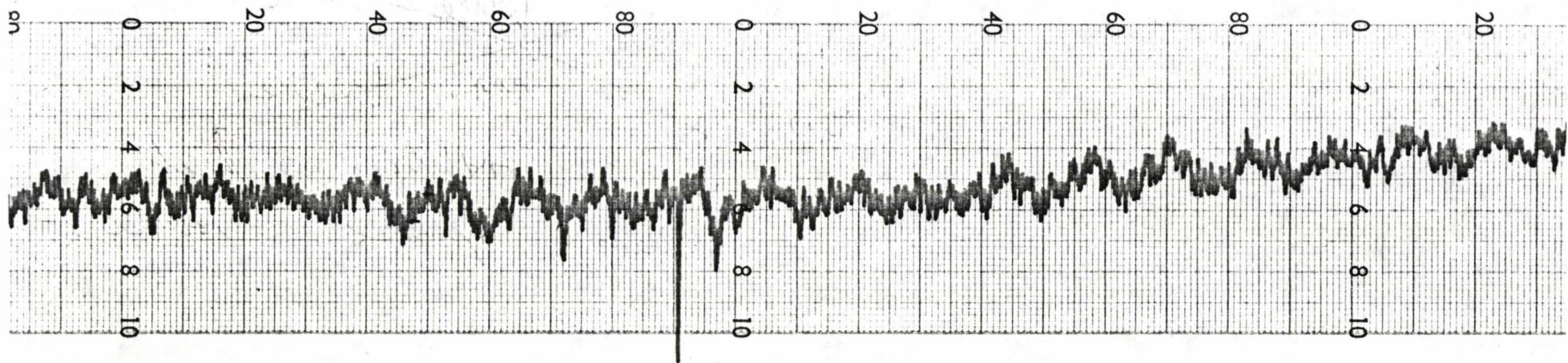


FIG. 3.7

Channel 1 x 3: Residual Fringing

Name of site	Aerial structure	O.S. ref. no.	Symbol
DARWIN	4 Yagis	TR 1433 6009	DA
CHEMISTRY	4 Yagis	TR 1388 5995	CH
WORKSHOP	1 Dipole	TR 1370 5998	W
FIELD ARRAY	18 Dipoles	TR 1353 5990	FA
HOTHE COURT	4 Dipoles	TR 1301 5979	H
T.V. STATION	4 Dipoles	TR 1242 5970	T
CHURCH WOOD	4 Dipoles	TR 1160 5958	C
BOSSENDEN FARM	4 Dipoles	TR 0881 5959	B
DUNKIRK	4 Dipoles	TR 0791 5944	D

TABLE 3.2 : Summary of the Stations

In Fig. 3.8 (page 51) a map utilising the contours from the Ordnance Survey map at a position angle of 83° , is reproduced, illustrating the terrain and giving the relative positions of the nine sites projected onto a position angle of 83° .

For completeness, Table 3.4 (page 52) is included which summarises each series of closure visibility runs, giving details of the dates of the experiments, the baselines utilised and the delays inserted into the paths of the two stations closest to the laboratories.

Baseline		Length		Angle to E/W ($^{\circ}$)
from	to	(m)	(λ)	
Darwin	Chemistry	471	60	15.0
	Field Array	822	104	11.1
	Hothe Court	1353	172	10.5
	T.V. Station	1949	247	9.2
	Church Wood	2777	352	8.3
Chemistry	Field Array	353	44	5.8
Field Array	Hothe Court	531	67	9.6
	T.V. Station	1128	143	7.9
	Church Wood	1956	247	7.1
	Bossenden Farm	4730	600	1.4
	Dunkirk	5643	715	2.9
Hothe Court	T.V. Station	597	76	6.3
T.V. Station	Church Wood	829	105	6.0
Church Wood	Bossenden Farm	2790	354	-2.5
Bossenden Farm	Dunkirk	912	115	7.1
Workshop	Field Array	188	24	22.9
Chemistry	Workshop	183	23	-11.8

TABLE 3.3 : Baseline Parameters

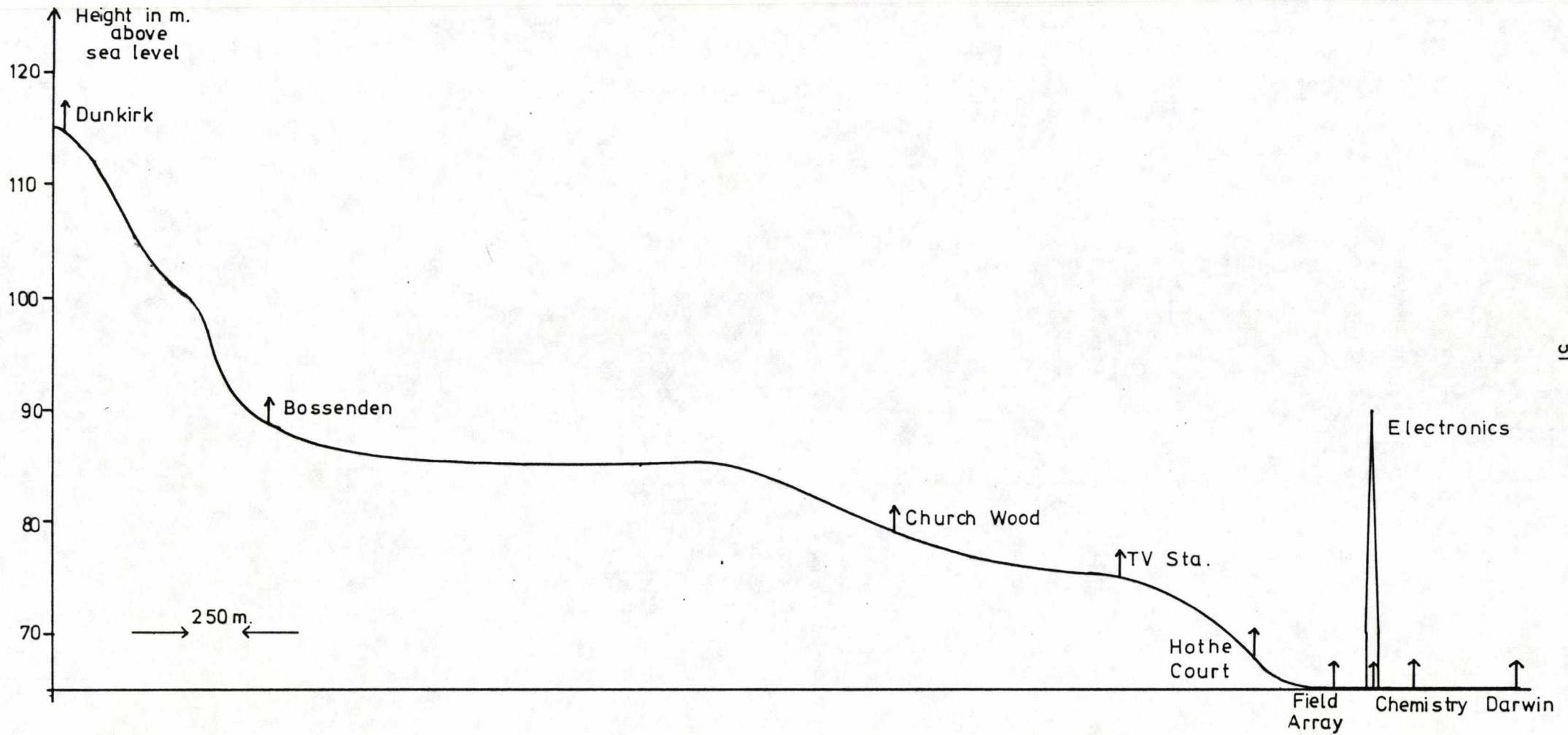


FIG. 3.8 Map Illustrating The Terrain & Siting Of The Outstations

Series	Length longest baseline	Number runs analysed	Dates of expt.		Baselines used			Delays inserted			
			first run	last run	R ₁₂	R ₂₃	R ₁₃	delay (μ sec)	Chan.	delay (μ sec)	Chan.
1	44	6	30.06.79	13.07.79	CH/W	W/FA	CH/FA	0.92	W	0.58	CH
2	104	6	17.08.79	18.09.79	DA/CH	CH/FA	DA/FA	1.07	FA	1.56	CH
3	172	7	3.10.79	31.10.79	DA/FA	FA/H	DA/H	1.45	FA	0.27	D
4	143	6	21.11.79	4.12.79	FA/H	H/T	FA/T	1.93	H	3.38	FA
5	247(i)	10	8.12.79	19.01.80	DA/FA	FA/T	DA/T	3.58	FA	2.25	D
6	247(ii)	7	17.04.80	24.04.80	FA/T	T/C	FA/C	2.76	T	6.33	FA
7	352	9	25.04.80	11.05.80	DA/FA	FA/C	DA/C	6.33	FA	5.01	D
8	600	13	23.07.80	29.10.80	FA/C	C/B	FA/B	9.20	C	15.53	FA
9	715	5	16.12.80	20.03.81	FA/B	B/D	FA/D	2.98	B	18.51	FA

TABLE 3.4 : Summary of Each Series of Measurements of the Closure Visibility

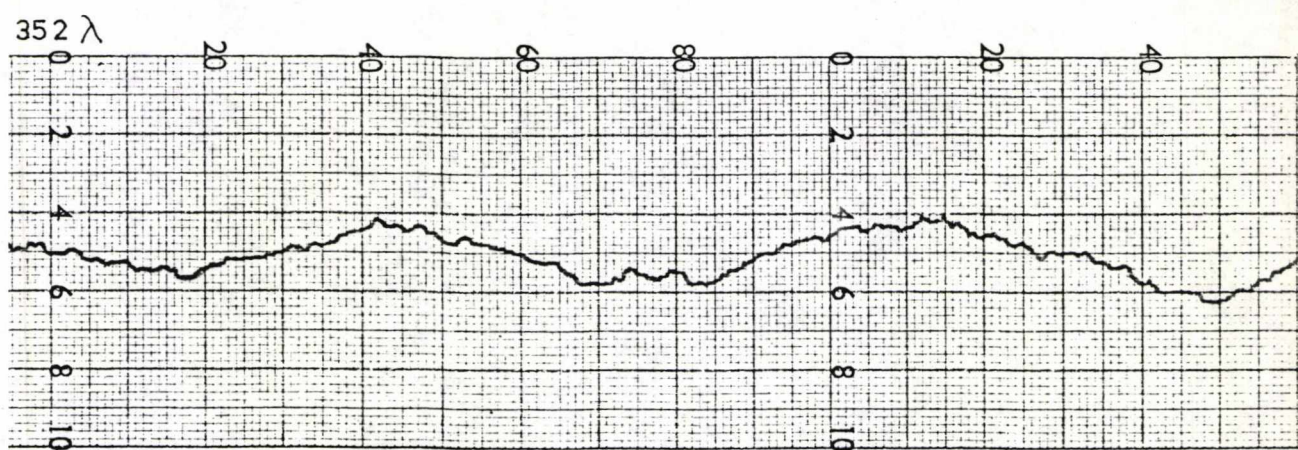
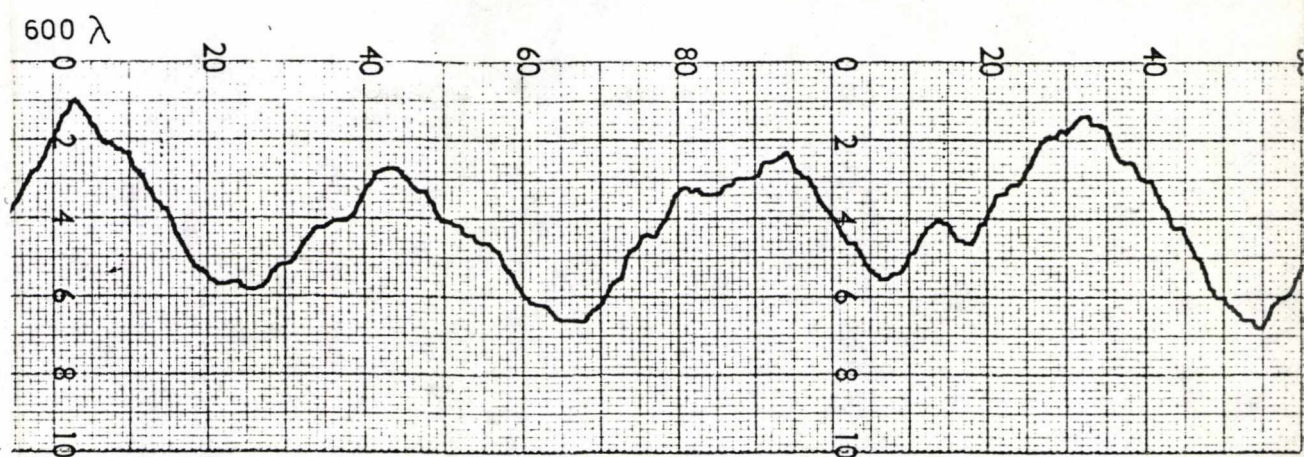
3.5 THE EFFECT OF INTERFERENCE AND SCINTILLATION

From Table 3.4 it is immediately obvious that only about 40% of the runs yielded analysable fringes. The major effect restricting a better performance was the gross scintillation which tended to destroy the fringes preventing any measurements from being taken. A typical scintillated run is reproduced in Fig. 3.9. In particular, the high percentage of 'useless' runs can be attributed to the fact all measurements were made around the maximum of the solar cycle.

When solar activity was extremely high, the ionisation density of the ionosphere was such that signals generated at 38MHz in other parts of the world, especially the Soviet Union in the mornings and the U.S.A. in the afternoons, were reflected in the F2 layer with the increase of the MUF (Maximum Usable Frequency). This effect was such that almost all runs in the months of January to March, when Cassiopeia A transited in the day-time, were rendered unanalysable by interference obliterating the fringes.

3.6 OTHER TESTS

In the course of the observations, tests on the performance of the system were carried out by measurements on Cygnus A at baselines of 600λ and 715λ . Cygnus A has been assumed symmetrical at high frequencies (Winter et. al. 1980), hence it is reasonable to extend this assumption to 38MHz and expect a zero phase angle on performing phase closure at the



↔
10 sec

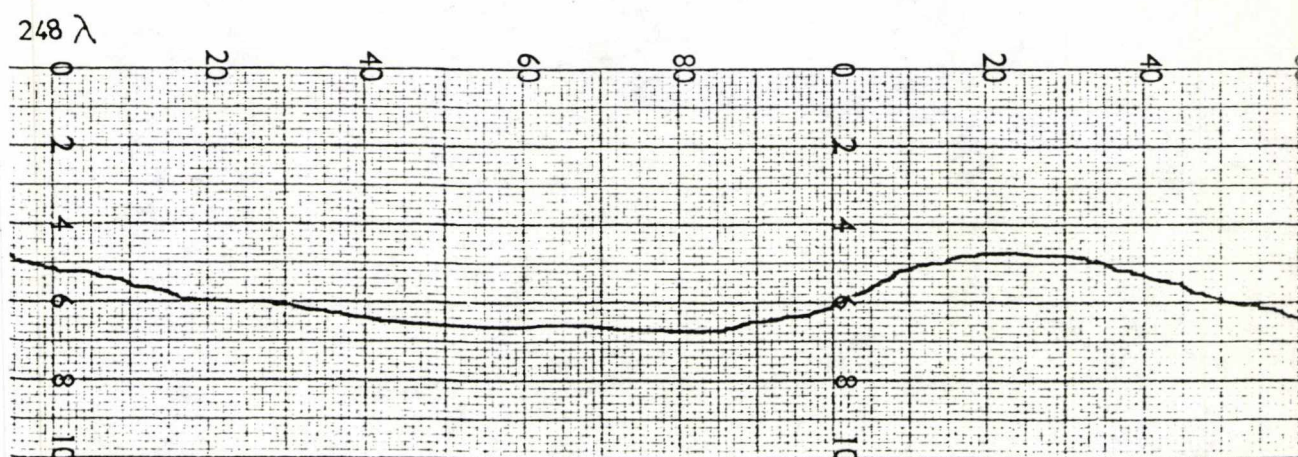


FIG. 3.9 Scintillated Run Illustrating Fringe Obliteration
— July 29th 1980

specified baselines.

In fact, the first measurements produced slightly positive results suggesting the possibility of a small systematic phase error. The equipment was checked and it was found that several leads from the buffer amplifiers to the multipliers had been interchanged, presumably at the time when the system was moved just before the series of measurements on the 247λ spatial frequency. The system was reconnected following the original labelling and measurements on Cygnus A repeated. Calculating the phase gave closure results of $0.2^\circ \pm 1.3^\circ$ at the 600λ baseline, confirming there were no systematic errors in the system as far as phase was concerned. Further checks at 715λ , at a later date, resulted in a closure phase of $-0.7^\circ \pm 4.7^\circ$ agreeing with the above conclusion.

In Fig. 3.10, the amplitude results of 0.61 ± 0.05 at 600λ and 0.56 ± 0.05 at 715λ , are superimposed on the results of Jennison and Latham (1959) - measured at epoch c.1956 - indicating a reasonable agreement with the structure known to exist at higher frequencies. It, however, has to be added that the component visibilities at 247λ and 352λ for the 600λ baseline, and, 115λ for the 715λ baseline, were interpolated from the results of Jennison and Latham to enable reconstruction of the visibility amplitudes at 600λ and 715λ from their closure amplitudes.

From these rather important tests, primarily limited by the errors due to the transit of Cygnus A in the home-station channel producing a total-power deflection

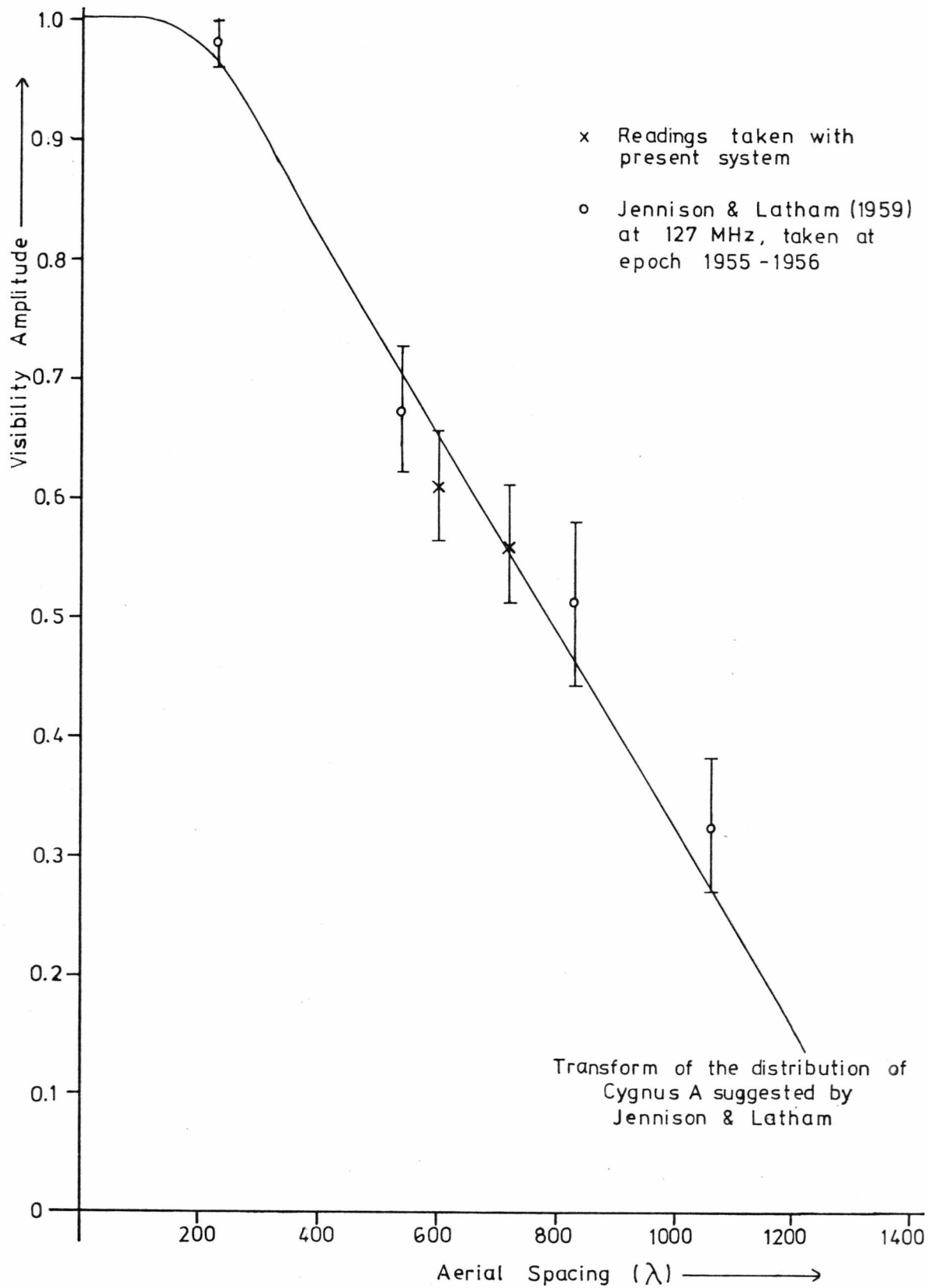


FIG. 3.10 The Amplitude Visibility Function Of Cygnus A

superimposed on an inflection in the output caused by the galaxy, it was concluded that the system was working satisfactorily.

CHAPTER 4

ERRORS IN THE MEASUREMENT OF THE VISIBILITY
FUNCTION4.1 INTRODUCTION

For each series of baseline triplets, a number of runs were analysed as summarised in Table 3.4, leading to error bars presented with the final results that include estimates of both the systematic and the random errors limiting the precision of the measured data. As an estimate of the random errors, the standard error of the mean was used as defined by Martin (1971):

$$\Delta x = \left[\frac{1}{n(n-1)} \sum_{i=1}^n (x_i - \bar{x})^2 \right]^{1/2}$$

In all cases of the amplitude and phase results, each baseline triplet was operated until the standard error of the mean was small compared with the estimates of the systematic errors in the system not cancelled out by the closure methods employed.

Although the closure phase and closure amplitude method does theoretically remove errors up to the point where each channel is split in the buffer amplifiers, in practice certain effects are present which have to be considered since they increase the size of the error bars associated with each

measurement of a complex visibility. In particular, that which is presently referred to as the 'Cygnus A effect', and also, the effect of decorrelation due to the use of finite bandwidths are discussed in Sections 4.2 and 4.3 respectively. In presenting the errors, estimates have also to be made of any other effects which can put some systematic bias on the results and these are considered in Section 4.4.

4.2 THE CYGNUS A EFFECT

The fact that there was some effect on the results due to the transit of Cygnus A in the side-lobes whilst Cassiopeia A was transiting in the main beam, has already been mentioned in Section 2.2.3. Of course, only one of the three interferometer channels was affected, that of the two remote stations correlated together, since the other two channels involved the use of the narrow beam homestation aerial in one limb of each interferometer.

To estimate the contribution due to Cygnus A in the case of the two remote, dipole stations, required precise knowledge of the far-field pattern of the aeriels. At 38MHz, this was rather difficult to determine and, therefore, the effect was investigated by observing Cassiopeia A with an interferometer spacing of 143λ , at a time when the nebula was in approximately the same area of the sky as Cygnus would be during a meridian transit of Cassiopeia A. Since the two sources lie at significantly different declinations

this could never be accomplished fully; however, noting that theoretically the aerial beam was narrowest in the east-west direction, Cassiopeia A was observed when its angle to the plane of the meridian was closest to the corresponding angle, 35.45° , for Cygnus A, when the latter source was at an hour angle of 3hr. 23min. Hence Cassiopeia was observed at an hour angle of 6hr., its angle to the plane of the meridian being 31.47° , close enough to give a first order estimate of the magnitude of the side-lobes in the east-west direction.

Observing Cassiopeia A with an almost east-west baseline and at an hour angle of 6hr., necessitated both insertion of extra delays and the use of fringe rotators, since the projected baseline was orientated north-south. The rate of fringe rotation was determined by the source Taurus A, which at the time of observation was transiting the meridian. Hence the fringe rotator was set to null out the Taurus fringes.

No fringes due to Cassiopeia A were observed and, hence, an upper limit of 1%, an estimate of the sensitivity of the interferometer, was placed on the effect of the side-lobe. Such an upper limit to the relative power contribution of Cygnus A for the remote stations, implied a possible 1% error in the measured fringe amplitude at meridian transit of Cassiopeia A.

To obtain a rough estimate of the effect of such a relative power contribution of Cygnus A on the fringes

analysed over a whole run, the simple model described in Fig. 4.1 was Fourier transformed. Since only the gross effect of the two sources separated at a large hour angle from each other was of interest, the model consisted of two delta functions as approximate representations of the two sources. Therefore, it was assumed for the purpose of the calculation that neither source was ever resolved, and that their separation in the interferometer beam remained constant over the period of observation.

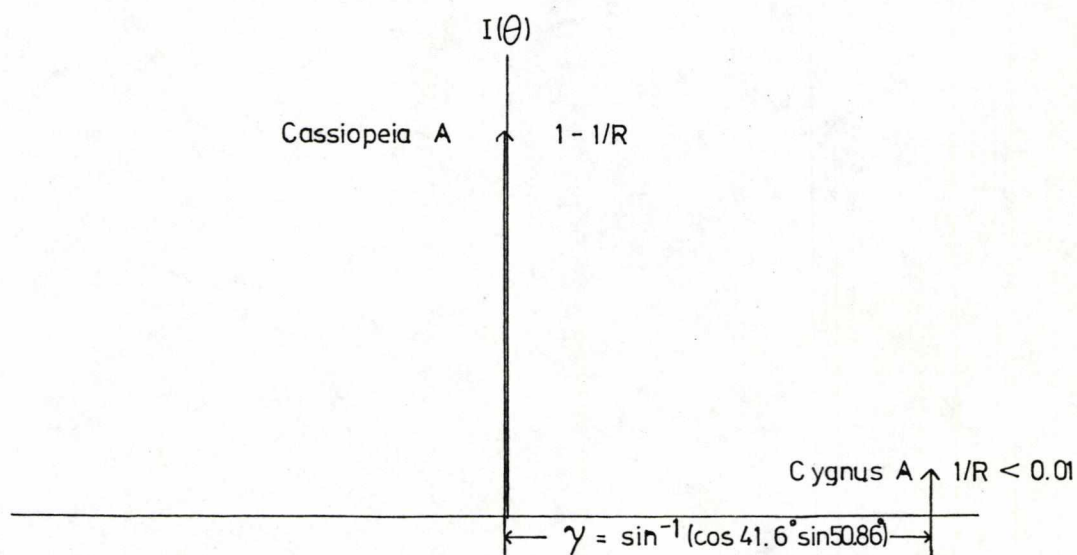


FIG. 4.1 Model Brightness Distribution

From Fig. 4.1, the intensity distribution $I(\theta)$ can be written:

$$I(\theta) = (1 - 1/R)\delta(\theta) + 1/R\delta(\theta - \gamma)$$

Rewriting equation (A2.6) of Appendix 2, the interferometer output $R(t)$ can be expressed:

$$R(t) = \exp[2\pi ni(\cos\delta \sinh)] \int_{-\infty}^{\infty} I(\theta) d\theta \exp[2\pi ni\theta]$$

$$= 1/R [(R-1)\exp[2\pi ni(\cos\delta_1 \sinh_1)] + \exp[2\pi ni(\cos\delta_2 \sinh_2) + 2\pi ni\gamma]]$$

where δ_1, h_1 and δ_2, h_2 are the declination and hour angle of Cassiopeia A and Cygnus A respectively.

The interferometer output can now be written in terms of an imaginary and a real component:

$$\text{Im}[R(t)] = 1/R [(R-1)\sin[2\pi n\cos\delta_1 \sinh_1] + \sin[2\pi n\cos\delta_2 \sinh_2 + 2\pi n\gamma]]$$

$$\text{Re}[R(t)] = 1/R [(R-1)\cos[2\pi n\cos\delta_1 \sinh_1] + \cos[2\pi n\cos\delta_2 \sinh_2 + 2\pi n\gamma]]$$

The modulus of the fringes, $R(t)$, can be found from:

$$|R(t)|^2 = \text{Im}^2[R(t)] + \text{Re}^2[R(t)]$$

and the argument, β from:

$$\tan \beta = \text{Im}[R(t)] / \text{Re}[R(t)] \quad (4.1)$$

For a meridian transit of Cassiopeia A, δ_1, δ_2, h_1 and h_2 are $58.53^\circ, 40.60^\circ, \phi$ and $50.86^\circ + \phi$ respectively where ϕ is the hour angle of Cassiopeia A. Hence the modulus of the fringes is given by:

$$|R(t)|^2 = 1/R [(R-1)^2 + 1 + 2(R-1)\cos 2\pi n[\cos 58.53^\circ \sin \phi - \cos 40.6^\circ \sin(50.86^\circ + \phi) - \gamma]]$$

Since ϕ is small, $\sin(50.86^\circ + \phi) \sim \sin 50.86^\circ + \phi \cos 50.86^\circ$

$$\therefore |R(t)|^2 = \left(\frac{R-1}{R}\right)^2 \left(1 + \frac{1}{(R-1)^2} + \frac{2}{(R-1)} \cos 2\pi n[0.0427\phi - 1.2076]\right)$$

Hence for large R , the amplitude of the fringes can be written:

$$\begin{aligned} |R(t)| &\sim \left(\frac{R-1}{R}\right) \left(1 + \frac{1}{(R-1)} \cos 2\pi n[0.0427\phi - 1.2076]\right) \\ &= 1 - 1/R + 1/R(\cos 2\pi n[0.0427\phi - 1.2076]) \end{aligned}$$

Thus for a small Cygnus component the fringe amplitude is a cosinusoidal variation of maximum amplitude $1/R$ and period $1/(0.0427n)\text{rad.}$, around the value due to the Cassiopeia A source alone. Considering a 250λ baseline, gives a period of approximately 21.5 minutes; considering a 600λ baseline, a period of approximately 9 minutes results. This effect was considered negligible since A) every run was analysed for a significant proportion of the period, or integral number thereof, the mean error tending to zero; and B) no periodic variation of the fringes was evident in any of the unscintillated runs.

The equation for the phase, (4.1), is quite complex to solve, and therefore the variation of β with ϕ for a single baseline was considered as an example of the effect.

$$\text{For } n=250\lambda: \quad \tan \beta = \frac{(R-1)\sin 819.96\phi + \sin(752.83\phi + 1896.93)}{(R-1)\cos 819.96\phi + \cos(752.83\phi + 1896.93)} \quad (4.2)$$

With no Cygnus component (infinite 'R') the corresponding

phase is given by:

$$\tan \beta_{\text{Cas}} = \frac{\sin 819.96 \phi}{\cos 819.96 \phi} = \tan 819.96 \phi \quad (4.3)$$

With R set to 100 as an upper limit to this effect, both equations (4.2) and (4.3) were evaluated for $\phi = \phi_i$ where

$$\phi_i = 1/4 \frac{2\pi i}{752.83}$$

and for each ϕ , the error term ' β_{er}^i ' given by $\beta^i - \beta_{\text{Cas}}^i$ calculated. The results are tabulated in Table 4.1 below.

i	β^i (deg)	β_{Cas}^i (deg)	β_{er}^i (deg)
0	-00.32	0.0	-0.32
1	-82.36	-81.97	-0.39
6	47.58	48.15	-0.57
7	-34.40	-33.82	-0.58
8	63.63	64.20	-0.57
17	46.34	46.43	-0.09
18	-35.56	-35.54	-0.02
19	62.55	62.48	0.07
28	45.28	44.71	0.57
29	-36.69	-37.27	0.58
30	61.34	60.76	0.58
44	-07.15	-06.89	-0.26
45	-89.19	-88.86	-0.33
46	08.77	09.16	-0.39

TABLE 4.1 : Error in Phase due to a 1% Cygnus A Component for a Baseline of 250λ

An examination of Table 4.1 indicates that for small ϕ the error in the measured phase of the fringes, for an assumed Cygnus A component of 1% total flux density, is a cosinusoidal variation of maximum value 0.58° and period 0.0939 radians, equivalent to approximately 21.5 minutes - for a baseline of 250λ . It is therefore reasonable to conclude that the phase error for any baseline of length n , is a cosinusoidal variation of maximum magnitude $1/(R-1)$ radians and period $1/(0.0427n)$.

This effect was also considered negligible for similar reasons stated above for the case of the effect on amplitude, namely, A) every run was analysed for a significant proportion of the period calculated above, the mean error tending to zero, and B) no periodic variation of the phase was evident in the calculated closure phases (although it is doubtful whether any such variation would have been noticed in the very large spread of measured closure phases for a single run). In particular, a maximum error of 0.6° is negligible compared with the final error bars in the phase of the visibility function.

4.3 THE BANDWIDTH EFFECT

Both the analysis of Appendix 2 and the equations of Chapter 3, have assumed a monochromatic source which, of course is false. The effect of a finite bandwidth on an interferometer can be obtained by integrating, with respect to frequency the monochromatic response, over the bandwidth.

From Fomalont and Wright (1972), the broad-band response, $R(t)$, is given by:

$$R(t) = \int \alpha(\nu) R_\nu(t) d\nu \quad (4.4)$$

where $\alpha(\nu)$ is the bandwidth function and $R_\nu(t)$ the monochromatic response for a small hour angle, ϕ , itself given by:

$$R_\nu(t) = g_k F(n_{ij}) \cos \left[2\pi \frac{B\nu}{c} \cos \delta \phi - 2\pi \nu \tau_k - \psi_i + \psi_j + \Psi(n_{ij}) \right]$$

In general, the evaluation of equation (4.4) is complicated for any given bandwidth function. However, if the latter is approximated to by a rectangular function of width, $\Delta\nu$, the integral can easily be evaluated:

$$R(t) = g_k F(n_{ij}) \operatorname{sinc} \frac{\pi \Delta\nu}{c} (B \cos \delta \phi - \Delta l_k) \times \cos \left[2\pi \frac{\nu}{c} (B \cos \delta \phi - \Delta l_k) - \psi_i + \psi_j + \Psi(n_{ij}) \right] \quad (4.5)$$

where $\Delta l_k = l_2 - l_1$ and represents the error in equalizing the paths for a meridian transit.

Clearly the effect of the finite bandwidth is such that the argument of the fringes remains unchanged, but their amplitude is reduced relative to the true value (unless delay tracking is employed where an extra delay is introduced in one limb of the interferometer and continually altered such that $B(\cos \delta)\phi - \Delta l_k$ is always small).

Performing closure amplitude, F_{123} is reduced from the

value given by equation (3.11) by a fraction, f , where

$$f = \frac{\text{sinc } \pi(\Delta\nu/c)[B_{12} \cos \delta\phi - (l_2 - l_1)] \text{sinc } \pi(\Delta\nu/c)[(B_{12} + B_{23}) \cos \delta\phi - (l_3 - l_1)]}{\text{sinc } \pi(\Delta\nu/c)[B_{23} \cos \delta\phi - (l_3 - l_2)]}$$

Hence, the closure amplitude is in general decorrelated by a fraction, k ($k=1-f$), of its true value whenever some differential time delay exists between two limbs of an interferometer.

To estimate the percentage error due to the effect, the errors due to measurements taken t seconds before or after centre transit and those due to uncertainties in path equalisation were considered separately.

Ignoring the errors in path equalisation, equation (4.6) can be rewritten:

$$f(\Delta l_k = 0) = \frac{\text{sinc } \pi(\Delta\nu/c)[B_{12} \cos \delta\phi] \text{sinc } \pi(\Delta\nu/c)[(B_{12} + B_{23}) \cos \delta\phi]}{\text{sinc } \pi(\Delta\nu/c)[B_{23} \cos \delta\phi]}$$

Since B_{12} is usually of the same order as B_{23} , and both B_{12} and B_{23} are less than B_{13} , the errors due to

$$\text{sinc } \pi(\Delta\nu/c)[B_{12} \cos \delta\phi] \quad \text{and} \quad \text{sinc } \pi(\Delta\nu/c)[B_{23} \cos \delta\phi]$$

are both much smaller than those due to

$$\text{sinc } \pi(\Delta\nu/c)[(B_{12} + B_{23}) \cos \delta\phi] \quad (4.7)$$

and approximately cancel, such that only equation (4.7) needs to be evaluated for all baselines to derive an estimate of the errors due to taking measurements either side of meridian transit.

Now for each run, measurements were taken at regular intervals, ϕ_i , in hour angle over the transit of total duration $2\phi_t$. Hence an estimate of the decorrelation for each baseline can be derived by evaluating equation (4.7) at all ϕ_i and taking the mean. Table 4.2 summarises the magnitude of the errors due to this effect using a rectangular bandwidth of 125kHz. This value of the bandwidth was obtained by equating the integral of the bandwidth function (derived from Fig. 3.5) with an equivalent area defined by a rectangular bandshape.

$(B_{12}+B_{23})$ (λ)	Angular interval ϕ_i (deg)	ϕ_t (deg)	decorrelation k (%)
44	2.0	8.0	0.01
104	2.0	8.0	0.04
143	2.0	8.0	0.10
172	1.0	8.0	0.10
247	1.0	6.0	0.10
352	1.0	3.5	0.10
600	0.5	2.5	0.14
715	0.5	2.5	0.20

TABLE 4.2 : Decorrelation due to Taking Measurements
Either Side of Meridian Transit

To estimate the errors due to unequal path compensation, equation (4.6) can be rewritten:

$$f(\phi=0) = \frac{\text{sinc } \pi \Delta \nu \Delta t \text{ sinc } \pi \Delta \nu (\Delta t + \Delta t')}{\text{sinc } \pi \Delta \nu \Delta t'}$$

where $\Delta t = (1/c)l_2 - l_1$ and $\Delta t' = (1/c)l_3 - l_2$

It is evident that minimum f occurs when $\Delta t \gg \Delta t'$. The decorrelation, k , is then given by:

$$k = 1 - \text{sinc}^2 \pi \Delta \nu \Delta t \quad (4.8)$$

Equation (4.8) was evaluated using $\Delta \nu = 125\text{kHz}$, as before, and $\Delta t = 100\text{nsec}$ (see Section 2.5), giving a decorrelation factor of 0.0005. Hence 0.05% was the estimate of the error due to the static differential time delay.

4.4 OTHER MISCELLANEOUS ERRORS

Two further sources of error have not as yet been considered, those due to the linear polarization of the receiving aerials and those due to the calibration procedures employed.

A) Polarization

Since all the aerials used were linearly polarized, any misalignment between elements of the aerials of the three stations caused some reduction in the fringe amplitudes

relative to the correct value. Latham (1957) has quantified the effect, and using his equations and an estimate of 2° as the accuracy to which each element could be aligned with a compass, an error of 0.1% decorrelation was evaluated.

In passing, it can be noted that the effect of differential Faraday rotation was considered negligible. Slee and Wraith (1967) state that baselines up to 5000 wavelengths can be usefully employed at 38MHz near the maximum of the solar cycle, whereas the maximum baseline used in the present series of experiments was only 715λ .

B) Calibration

The method employed in measuring the calibration constant, described in Section 3.2, was directly analogous to the determination of the closure amplitudes, and therefore the values of the constant derived by the procedure were considered to be normally distributed. Hence, an estimate of the error due to the calibration procedure in the case of closure amplitude was calculated from the standard error of the mean of the calibration constant, and it is this estimate which is tabulated in Table 4.3 (see page 71) for the various baselines.

Similarly for closure phase, the error bars presented with the results in the following chapter, include a component due to the uncertainty in pen alignment. This was caused by the accuracy to which the alignment of a coherent calibrating deflection in all three pen outputs could be

read, and was a function of the fringe periods associated with each interferometer output.

4.5 SUMMARY OF THE SOURCES OF ERROR

For each series of baseline triplets, Table 4.3 lists both the percentage errors due to the various sources of systematic bias and the standard error of the mean of the measured data, which together constitute the error bars presented in Chapter 5. Each closure amplitude result is therefore estimated to be accurate to within 1% of its true value.

Longest baseline (λ)	±% error due to			Stan. err. of the mean (absolute)
	Calibration constant	Polarization	Differential time delay	
44	0.23	0.1	0.06	0.004
104	0.26	0.1	0.09	0.003
143	0.26	0.1	0.15	0.002
172	0.79	0.1	0.15	0.002
247i	0.51	0.1	0.15	0.002
247ii	0.24	0.1	0.15	0.004
352	0.63	0.1	0.15	0.001
600	0.22	0.1	0.19	0.001
715	0.78	0.1	0.25	0.001

TABLE 4.3 : Summary of the Sources of Error in the
Measured Closure Amplitudes

In the case of the closure phases, the predominant error was the standard error of the mean with only a small component due to pen alignment uncertainty.

PART TWO

THE LOW FREQUENCY STRUCTURE OF
CASSIOPEIA A

CHAPTER 5

RESULTS OF THE MEASUREMENT OF THE VISIBILITY
FUNCTION

5.1 THE RESULTS

Measurements of the complex visibility function of Cassiopeia A were made during the period from 30th June 1979 to 20th March 1981, the precise dates for each set of baseline triplets having been tabulated in Table 3.4. In Table 5.1, reproduced on page 74, the closure amplitudes and closure phases for each set of baselines are listed, together with their estimated errors.

AC ¹⁾	AB	BC	Closure Amplitude	Closure Phase
44	23	24	0.992 ± 0.008	- 2)
104	60	44	0.961 ± 0.007	0.01 ± 0.1°
143	67	76	0.917 ± 0.007	1.2 ± 0.9°
172	104	67	0.966 ± 0.012	0.7 ± 0.7°
247i ³⁾	104	143	0.907 ± 0.009	-3.7 ± 0.6° 4)
247ii	143	105	0.762 ± 0.008	-5.2 ± 0.8°
352	104	247	0.807 ± 0.008	6.8 ± 0.6°
600	247	354	0.248 ± 0.002	12.1 ± 0.7°
715	600	115	0.0148 ± 0.0004	27.1 ± 1.9°

TABLE 5.1 : Closure Visibility Results

A number of points arise from Table 5.1 which need to be commented on:

- 1) AB+BC is not exactly equal to AC in several cases since the baselines were not precisely collinear (see Table 3.3).
- 2) The closure phase for 44λ was not measured since an extremely small number of fringes resulted over the transit for the two component baselines. The closure phase was assumed equal to zero, the assumption justified by the approximate zero at 104, 143 and 172λ.
- 3) Two sets of readings exist at 247λ since the siting of the outstations allowed observations to be repeated

with different baseline configurations.

- 4) The negative closure phases at 247λ are anomalous and it is highly probable that there was a systematic error not accounted for in the error bars. This effect is further referred to in Section 6.5.

5.2 RECONSTRUCTION OF THE VISIBILITY FUNCTION

One advantage of the present method over the usual use of closure results in VLBI, is that observations have been made for small spacings, with the result that the complex visibilities can be reconstructed from the closure results by the methods outlined in Sections 3.1 and 3.2. This is seldom the case in present day VLBI observations (Readhead and Wilkinson 1978).

However equations (3.9 to 3.11) assume that the total power station is configured as an end-station in a line of three receiving systems, whereas in three cases it was physically the mid-station. For these three cases the equations require modification, and therefore, for completeness all the equations used for reconstructing the visibility amplitudes are presented in Table 5.2 (see page 76).

From Table 5.2 the visibility at 44λ is as given by the value of the closure amplitude, since the two component spacings were approximately equal. However since the visibility amplitudes at baselines 60, 67, 76 and 115λ were

Longest baseline, n_{13}^i (λ)	Visibility amplitude given by
44	$V_{44} \times (F_{23} / F_{24})$
104	$V_{104} \times (F_{60} / F_{44})$
143	$V_{143} \times (F_{76} / F_{67})$
172	$V_{172} \times F_{67} \times F_{104}$
247i	$V_{247}^i \times F_{104} \times F_{143}$
247ii	$V_{247}^{ii} \times (F_{104} / F_{143})$
352	$V_{352} \times F_{104} \times F_{248}$
600	$V_{600} \times (F_{352} / F_{248})$
715	$V_{715} \times (F_{115} / F_{600})$

V_i : closure amplitude for triplet the longest baseline of which is n_{13}^i

F_i : amplitude of the visibility function for a baseline of $i\lambda$

TABLE 5.2 : Reconstruction of the Visibility Amplitudes

neither measured or known, the value at each of the respective spacings had to be interpolated from the measured visibility at 44λ .

Lequeux (1962) working at a higher frequency, has shown that the amplitude of the visibility function of Cassiopeia follows closely a sinc law. Also, Jennison and Latham (1959), at a somewhat lower frequency than Lequeux, found the main body of the nebula to have a distribution given by a slight limb-brightened disc, the Fourier transform of which lies

between a Bessel function of the first order (F.T. of a disc distribution) and a sinc function (F.T. of a rectangular distribution), both of which, to first order and for small spacings, follow a parabola defined by

$$y = 1 - kx^2$$

where x represents the spacing in wavelengths. Hence the visibility function amplitude of Cassiopeia A was approximated to by the parabola at short baselines, using the measured visibility at 44λ to determine k . The results of the approximations are listed in Table 5.3.

Baseline	Visibility amplitude
60λ	0.985 ± 0.015
67λ	0.981 ± 0.018
76λ	0.976 ± 0.024
115λ	0.945 ± 0.054

TABLE 5.3 : Approximations Used in the Visibility Function Reconstruction

The near zero value of the closure phase up to spacings of 172λ indicated that a visibility phase of $0 \pm 0.1^\circ$ (the value at 104λ) could be assumed for the baselines listed in Table 5.3.

The amplitudes and phases of the complex visibility function of Cassiopeia A reconstructed from the closure

visibilities for spacings up to 715λ , are tabulated in Table 5.4 and plotted in Figs. 5.1 and 5.2 for amplitude and phase respectively. By comparing the visibility amplitude at 104λ with the value derived by the parabola approximation, an estimate of the goodness of the approximation can be obtained for spacings up to 104λ . The estimate of 0.955 ± 0.44 at 104λ agrees extremely well with the reconstructed visibility of 0.954 ± 0.014 - suggesting the parabola approximation to be reasonably valid.

Baseline (λ)	Visibility amplitude	Visibility phase
44	0.992 ± 0.008	0.0°
104	0.954 ± 0.014	$0.0^\circ \pm 0.1^\circ$
143	0.912 ± 0.013	$1.2^\circ \pm 1.1^\circ$
172	0.904 ± 0.041	$0.7^\circ \pm 0.9^\circ$
247	0.793 ± 0.022	$-3.2^\circ \pm 1.3^\circ$
352	0.611 ± 0.032	$3.6^\circ \pm 2.0^\circ$
600	0.191 ± 0.017	$12.5^\circ \pm 4.0^\circ$
715	0.074 ± 0.013	$39.6^\circ \pm 6.0^\circ$

TABLE 5.4 : Visibility Function of Cassiopeia A

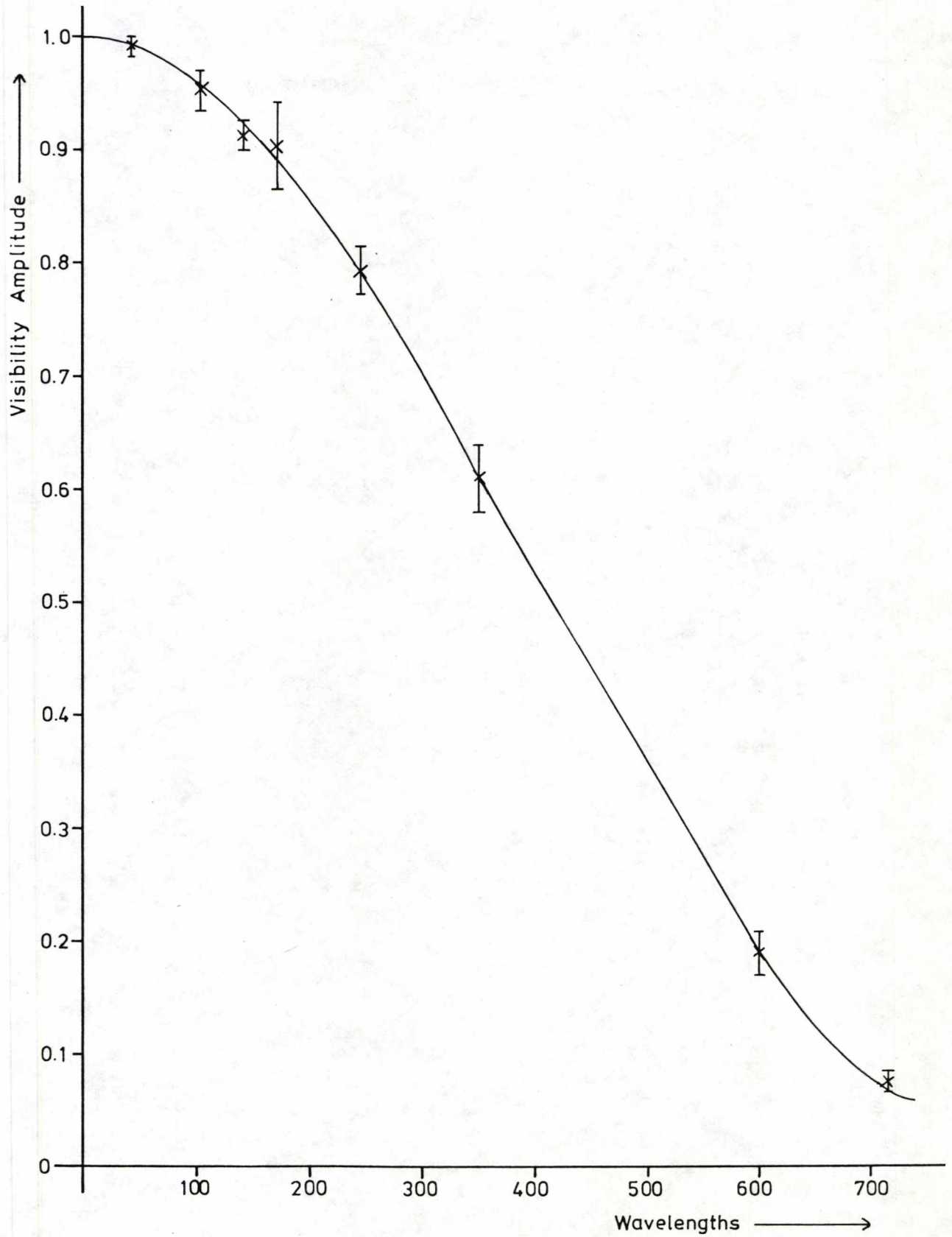


FIG. 5.1 Amplitude Of The Visibility Function Of Cassiopeia A

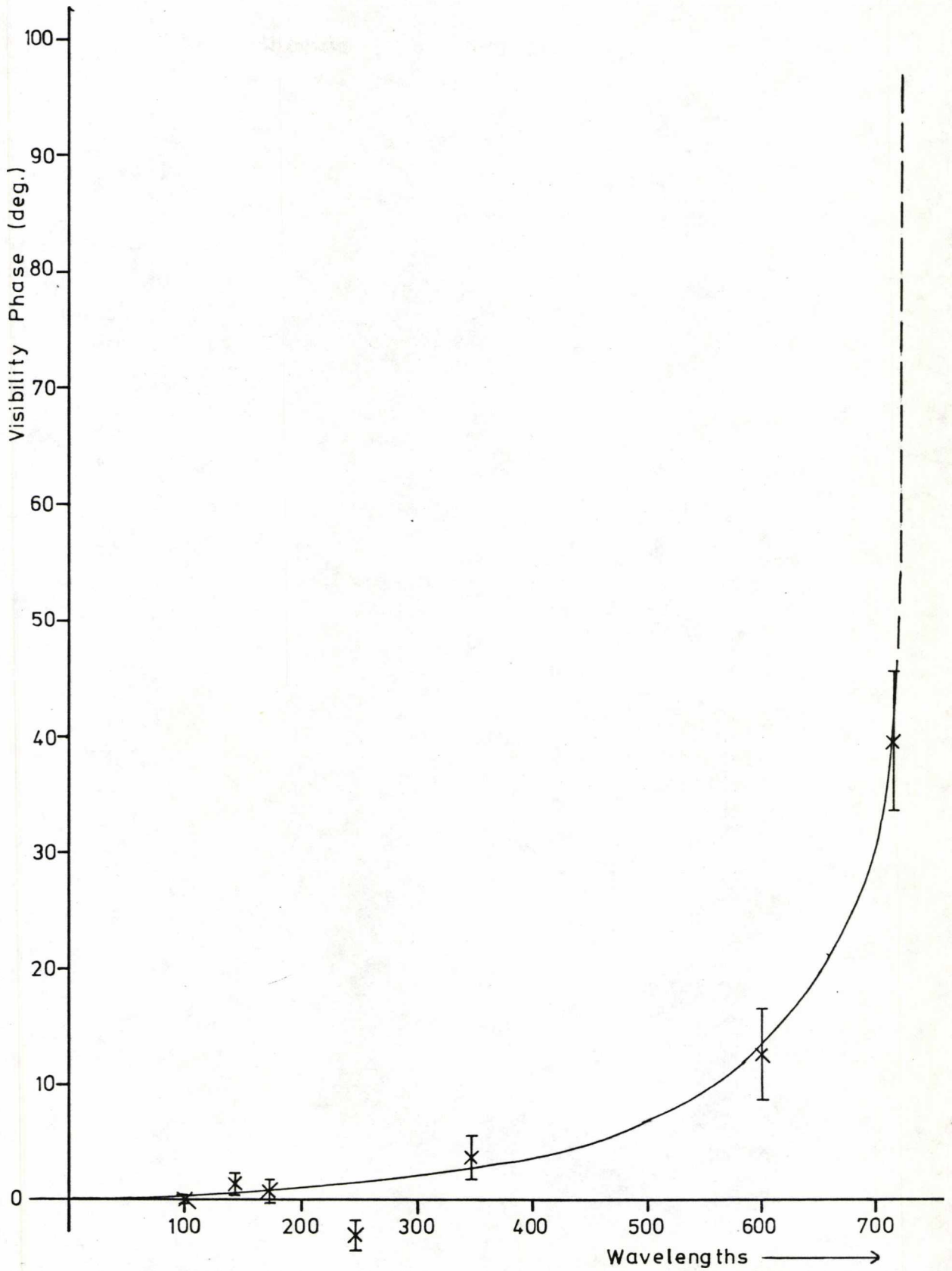


FIG. 5.2 Phase Of The Visibility Function Of Cassiopeia A

5.3 APPLICATION OF FOURIER TRANSFORMS TO THE ANALYSIS

Equation (A2.3) of Appendix 2 can be rewritten as a function of a single angular parameter θ , suitable for the present one-dimensional determination of the complex visibility function. Hence:

$$V(n) = \int_{-\infty}^{\infty} I(\theta) \exp 2\pi n i \theta \, d\theta \quad (5.1)$$

Clearly the brightness distribution, $I(\theta)$ is simply the inverse Fourier transform of the visibility function and hence the source structure can be recovered by performing the inverse transform associated with equation (5.1):

$$I(\theta) = \int_{-\infty}^{\infty} V(n) \exp -2\pi n i \theta \, dn \quad (5.2)$$

Equation (5.2) can be expressed in terms of discrete observations, a more suitable description of the present work:

$$I(\theta) = \sum_{k=1}^N w_k V(n_k) \exp -2\pi n_k i \theta \quad (5.3)$$

where $V(n_k)$ is the complex visibility of the k -th baseline and w_k is the weighting associated with each point such that the corresponding beam, synthesized by the measurements, is expressed by:

$$P(\theta) = \sum_{k=1}^N w_k \exp -2\pi n_k i \theta \quad (5.4)$$

To perform a discrete Fourier transform usually requires that the input data points be spaced at regular intervals. To further this aim, the complex visibilities at a regular grating interval were interpolated from the graphs reproduced in Figs. 5.1 and 5.2 by simply reading off the values at regular intervals. This method of interpolation was favoured to the more usual methods, in which least squares are used to approximate functions to the visibility curve (Meisel 1978), because of its simplicity. Since it is reasonable to assume that the Fourier transform of Cassiopeia A up to the first minimum before any fine structure is resolved, follows a well behaved function, accurate interpolation of the function should be possible if a reasonable number of data points are available which unambiguously define the form of that function. This criterion seemed to be well satisfied since the measured data points were relatively numerous and because the visually estimated best fit lines, representing the complex visibility function, lay reasonably close to the data points.

A grid-interval of 100λ was chosen so that the first grating lobes of the discrete transform were at a distance of 34arcmin. from the map phase centre, well outside the area of the nebula and any possible asymmetrical component. The aliasing due to the gridding was therefore negligible in the central field of view.

The results of the interpolation are tabulated in Table 5.5 (see page 83) in both their rectangular and spherical representations. Using the complex co-ordinate

Spacing (λ)	Visibility Function			
	amplitude	phase	real	imaginary
0	1.000	0.0 ^o	1.000	0.0
100	0.960	0.2 ^o	0.960	0.003
200	0.860	0.8 ^o	0.860	0.012
300	0.703	1.8 ^o	0.703	0.022
400	0.530	3.3 ^o	0.529	0.031
500	0.360	6.5 ^o	0.358	0.041
600	0.191	12.5 ^o	0.186	0.041
700	0.075	31.0 ^o	0.064	0.039

TABLE 5.5 : Visibility Function of Cassiopeia A
- Interpolated

form of the data of Table 5.5 in the discrete transform program of Appendix 3, the synthesized brightness distribution reproduced in Fig. 5.3 resulted. This distribution, the result of the true brightness distribution convolved with a sinc beam of half-power width 2.47 arcmin., shows a mainly symmetrical structure with a small component in the east. The asymmetry of the source is best illustrated by reflecting the structure west of the centre of the nebula main body in a line through this centre, which itself is clearly displaced by about 0.1 arcmin. from the map phase centre. Because of the width of the convolving beam the position of the asymmetrical component is very much uncertain but it would appear to be centred approximately 260 arcsec. east of the nebula main body centre.

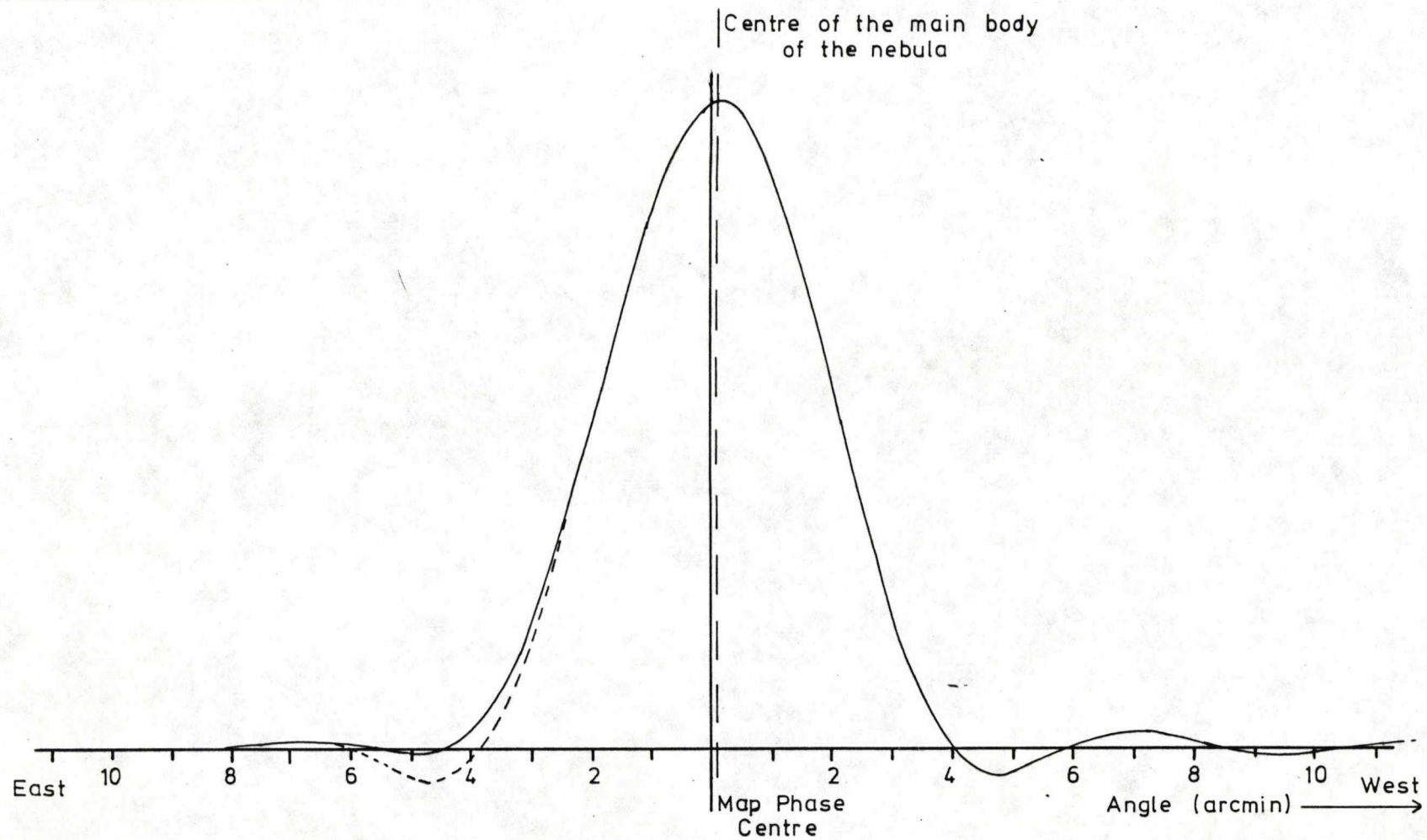


FIG. 5.3 Synthesized Brightness Distribution Of Cassiopeia A
 — Uniform Weighting

Because of the negative sidelobes present in the synthesized map, which of course have no physical meaning, a second series of transforms was performed using a linear weighting function with a cut-off at 1,600 wavelengths and zero weighting at baselines of 900λ and over. The weighting coefficients, w_k , are tabulated in Table 5.6, and the convolving beam realized with this set of w_k is plotted and compared with the original sinc beam in Fig. 5.4. Fig. 5.4 illustrates that although the new beam is approximately 20% wider, the primary side-lobes are reduced by 50%.

Baseline (λ)	w_k
0	1.000
100	0.938
200	0.875
300	0.813
400	0.750
500	0.688
600	0.625
700	0.563
800	0.500
900 and over	0

TABLE 5.6 : Weighting Coefficients

Weighting the data points of Table 5.5 accordingly, and performing the transform, a second synthesized map of the brightness distribution results as shown in Fig. 5.5. It

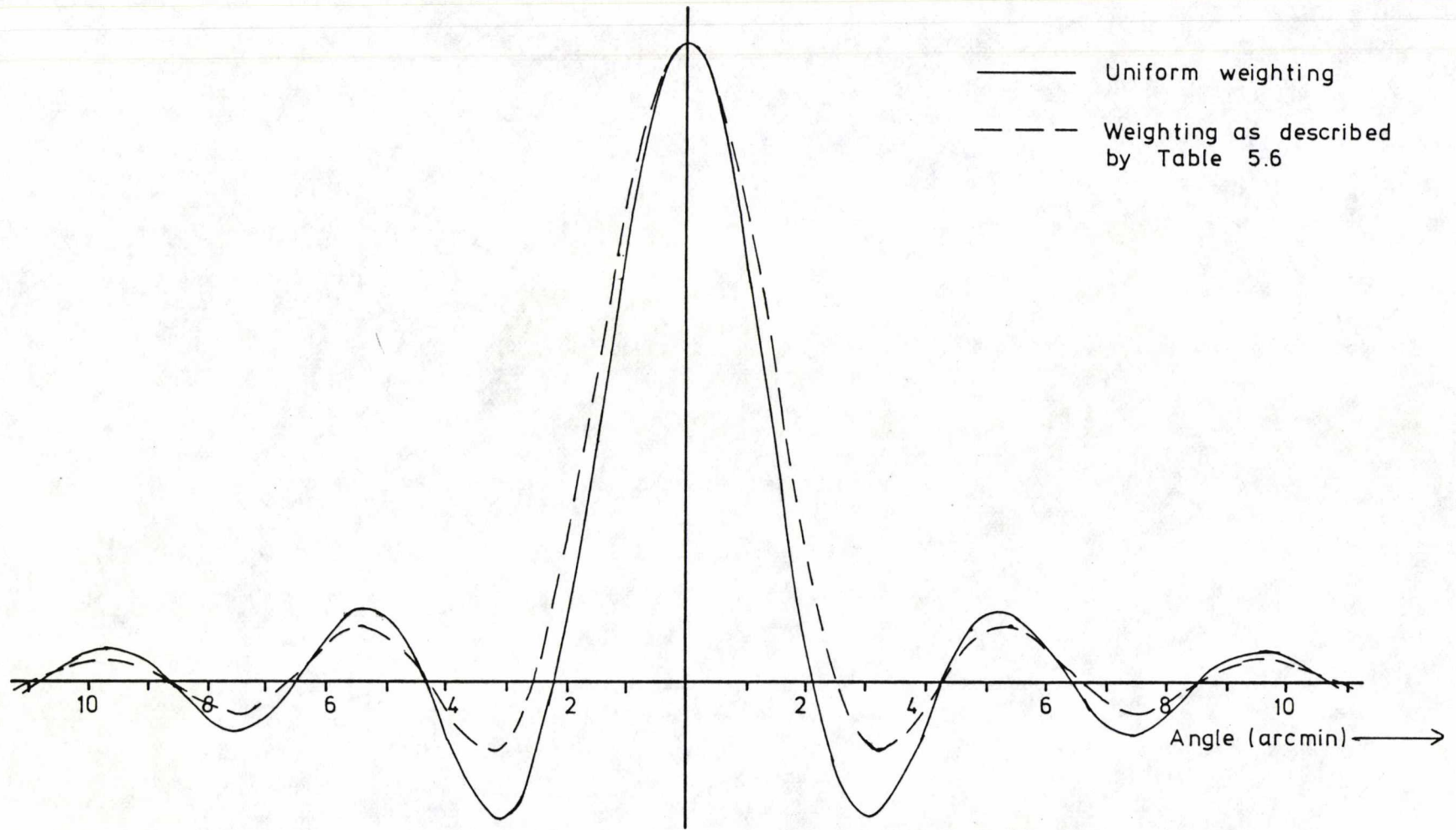


FIG. 5.4 Comparison Of The Two Convolver Beams

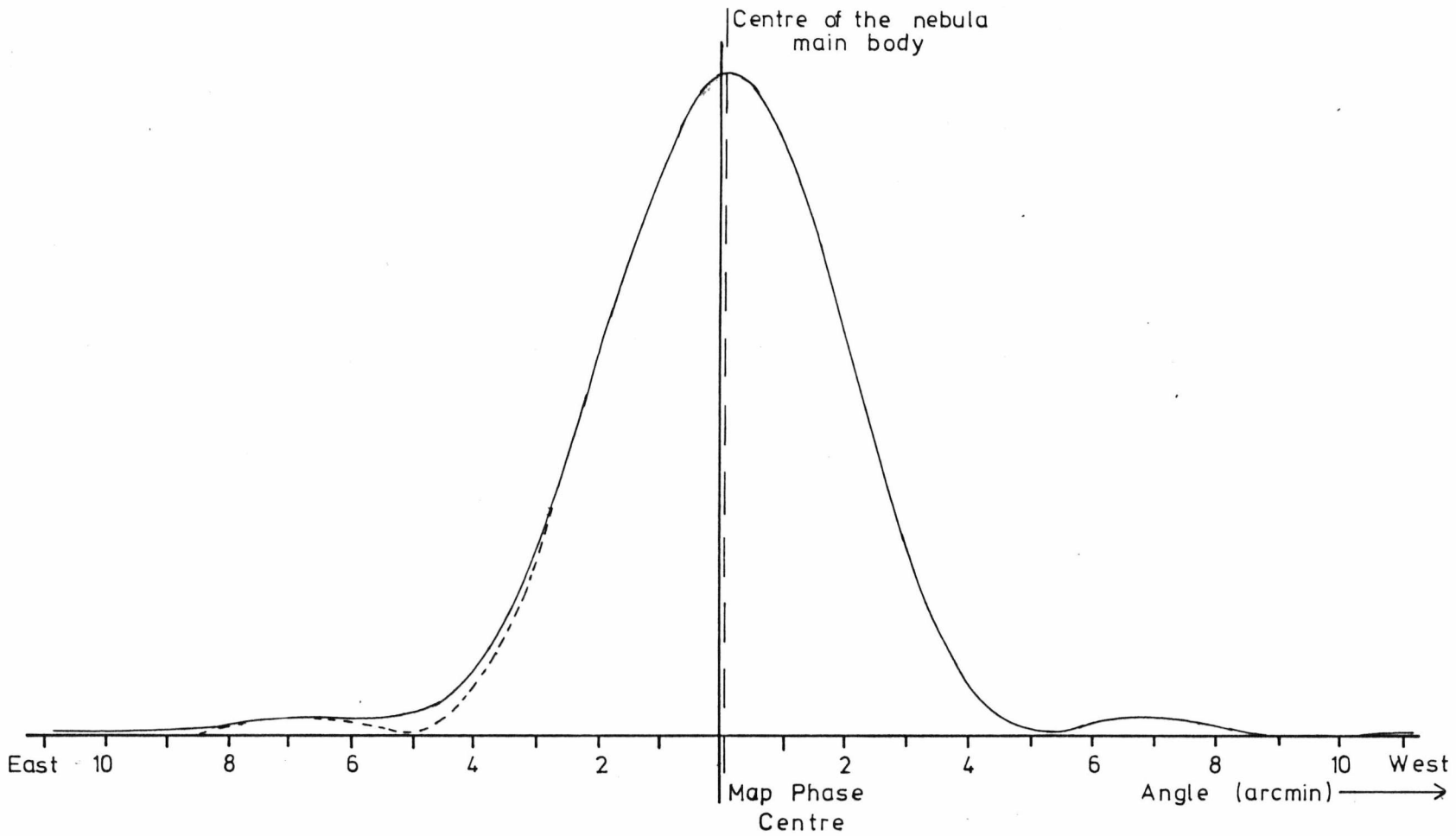


FIG. 5.5 Synthesized Brightness Distribution Of Cassiopeia A
— Nonuniform Weighting

can be immediately noticed that all the negative features of the first map have disappeared. The asymmetry noted in the original map is still present but, due to the wider beamwidth, has been smoothed out to a greater extent than before and displaced further east.

From the maps reproduced in Figs. 5.3 and 5.5 a tentative upper limit of about 5% can be placed on the percentage flux density of the asymmetrical component. However, the effect of the convolving beam in both cases is such that the width of the jet and its displacement from the main body of the nebula are of uncertain dimension.

5.4 COMPARISON WITH PREVIOUS WORK

Because of the difficulty in interpreting the synthesized map of Cassiopeia A, the results of two previous attempts by Jennison and Latham (1959) and Matheson (1973) to determine the complex visibility function of the nebula, were used to produce source distributions convolved to the same resolution. The results of the previous work, reproduced in Figs. 5.6 and 5.7, were interpolated to the same grid structure used above and weighted with the coefficients listed in Table 5.6. For completeness the results of the gridding are tabulated in Table 5.7 (see page 91). It should, however, be noted that the interpolation cannot be justified by the same arguments as the present work, and therefore, the two 'new' synthesized maps derived from the previous work, can only be interpreted as a rough indication of the

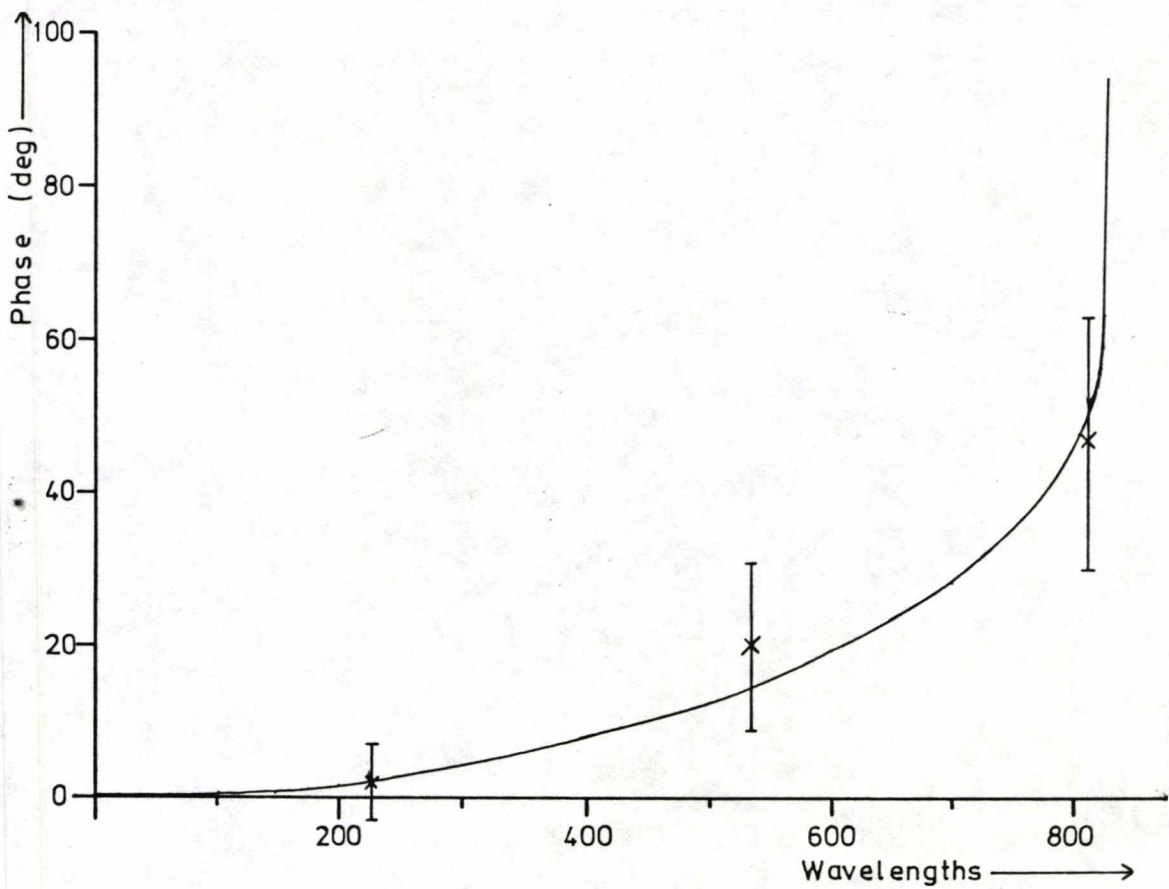
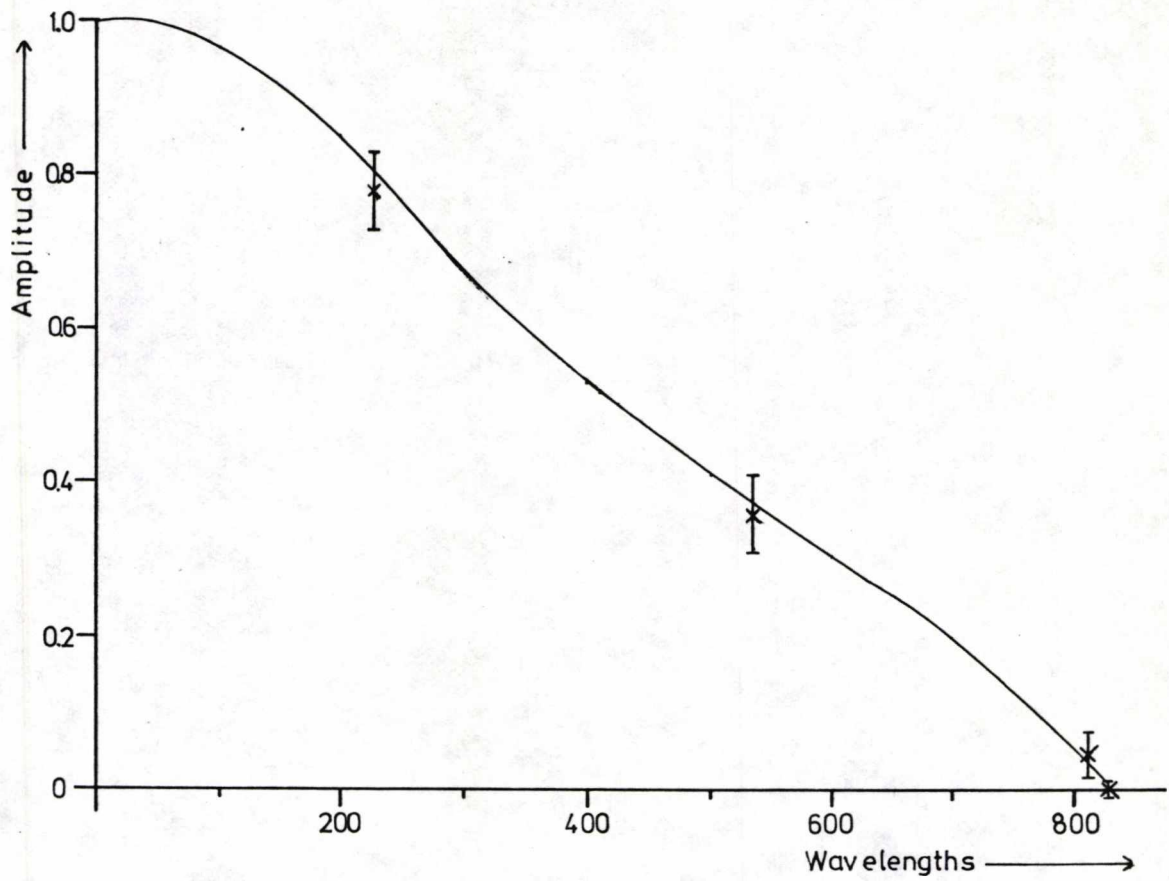


FIG. 5.6 Visibility Function Of Cassiopeia A
— Jennison & Latham (1959)

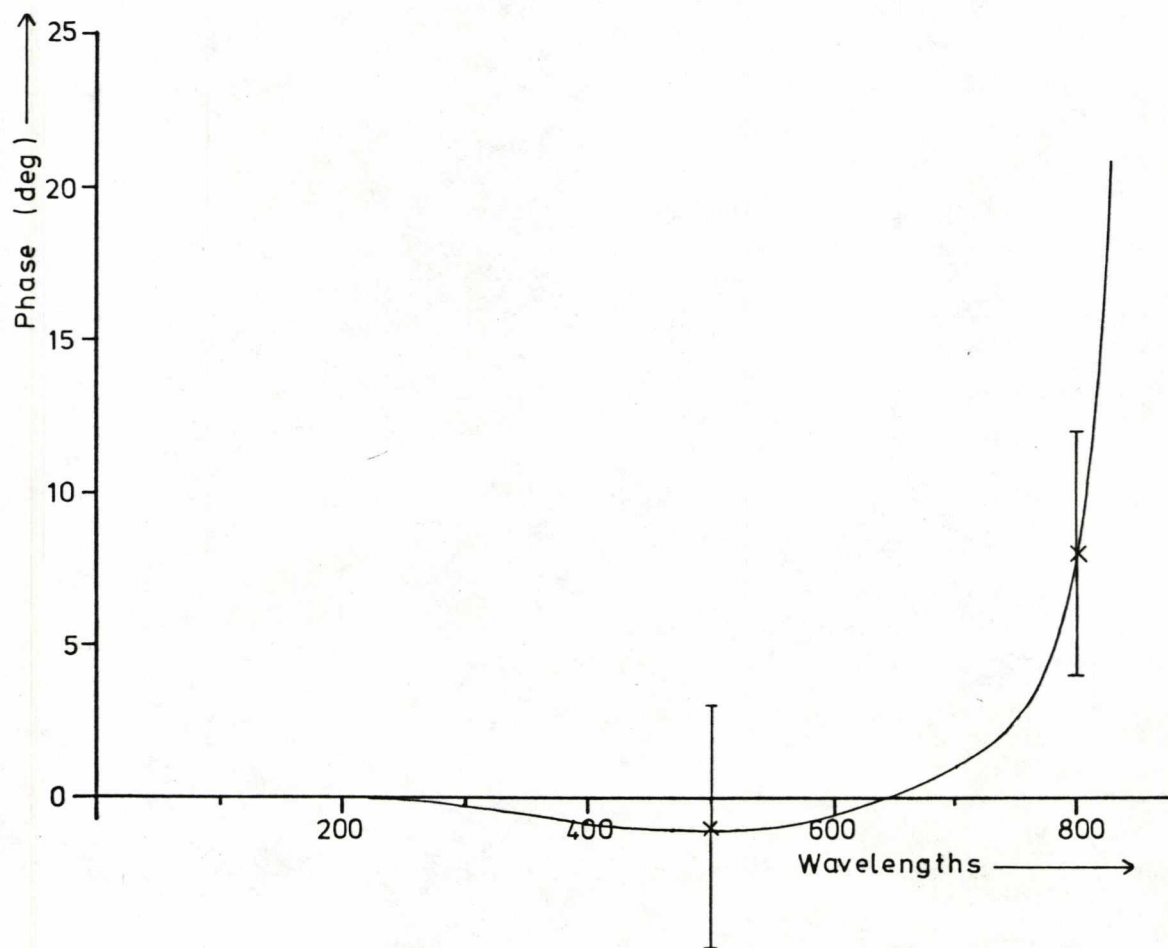
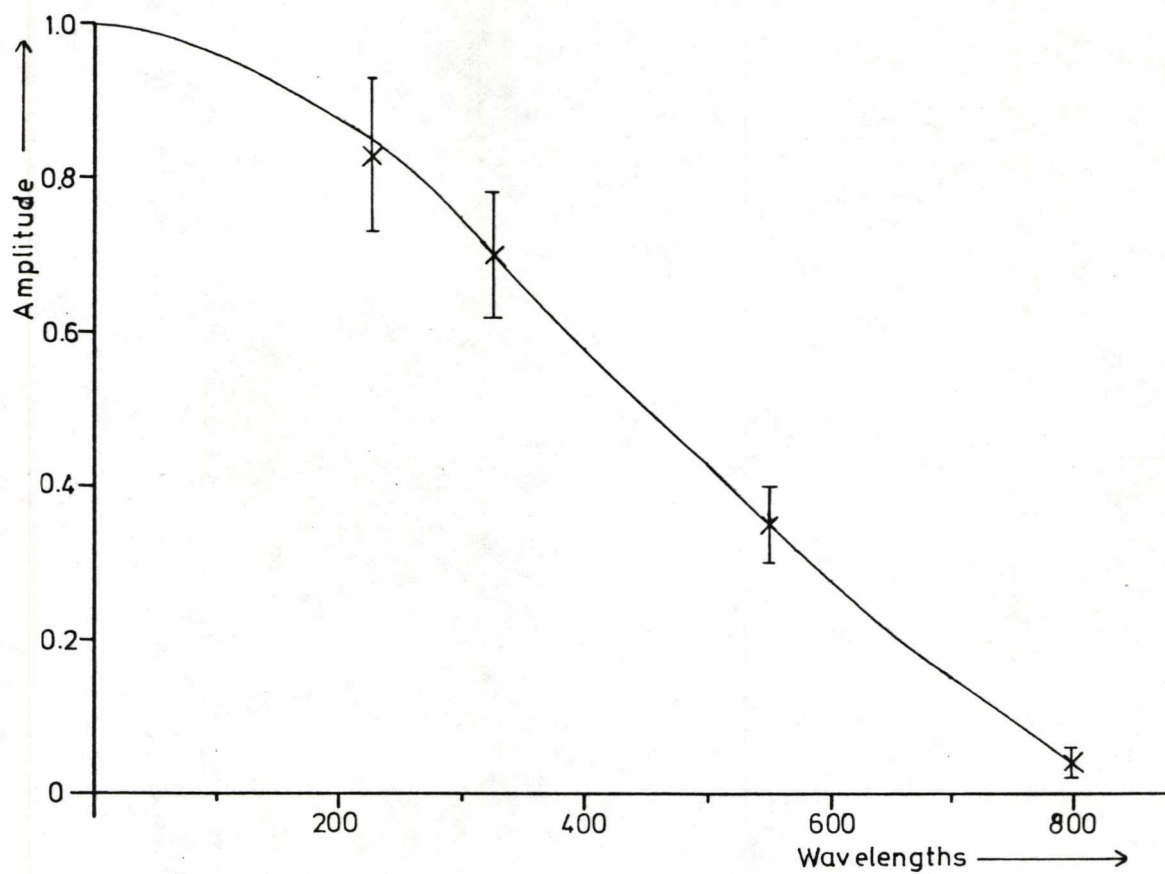


FIG. 5.7 Visibility Function Of Cassiopeia A
— Matheson (1973)

Baseline (λ)	Jennison & Latham (1959) at epoch 1956		Matheson (1973) at epoch 1973	
	amplitude	phase	amplitude	phase
0	1.000	0.0 $^{\circ}$	1.00	0.0 $^{\circ}$
100	0.965	0.5 $^{\circ}$	0.96	0.0 $^{\circ}$
200	0.850	1.8 $^{\circ}$	0.88	0.0 $^{\circ}$
300	0.675	4.5 $^{\circ}$	0.75	-0.2 $^{\circ}$
400	0.530	8.0 $^{\circ}$	0.58	-0.8 $^{\circ}$
500	0.410	12.7 $^{\circ}$	0.43	-1.0 $^{\circ}$
600	0.305	19.5 $^{\circ}$	0.28	-0.6 $^{\circ}$
700	0.200	26.5 $^{\circ}$	0.15	1.0 $^{\circ}$

TABLE 5.7 : Visibility Function of Cassiopeia A
Derived from Previous Work

convolved source structure determined from Jennison and Latham's and Matheson's data.

The result of superimposing the two synthesized brightness distributions on the distribution derived earlier is displayed in Fig. 5.8. It is clear from the map that the distribution at 38MHz lies somewhere in between those synthesized from the previous work. It should also be born in mind that the expansion of the remnant has not been taken into account and, to a great extent, this can explain the difference in width of the main body of the nebula between the three distributions. However it is not implausible from the present results that the emitting region at 38MHz is somewhat wider than at the two higher frequencies.

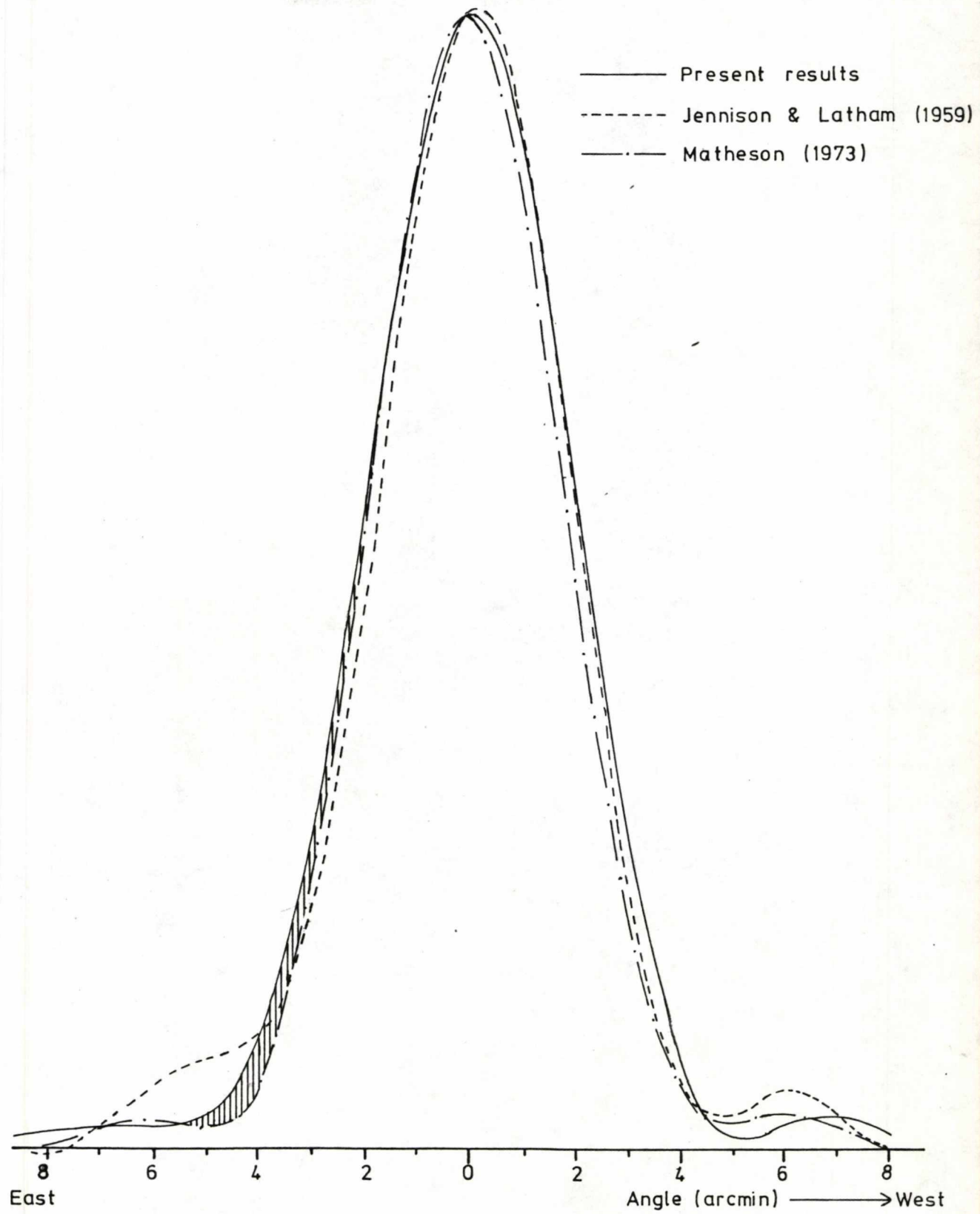


FIG. 5.8 Comparison Of Synthesized Brightness Distributions †

†Distributions not reduced to common epoch

Although it is obvious that the map phase centres of the three synthesized distributions are not in reality coincident, for ease of representation they have been assumed identical in position, and hence, it has been possible to shade in the area representing the asymmetrical component on the eastern edge of the remnant. The spur of Jennison and Latham's is clearly more pronounced than the jet of the present study and would appear to extend further from the main body of the nebula than the extension at 38MHz. In fact, the difference in form of the jet in the two distributions indicates the possibility of a significantly different structure of the asymmetrical component. It can also be concluded that the proximity of the jet of the present study to the main emission, has meant that the two components have been smoothed together by the convolving beam.

Clearly, if a Fourier transform is to be used to resolve the asymmetrical component from the main body of the remnant, the visibility function has to be mapped up to a much greater baseline in the spatial frequency domain.

CHAPTER 6

SOME MODEL FITTING

6.1 INTRODUCTION

With the present resolution it is difficult to assess the significance of the results of Chapter 5. Some asymmetry has been noted, but it is impossible to specify even the range of parameters that describe the source of the asymmetry from the synthesized maps. Clearly a model fitting procedure is desirable in which the experimentally determined visibilities can be compared with those derived by Fourier transforming a known brightness distribution. In effect, such a procedure necessarily gives a "better resolution" since no longer is the visibility function at spatial frequency points greater than the maximum spacing assigned to zero. On the other hand, with the maximum spatial frequency of the present study as low as 715λ , the model fitting procedure cannot yield a convergent solution and clearly a family of models will exist, each model agreeing well with the measured data.

Since the spatial frequency coverage of the present study was fairly limited, it was considered sufficiently accurate to use a simple two component, four parameter model to describe the source brightness distribution, specified by the width, y , of the asymmetrical component and its separation, e , from the main body of the nebula of

relative flux density, r , and width, w . The complex visibility function, V , is thus a non-linear function of the source parameters, r , w , y and e , which can be optimized using a non-linear least squares method until a reasonable fit is obtained between the observed and model visibilities.

Now a measure of the goodness of fit can be defined by:

$$\chi^2 = \sum_{k=1}^N \left| \frac{V'_k - V_k(r, w, y, e)}{\sigma_k} \right|^2 \quad (6.1)$$

...from Bevington (1969)

where V'_k is the experimentally determined visibility for the k -th baseline, σ_k is the error in V'_k and $V_k(r, w, y, e)$ is the visibility for the k -th baseline for a model of parameters r , w , y and e .

Equation (6.1) can be minimised with respect to r , w , y and e leading to a set of four non-linear simultaneous equations:

$$\frac{\partial}{\partial r} \sum_{k=1}^N \left| \frac{V'_k - V_k(r, w, y, e)}{\sigma_k} \right|^2 = 0 \quad (6.2)$$

$$\frac{\partial}{\partial w} \sum_{k=1}^N \left| \frac{V'_k - V_k(r, w, y, e)}{\sigma_k} \right|^2 = 0 \quad (6.3)$$

$$\frac{\partial}{\partial y} \sum_{k=1}^N \left| \frac{V'_k - V_k(r, w, y, e)}{\sigma_k} \right|^2 = 0 \quad (6.4)$$

$$\frac{\partial}{\partial e} \sum_{k=1}^N \left| \frac{V'_k - V_k(r, w, y, e)}{\sigma_k} \right|^2 = 0 \quad (6.5)$$

By the method of least squares the solution of equations (6.2 - 6.5) gives the best fit parameters r , w , y and e . Clearly the equations are difficult to solve and therefore in practice χ^2 , which describes a hypersurface in 4-dimensional space, must be minimised by an iterative search procedure.

However, it has already been mentioned above, that a single convergent solution is not expected due to the limited data available. Hence a brute-force search procedure was adopted to locate the many minima, mapping χ^2 for a wide range of samples in parameter space. In fact, had an iterative least squares program been used, a brute-force search would still have been necessary to confirm that no minima had been omitted.

6.2 THE 2-COMPONENT, 4-PARAMETER MODEL

In model fitting procedures, Gaussian shaped components are usually used (Fomalont and Wright 1974), but any models expected to describe reasonably the source distribution, are satisfactory - as long as they have convenient transforms.

In the present study, a rectangular brightness distribution was used to describe the main body of the nebula following the models used by Jennison (1959) and Matheson (1974). Also, as mentioned in Chapter 5, the visibility function at high frequencies is known to follow the form of a sinc function (Lequeux 1962), the transform of

which gives a rectangular source distribution. Such a distribution can be unambiguously specified by its width 'w' and normalized flux density 'r'.

As a model of a possible jet, a second rectangular distribution was considered satisfactory, since it could both represent a point source (if the width parameter is accordingly set to zero) and an extended source as suggested by both optical studies and the work of Jennison and Latham (1959). With the present resolution, a compact Gaussian asymmetrical component is still consistent with the point source model since neither are resolved at the present maximum spatial frequency and therefore, the use of such a Gaussian model in preference to the simpler delta function is of no advantage in the model fitting. The second rectangular distribution can be specified by its width 'y', its relative flux density '1-r' and finally, its distance from the phase centre of the map 'e'.

$I(\theta)$ for this two component, four parameter model is illustrated in Fig. 6.1. The Fourier transform of the model can easily be calculated for use in a model fitting procedure.

Initially consider x, the distance of the main body of the nebula from the phase centre of the total distribution. 'x' can be found by taking moments around the phase centre:

$$(1-r)y + (r/(2w))(w/2 - x)^2 = (r/(2w))(w/2 + x)^2$$

$$\Rightarrow x = y(1/r - 1)$$

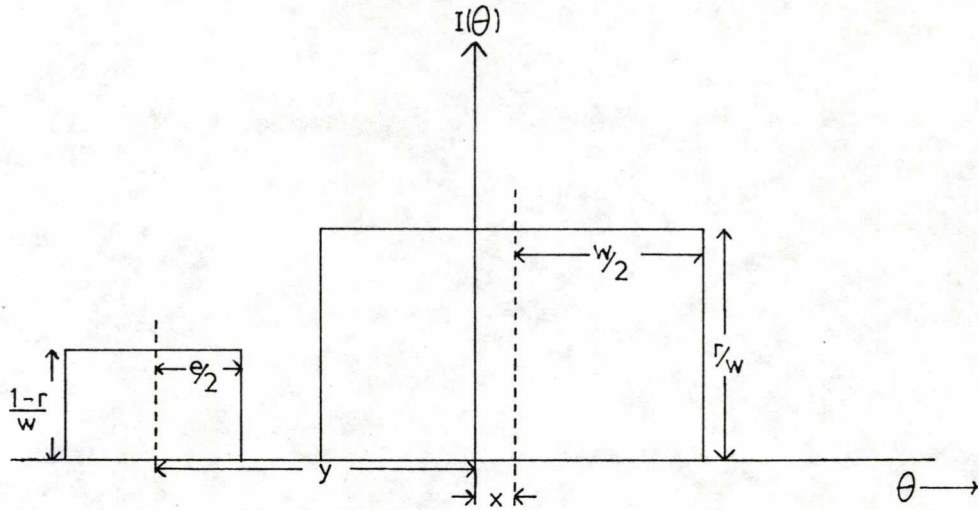


FIG. 6.1 Schematic Model Brightness Distribution

The Fourier transform of a brightness distribution, $I(\theta)$, is given by equation (5.1). Hence the Fourier transform of the main component becomes:

$$V^1(n) = r \operatorname{sinc}(\pi n w) \exp(2\pi n i x)$$

and that of the secondary source:

$$V^2(n) = (1-r) \operatorname{sinc}(\pi n e) \exp(-2\pi n i y)$$

Hence the Fourier transform of the model is given by:

$$V_k(r, w, y, e, n) = r \operatorname{sinc}(\pi n w) \exp(2\pi n i y \frac{1-r}{r}) + (1-r) \operatorname{sinc}(\pi n e) \exp(-2\pi n i y) \quad (6.6)$$

The calculation of $V_k(r, w, y, e, n)$ for each set of parameters over some desired range in parameter space is an extremely laborious process even before the calculation of χ^2 . Hence calculations were performed on a PDP11-40 computer running

under a UNIX version 6 operating system.

Finally, it should also be stressed that because of the limited resolution, the double rectangular form of the model distribution is but one of several that would have adequately described the expected source structure. For the reasons given above the present form was adopted, but it is likely that reasonable solutions would have been found had a different form of model distribution been chosen e.g. a disc distribution representing the main body of the nebula. However it is equally correct to state that a more complex form of model distribution, with perhaps three or four components, could not have been justified for precisely the same reason, namely the limited resolution. Hence, the solutions derived with the present model fitting procedures, are only representations of the general form of the source structure.

6.3 THE MODEL FITTING IMPLEMENTED

In Section 6.1, it was stated that a brute-force method was adopted to evaluate χ^2 , given by equation (6.1), over a range of parameters, each equally incremented. This equation can be rewritten in terms of the amplitude and phase of the relevant visibilities:

$$\begin{aligned} \chi^2 &= \sum_{k=1}^N \left| \frac{1}{\sigma_k} (F'_k \exp i \Psi'_k - F_k(r,w,y,e) \exp i \Psi_k(r,w,y,e)) \right|^2 \\ &= \sum_{k=1}^N (1/\sigma_k^2) \left[(F'_k \cos \Psi'_k - F_k(r,w,y,e) \cos \Psi_k(r,w,y,e))^2 \right. \\ &\quad \left. + (F'_k \sin \Psi'_k - F_k(r,w,y,e) \sin \Psi_k(r,w,y,e))^2 \right] \quad (6.7) \end{aligned}$$

The terms inside the square brackets of equation (6.7) simply represent the squares of the differences between the real and imaginary components of the measured and model visibility function for the k-th baseline. Since two different errors arose from the two procedures used for determining the amplitude and phase of the visibility function, the error term ' σ_k^2 ', can be rewritten as the square of the relevant error for each of the real and imaginary measured results, $R_{\sigma_k}^2$ and $I_{\sigma_k}^2$.

Hence, χ^2 , given by equation (6.8) below, can be calculated by treating the real and imaginary terms of the measured and model visibilities separately and summing the results.

$$\chi^2 = \sum_{k=1}^N \left[\frac{1}{R_{\sigma_k}} (R'_k - R_k(r,w,y,e)) \right]^2 + \sum_{k=1}^N \left[\frac{1}{I_{\sigma_k}} (I'_k - I_k(r,w,y,e)) \right]^2 \quad (6.8)$$

In equation (6.8), $R_k(r,w,y,e)$ and $I_k(r,w,y,e)$, the real and imaginary components of the model visibility, are given by equations (6.9) and (6.10), derived by rewriting equation (6.6).

$$R_k(r,w,y,e) = r \operatorname{sinc}(\pi n w) \cos(2\pi n y \frac{1-r}{r}) + (1-r) \operatorname{sinc}(\pi n e) \cos(2\pi n y) \quad (6.9)$$

$$I_k(r,w,y,e) = r \operatorname{sinc}(\pi n w) \sin(2\pi n y \frac{1-r}{r}) + (1-r) \operatorname{sinc}(\pi n e) \sin(2\pi n y) \quad (6.10)$$

The evaluation of equation (6.8) was realized by writing the relevant program in the C-language, which could subsequently be run on a PDP11-40 computer system.

Since three sets of results were available i) the

closure results, ii) the visibilities reconstructed from the closure results and iii) the visibilities derived from the graphs reproduced in Figs. 5.1 and 5.2 at a regular grid interval of 100λ , it was considered worthwhile to perform independent mappings of the χ^2 hypersurface for each set of data. It was, of course, born in mind that both the reconstructed results and the derived graph data had been obtained from the actual observables - the closure results. However, a comparison of the parameters giving rise to minima in χ^2 could effectively establish:

- A) The consistency of the procedure reconstructing the visibility function from the closure results, particularly the parabolic interpolation at short spacings; and
- B) The validity of two rectangular distributions as an accurate representation of the form of the source structure.



The program which performed the model fitting is reproduced in Appendix 4. The main routine, lines 82-276, calls on four subroutines:

- A) model(), lines 379-433, which calculates χ^2 for the visibilities reconstructed from closure results;
- B) trial(), lines 436-493, which calculates χ^2 for the visibilities interpolated at a regular grid interval;
- C) close(), lines 496-585, which calculates χ^2 for the

closure data;

- D) `search()`, lines 279-375, which implements the mapping of χ^2 for all possible permutations of the four parameters, each incremented over a specified range.

A number of extra facilities, besides the basic implementation of equation (6.8) have been built into the program. The preamble, lines 1-80, lists the options available. Two options for mapping χ^2 have been incorporated into the program. 'table -s' implements `search()`. 'table -a' with internal option '0', calculates χ^2 for a set of input parameters and then proceeds to map the value of χ^2 for one parameter incremented in turn around the original input set. The latter routine was found useful in determining a local minimum of χ^2 more precisely. Although this method assumed the variation of χ^2 with each parameter to be independent of the other three, the saving in computer time over the '`search()`' routine was considerable.

The other internal options permit the printing out of both the model and experimentally determined complex visibilities for corresponding spatial frequencies allowing a visual comparison of the results. In the case of closure data, the value of χ^2 associated with each real and imaginary point was available, as illustrated in Table 6.8 (see page 115).

6.4 MAPPING BASED ON CLOSURE DATA

The closure results listed in Table 5.1 were transformed into real and imaginary complex co-ordinates, a form suitable for the calculation of χ^2 , and this representation of the closure data is tabulated in Table 6.1.

k	baseline (λ)	R'_k	$\pm R_{\sigma k}$	I'_k	$\pm I_{\sigma k}$
1	44	0.992	0.008	0.000	0.017
2	104	0.961	0.007	0.002	0.018
3	143	0.917	0.008	0.020	0.015
4	172	0.966	0.012	0.012	0.012
5	247 i	0.905	0.010	-0.059	0.010
6	247 ii	0.759	0.009	-0.069	0.011
7	352	0.801	0.009	0.096	0.010
8	600	0.243	0.003	0.052	0.003
9	715	0.0132	0.0006	0.0097	0.0036

TABLE 6.1 : Complex Co-ordinate Representation of the Closure Visibilities

A single search of parameter space for minima in χ^2 , was performed using the program referred to in the above section. The χ^2 variable 'X(3)' was evaluated for 13,662 points in parameter space, the limits and increments of each parameter as specified in Table 6.2 (see page 104).

	nebula main body		2nd component	
	flux -r- ratio	width -w- (rad.)	distance from -y- phase centre	width -e- (rad.)
minimum	0.91	1.28×10^{-3}	-1.57×10^{-3}	0
maximum	0.99	1.38×10^{-3}	3.07×10^{-3}	6.8×10^{-4}
increment	0.01	1.00×10^{-5}	1.00×10^{-4}	3.4×10^{-4}

TABLE 6.2 : Parameter Space Searched for Minima in X(3)

Considering the range of each parameter in turn:

- r- The limits allowed for a "jet" flux density of 0% to 9% of the total distribution. This range was approximately consistent with much of the previous work on Cassiopeia A, both at high frequencies (0%) and low frequencies (10% suggested by Jennison and Latham (1959), less than 2% by Matheson (1974) and less than 10% suggested by Hutton et. al. (1974)).
- w- In 1956, Jennison and Latham (1959) determined the first minimum of the visibility function to lie at 840λ . Using a rectangular brightness distribution model and assuming an undecelerated expansion of the nebula since its explosion in 1657 (Kamper and Van der Bergh 1976), gives rise to an expected angular size of 266 arcsec. (1.29×10^{-3} rad.) at epoch 1980. The range of this parameter was set such that the limits encompassed this estimate and allowed for a larger

emitting region at 38MHz than at higher frequencies up to a maximum of approximately 4.75 arcmin.

- y- Hutton et. al. (1974), expecting a point source to give considerable improvement to their models, searched the area 300 arcsec. west to 600 arcsec. east of their map centre for a good fit and found solutions in three distinct regions. The present work varied the 'y' parameter over a slightly greater range (323 arcsec. W. to 633 arcsec. E.), although from the synthesized map of Fig. 5.8, solutions were expected in the very much smaller range, 148 arcsec. E. to 320 arcsec. E.
- e- The parameter associated with the width of a possible asymmetrical component was varied up to a maximum of approximately 140 arcsec., allowing representations of both a compact source and an extended source.

The 55 points with the lowest value of χ^2 parameter, $X(3)$, resulting from the search of parameter space are tabulated in Table 6.3 (see pages 106/7). It is difficult to assess the degree of convergence of the least squares method in its present application. However, it is probably reasonable to assume that the minima of Table 6.3 with $X(3)$ less than 200, are an accurate representation of the solutions of equations (6.2 - 6.5). These points are again reproduced in Table 6.4 (see page 108), and the values of the χ^2 parameter, $X(3)$, can be compared with those evaluated for a symmetrical Cassiopeia A distribution by referring to Table 6.5 (see page 110).

nebula main body		2nd component		X(3)
flux ratio	width (r)	distance from phase centre(r)	width (r)	
0.930	1.290E-3	8.700E-4	6.800E-4	201.83
0.930	1.300E-3	8.700E-4	6.800E-4	214.54
0.940	1.280E-3	8.700E-4	0.000	199.94
0.940	1.280E-3	8.700E-4	3.400E-4	204.00
0.940	1.290E-3	8.700E-4	0.000	208.42
0.940	1.290E-3	8.700E-4	3.400E-4	196.12
0.940	1.290E-3	8.700E-4	6.800E-4	207.10
0.940	1.300E-3	8.700E-4	3.400E-4	225.30
0.940	1.300E-3	8.700E-4	6.800E-4	192.23
0.940	1.310E-3	8.700E-4	6.800E-4	214.42
0.940	1.320E-3	9.700E-4	6.800E-4	223.24
0.950	1.290E-3	8.700E-4	0.000	205.49
0.950	1.290E-3	8.700E-4	3.400E-4	214.69
0.950	1.300E-3	8.700E-4	0.000	214.50
0.950	1.300E-3	8.700E-4	3.400E-4	209.48
0.950	1.310E-3	8.700E-4	6.800E-4	222.01
0.950	1.310E-3	9.700E-4	0.000	219.70
0.950	1.310E-3	9.700E-4	3.400E-4	214.42
0.950	1.310E-3	9.700E-4	6.800E-4	224.51
0.950	1.320E-3	9.700E-4	0.000	214.32
0.950	1.320E-3	9.700E-4	3.400E-4	202.62
0.950	1.320E-3	9.700E-4	6.800E-4	193.84
0.950	1.330E-3	9.700E-4	6.800E-4	201.35
0.950	1.340E-3	1.070E-3	6.800E-4	215.04
0.950	1.350E-3	1.070E-3	6.800E-4	223.92
0.960	1.310E-3	9.700E-4	0.000	216.69
0.960	1.320E-3	9.700E-4	0.000	192.05
0.960	1.320E-3	9.700E-4	3.400E-4	197.11

TABLE 6.3 : Results of the Closure Model Fitting

nebula main body		2nd component		X(3)
flux ratio	width (r)	distance from phase centre(r)	width (r)	
0.960	1.320E-3	9.700E-4	6.800E-4	226.21
0.960	1.330E-3	9.700E-4	0.000	205.41
0.960	1.330E-3	9.700E-4	3.400E-4	204.74
0.960	1.330E-3	9.700E-4	6.800E-4	217.27
0.960	1.330E-3	1.070E-3	3.400E-4	224.88
0.960	1.340E-3	1.070E-3	0.000	198.28
0.960	1.340E-3	1.070E-3	3.400E-4	194.26
0.960	1.340E-3	1.070E-3	6.800E-4	202.15
0.960	1.350E-3	1.070E-3	0.000	204.76
0.960	1.350E-3	1.070E-3	3.400E-4	201.46
0.960	1.350E-3	1.070E-3	6.800E-4	210.48
0.960	1.350E-3	1.170E-3	6.800E-4	224.59
0.960	1.360E-3	1.170E-3	0.000	219.35
0.960	1.360E-3	1.170E-3	3.400E-4	210.10
0.960	1.360E-3	1.170E-3	6.800E-4	214.01
0.960	1.370E-3	1.170E-3	0.000	220.38
0.960	1.370E-3	1.170E-3	3.400E-4	217.60
0.970	1.340E-3	1.070E-3	0.000	206.87
0.970	1.340E-3	1.070E-3	3.400E-4	216.53
0.970	1.350E-3	1.070E-3	0.000	212.35
0.970	1.350E-3	1.070E-3	3.400E-4	221.86
0.970	1.350E-3	1.170E-3	0.000	217.83
0.970	1.350E-3	1.170E-3	3.400E-4	223.07
0.970	1.360E-3	1.170E-3	0.000	201.05
0.970	1.360E-3	1.170E-3	3.400E-4	210.88
0.970	1.370E-3	1.170E-3	0.000	219.61
0.970	1.370E-3	1.270E-3	0.000	226.89

TABLE 6.3 : Results of the Closure Model Fitting (contd.)

nebula main body		2nd component		X(3)
flux (%)	width (arcmin)	distance from phase centre (arcsec)	width (arcsec)	
94	4.40	180	0	199.94
94	4.43	180	70	196.12
94	4.47	180	140	192.23
95	4.54	200	140	193.84
96	4.54	200	0	192.05
96	4.54	200	70	197.11
96	4.61	221	0	198.28
96	4.61	221	70	194.26

TABLE 6.4 : Best-fit Parameters (Closure Search)

Of particular interest is the range of the 'y' parameter in which all the solutions lie. This range, 180 arcsec. to 220 arcsec. east of phase centre, has been superimposed in Fig. 6.2 onto a one-dimensional representation of the emitting region distributed along a position angle of 83° , the mean of the present observations. The coincidence of Hutton et. al.'s position B with the present work is remarkable. If the present study has detected the same compact source postulated by Hutton et. al., the solutions with the 'e' parameter equal to zero and the 'y' parameter lying between 180 and 200 arcsec. E. listed in Table 6.4, would also be consistent with Hutton et. al.'s models. However the other minima cannot be ignored, and if an extended jet is present, it would have been resolved by Hutton et. al. and remained undetected. The present

NOTES

- 1) y-axis not to scale
- 2) x [nebula main body offset from phase centre] given by

$$x = y \left(\frac{1-r}{r} \right)$$
- 3) e_{max} represents the range of widths of the eastern component tested

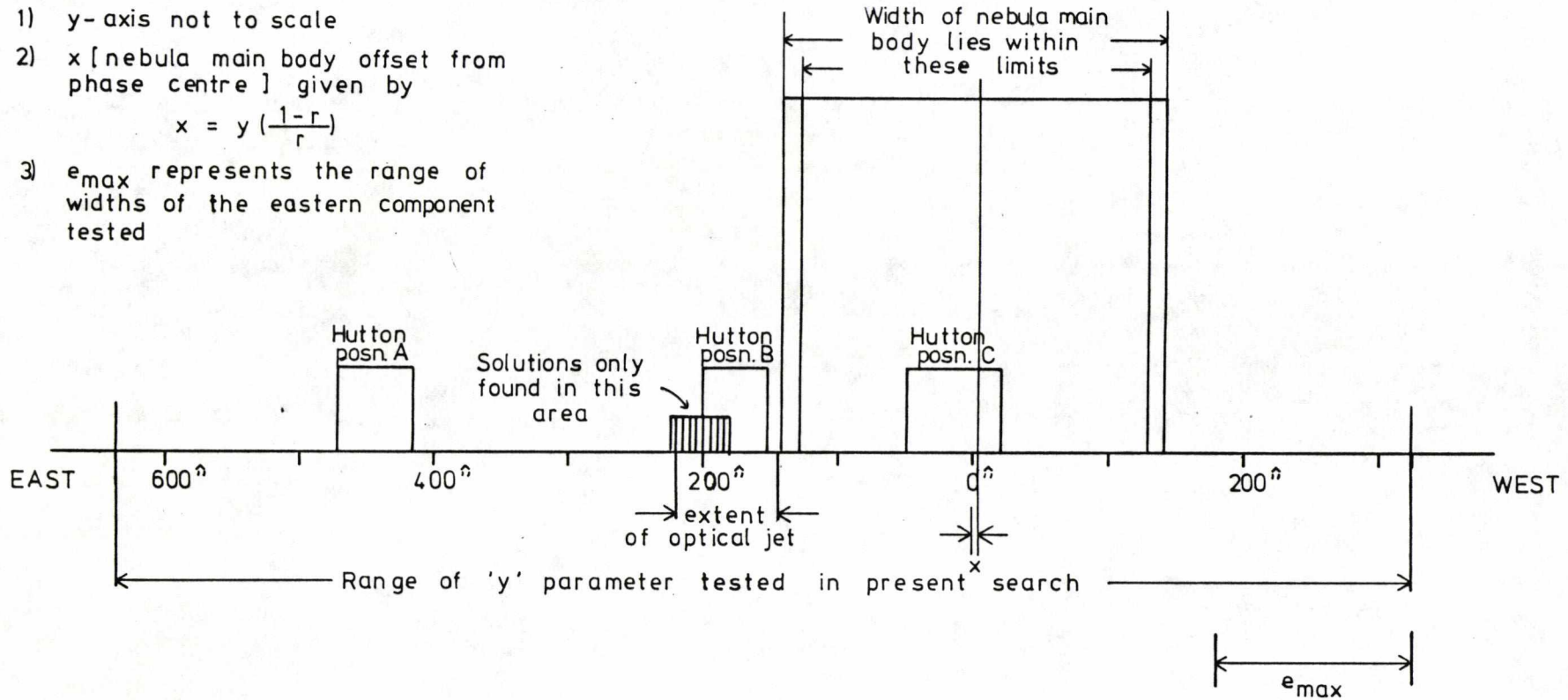


FIG. 6.2 A Graphical Representation Of The Results Of The Closure Model Fitting

Cassiopeia A width (10^{-3} radians)	X(3)	X(2)	X(1)
1.28	1961.11	112.54	72.77
1.29	1595.84	99.12	65.69
1.30	1303.88	86.91	59.61
1.31	1077.76	75.92	54.51
1.32	910.52	66.12	50.36
1.33	795.72	57.51	47.15
1.34	727.41	50.08	44.85
1.35	700.12	43.81	43.44
1.36	708.86	38.69	42.89
1.37	749.10	34.71	43.20
1.38	816.75	31.86	44.32

TABLE 6.5 : χ^2 Evaluated for Symmetrical Source Distributions

resolution also forbids any more than a passing suggestion, that there may be a relationship between the point source of Hutton et. al. (1974) and the present study.

Assuming a rectangular brightness distribution along the axis of position angle 83° , for the main body of Cassiopeia A, the results of the closure search can be summarised as follows:

- 1) As the jet flux is decreased from 6% to 4% of the total flux density, its separation from the main body of the nebula is increased from approximately 180 arcsec. to 220 arcsec. east of phase centre.

- 2) As the jet flux is decreased from 6% to 4%, the width of the main body of the nebula is increased from 4.40 arcmin. to 4.61 arcmin.
- 3) With the present resolution, the width of the jet is still as yet undetermined and both point and extended source solutions remain consistent.

6.5 MAPPING BASED ON RECONSTRUCTED VISIBILITY DATA

The data of the reconstructed visibility function, listed in Table 5.4, were transformed into real and imaginary complex co-ordinates for use in the least squares routine. This representation of the data is tabulated in Table 6.6 below.

k	baseline (λ)	R'_k	$\pm R\sigma_k$	I'_k	$\pm I\sigma_k$
1	44	0.992	0.008	0.000	0.010
2	104	0.954	0.014	0.000	0.002
3	143	0.912	0.014	0.020	0.018
4	172	0.904	0.041	0.012	0.015
5	247	0.792	0.023	-0.045	0.019
6	352	0.610	0.034	0.040	0.024
7	600	0.187	0.020	0.043	0.017
8	715	0.057	0.015	0.048	0.014

TABLE 6.6 : Complex Co-ordinate Representation of the Reconstructed Visibilities

χ^2 was evaluated for the same parameter space searched in the previous section, by using the 'table -s 1' option of the program reproduced in Appendix 4. The minima found in the mapping of χ^2 are tabulated in Table 6.7 (see page 113), with X(1) representing the value of the χ^2 parameter. For comparison purposes the values of X(1), calculated for a symmetrical source, can be found by referring to column X(1) of Table 6.5 (see page 110).

It is not surprising to find some difference between the convergence of the two mappings (c.f. Table 6.7 with Table 6.4), since the errors in the reconstruction of the visibility function from closure data are cumulative. However, there is an excellent agreement between the parameters giving rise to the minima found by the two mappings, in that all the points bar two in Table 6.4 correspond to points in Table 6.7. This would tend to confirm that the parabolic interpolation used in the reconstruction process, was a good approximation to the actual visibility function at short baselines. It is also interesting to note that the same point in parameter space (a 4% point source, 200 arcsec. east of phase centre with the main body of Cassiopeia A of width 4.54 arcmin.) gives rise to the minimum χ^2 found by both mappings.

The difference in magnitude of χ^2 between the two mappings for the same parameters, was also investigated since it could not be explained by the difference in the number of degrees of freedom - 13 in the closure case and 11 in the mapping based on reconstructed data. The closure

nebula main body		2nd component		X(1)
flux ratio	width (r)	distance from phase centre(r)	width (r)	
0.940	1.280E-3	8.700E-4	6.800E-4	15.69
0.940	1.290E-3	8.700E-4	6.800E-4	14.78
0.940	1.300E-3	8.700E-4	6.800E-4	14.74
0.940	1.310E-3	8.700E-4	6.800E-4	15.54
0.950	1.290E-3	8.700E-4	0.000	15.63
0.950	1.290E-3	8.700E-4	3.400E-4	15.46
0.950	1.300E-3	8.700E-4	3.400E-4	15.44
0.950	1.300E-3	8.700E-4	6.800E-4	15.62
0.950	1.310E-3	8.700E-4	6.800E-4	15.66
0.950	1.310E-3	9.700E-4	6.800E-4	15.52
0.950	1.320E-3	9.700E-4	6.800E-4	15.30
0.960	1.310E-3	9.700E-4	0.000	14.94
0.960	1.310E-3	9.700E-4	3.400E-4	15.08
0.960	1.320E-3	9.700E-4	0.000	14.61
0.960	1.320E-3	9.700E-4	3.400E-4	14.63
0.960	1.320E-3	9.700E-4	6.800E-4	15.64
0.960	1.330E-3	9.700E-4	0.000	15.13
0.960	1.330E-3	9.700E-4	3.400E-4	15.03
0.960	1.330E-3	9.700E-4	6.800E-4	15.72
0.960	1.330E-3	1.070E-3	0.000	15.74
0.960	1.330E-3	1.070E-3	3.400E-4	15.66
0.960	1.340E-3	1.070E-3	0.000	15.55
0.960	1.340E-3	1.070E-3	3.400E-4	15.50
0.970	1.330E-3	1.070E-3	0.000	15.49
0.970	1.330E-3	1.070E-3	0.000	15.49
0.970	1.340E-3	1.070E-3	0.000	15.01
0.970	1.340E-3	1.070E-3	3.400E-4	15.53
0.970	1.350E-3	1.070E-3	0.000	15.38

TABLE 6.7 : Reconstructed Visibilities Model Fitting Results

visibility and the χ^2 associated with each spatial frequency was calculated by computer for a number of points in parameter space listed in Table 6.3. For reference, the computer output for the point P_{MIN} , ($r=0.96$, $w=4.54$ arcmin, $y=200$ arcsec, $e=0$), which gave rise to the minimum χ^2 , is reproduced in Table 6.8 (see page 115).

For all points in parameter space, the value of χ^2 for the imaginary component of the visibility at spatial frequencies of $247i$, $247ii$ and 352λ , (underlined in Table 6.8 for P_{MIN}) was anomalously large confirming the suspicion, voiced earlier in Section 5.1, that the negative phase at 247λ had a systematic error that had not been accounted for. It would also appear apparent from the present results that the positive closure phase at 352λ had a similar error. These anomalous results coincided with the possibility of phase errors referred to in Section 3.6, but no further steps were taken to check the results since it was unreasonable to devote a further considerable length of time correcting errors of small magnitude around zero degrees which provided little information as to the source structure, the baselines involved being short. Fortunately, since the errors were of opposite sign, neither the reconstruction of the phase at 600λ and 700λ nor the gridding of the visibility function, were significantly affected.

A further investigation of the possible effect on the model fitting was instigated by setting the relevant closure phases to zero and running two search programs

Base line	Real		Imag		Model	
	actual	model	actual	model	amp	phase
0.0 : R	1.000	1.000	I 0.000	0.000	1.000	0.00
104.0 : R	0.954	0.962	I 0.000	0.000	0.962	0.05
143.0 : R	0.912	0.930	I 0.020	0.002	0.930	0.14
172.0 : R	0.904	0.900	I 0.012	0.004	0.900	0.24
247.0 : R	0.792	0.802	I -0.045	0.010	0.802	0.73
352.0 : R	0.610	0.629	I 0.040	0.025	0.630	2.25
600.0 : R	0.187	0.197	I 0.043	0.055	0.205	15.68
715.0 : R	0.057	0.042	I 0.048	0.048	0.064	48.65

0 : R	1.000	1.000	I 0.000	0.000	1.000	0.00
100 : R	0.960	0.965	I 0.003	0.000	0.965	0.05
200 : R	0.860	0.866	I 0.012	0.006	0.866	0.38
300 : R	0.703	0.719	I 0.022	0.017	0.719	1.35
400 : R	0.529	0.543	I 0.031	0.033	0.544	3.43
500 : R	0.358	0.363	I 0.041	0.048	0.366	7.48
600 : R	0.186	0.197	I 0.041	0.055	0.205	15.68
700 : R	0.064	0.060	I 0.039	0.050	0.078	39.89

Base line	Least Squares		Real		Imag	
	actual	model	actual	model	actual	model
44 : R	0.022	I 0.000	R 0.992	0.993	I 0.000	0.000
104 : R	1.028	I 0.006	R 0.961	0.968	I 0.002	0.000
172 : R	1.812	I 0.575	R 0.966	0.950	I 0.012	0.003
143 : R	4.576	I 1.491	R 0.917	0.934	I 0.020	0.002
247 : R	0.822	I <u>45.577</u>	R 0.905	0.896	I -0.059	0.009
247 : R	3.033	I <u>48.187</u>	R 0.759	0.775	I -0.069	0.007
352 : R	2.701	I <u>56.407</u>	R 0.801	0.816	I 0.096	0.021
600 : R	13.946	I 3.060	R 0.243	0.254	I 0.052	0.057
715 : R	8.409	I 0.403	R 0.013	0.011	I 0.01	0.007

TABLE 6.8 : O/P of Program 'table' for Input Parameters, P_{MIN}

mapping parameter space in X(1) and X(3). The values of χ^2 were found to be significantly reduced but the majority of best-fit parameters remained the same, suggesting that the method of least squares is not seriously affected by systematic errors as long as these occur on only a small percentage of the total number of spatial frequencies.

Table 6.9 summarises the results (c.f. Table 6.4).

nebula main body		2nd component		X(1)	X(3)
flux (%)	width (arcmin)	distance from phase centre (arcsec)	width (arcsec)		
94	4.40	180	0	7.35	55.35
94	4.43	180	70	6.58	52.22
94	4.47	180	140	5.56	50.30
95	4.43	180	0	7.22	55.88
95	4.54	200	140	5.54	57.97
96	4.54	200	0	5.72	47.12
96	4.54	200	70	5.81	52.34

TABLE 6.9 : Chi-squared Parameters X(1) and X(3) -
Imaginary Visibilities Adjusted

6.6 MAPPING BASED ON GRIDDED DATA

Using the real and imaginary components of the complex visibilities listed in Table 5.5 for values of R_k' and I_k' respectively, χ^2 was evaluated for 2,673 points in parameter space, the limits and increments of each parameter as specified in Table 6.10. The range of the 'y' parameter

	nebula main body		2nd component	
	flux -r- ratio	width -w- (rad)	distance from -y- phase centre	width -e- (rad)
minimum	0.91	1.28×10^{-3}	6.7×10^{-4}	0
maximum	0.99	1.38×10^{-3}	14.7×10^{-4}	6.8×10^{-4}
increment	0.01	1.00×10^{-5}	1.0×10^{-4}	3.4×10^{-4}

TABLE 6.10 : Parameter Space Searched for Minima in X(2)

was considerably smaller than in previous mappings, since it had already been well established by the searches referred to in Sections 6.4 and 6.5. For all spatial frequencies, the error terms $R_{\sigma k}$ and $I_{\sigma k}$ were set to 0.019, the mean error of the visibilities reconstructed from closure results.

The resulting best-fit parameters are listed in Table 6.11 (see page 118), and the values of the χ^2 parameter, X(2), can be compared with those derived for a symmetrical distribution by referring to column X(2) of Table 6.5. There is some difficulty in interpreting the

nebula main body		2nd component		X(2)
flux ratio	width (r)	distance from phase centre(r)	width (r)	
0.920	1.280E-3	7.700E-4	6.800E-4	2.02
0.920	1.290E-3	7.700E-4	6.800E-4	2.52
0.940	1.300E-3	8.700E-4	6.800E-4	2.38
0.940	1.310E-3	8.700E-4	6.800E-4	2.00
0.940	1.320E-3	8.700E-4	6.800E-4	2.67
0.950	1.320E-3	8.700E-4	6.800E-4	2.08
0.950	1.330E-3	8.700E-4	6.800E-4	2.26
0.960	1.330E-3	9.700E-4	0.000	2.24
0.960	1.330E-3	9.700E-4	3.400E-4	2.00
0.960	1.330E-3	9.700E-4	6.800E-4	2.09
0.960	1.340E-3	9.700E-4	0.000	2.48
0.960	1.340E-3	9.700E-4	3.400E-4	2.02
0.960	1.340E-3	9.700E-4	6.800E-4	1.48
0.960	1.350E-3	9.700E-4	6.800E-4	1.94
0.970	1.340E-3	1.070E-3	0.000	2.66
0.970	1.350E-3	1.070E-3	0.000	1.55
0.970	1.350E-3	1.070E-3	3.400E-4	1.62
0.970	1.350E-3	1.070E-3	6.800E-4	2.22
0.970	1.360E-3	1.070E-3	0.000	1.52
0.970	1.360E-3	1.070E-3	3.400E-4	1.48
0.970	1.360E-3	1.070E-3	6.800E-4	1.78
0.970	1.360E-3	1.170E-3	0.000	2.60
0.970	1.360E-3	1.170E-3	3.400E-4	2.52
0.970	1.360E-3	1.170E-3	6.800E-4	2.71
0.970	1.370E-3	1.070E-3	0.000	2.57
0.970	1.370E-3	1.070E-3	3.400E-4	2.42
0.970	1.370E-3	1.170E-3	3.400E-4	2.61
0.970	1.370E-3	1.170E-3	6.800E-4	2.71

TABLE 6.11 : Results of the Gridded Data Model Fitting

results of Table 6.11. Some best-fit parameters which are solutions of previous mappings do not appear in Table 6.11, and others listed in this table do not appear in the previous solutions. However, the error terms, R_{σ_k} and I_{σ_k} , are only estimates of the actual errors and therefore can be best interpreted as a single weighting factor associated with the mapping. Hence, although it would appear from the small range of the χ^2 parameter, $X(1) - 1 < X(1) < 3$ - that all the points of Table 6.11 represent minima, a better interpretation is that only those points with $X(1)$ less than 2 represent actual solutions of equations (6.2 to 6.5).

It is important to note that since all visibility data have ultimately been derived from the closure results, the parameters of the distributions which best model the source structure have already been found by the results of the closure data least squares search, the solutions of which are listed on page 108 in Table 6.4. The significance of the present mapping of χ^2 based on the interpolated visibility function is that the results obtained from it can be used to give some indication of, firstly, the excellence of the form of the function chosen to model the source structure (two rectangular distributions) and, secondly, the accuracy of the interpolation used to derive the synthesized maps of the previous chapter.

If the best-fit brightness distribution obtained by closure model fitting (Model 1) and interpolated data model fitting (Model 2) is convolved to the same resolution as the

map displayed in Fig. 5.8, the three maps can be compared and any significant differences noted. From these differences a number of conclusions are possible:

- 1) Little deviation between the maps indicates that the form of the function, namely two rectangular distributions, is a reasonable representation of the source structure and that the interpolation is good.
- 2) Significant deviation between the maps indicates that both the models and the interpolation are inaccurate.
- 3) If the maps derived from the least squares searches are similar but differ from the original synthesized map significantly, the interpolation is good but the form of the function chosen to model the source structure needs to be refined.

The best fit models from the searches described in this section and Section 6.4 can be arbitrarily chosen from Table 6.11 ($X(1) < 2$) and Table 6.4 respectively. The two models which were convolved to the same resolution as the original maps are described by the parameters listed in Table 6.12 (see page 121).

The convolved distributions were obtained by initially evaluating the visibilities at a regular grid interval of 100λ , using option '2' of the 'table -a' program (see Appendix 4), and then Fourier transforming the output data weighted by the coefficients listed in Table 5.6. The two

Parameters	Model 1	Model 2
main body of nebula		
rel. flux density	0.96	0.97
width	$1.32 \times 10^{-3} r.$	$1.36 \times 10^{-3} r.$
2nd. component		
distance from phase centre	$9.70 \times 10^{-4} r.$	$1.07 \times 10^{-3} r.$
width	0	0

TABLE 6.12 : Parameters of Models 1 and 2

resultant maps are superimposed on the original synthesized map of the source distribution in Fig. 6.3. It can be seen that there is a small difference on the western edge of the remnant between all three distributions.

The fact that the two distributions derived from best-fit models coincide with each other to a higher degree than with the synthesized map of Chapter 5, tends to suggest that the rectangular form of the function chosen to model the source structure needs to be refined. This, of course, is hardly a surprising result, since it is rather unlikely that the main body of the nebula has an exactly rectangular distribution along the chosen axis.

On the other hand, since the deviation is fairly small, it can still be concluded that within the resolution limits of the present study, a rectangular distribution with a point or extended component is a reasonable model of the actual source structure, and that the visibility

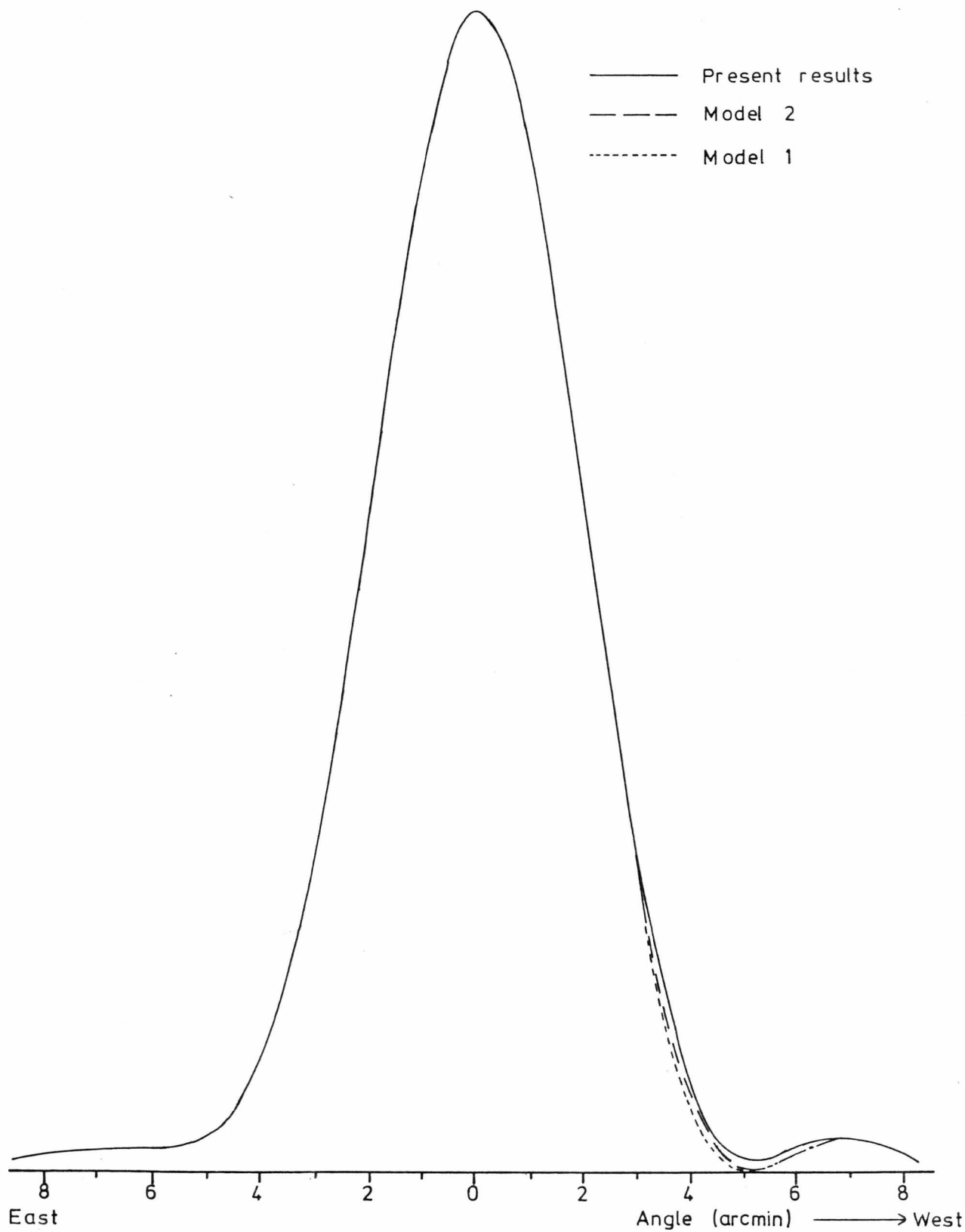


FIG. 6.3 Comparison Of Synthesized Distribution With Model Distributions Convolved To The Same Resolution

function can be interpolated without significant bias.

6.7 TEMPORAL LIMITATIONS OF THE PRESENT STUDY

The results presented in this study have assumed no secular variation of the supernova remnant over the time period in which the data have been obtained. Unfortunately, this assumption is not valid, and two effects have some bearing on the conclusions reached.

First of all, there is the expansion of the remnant itself. Dickel and Greisen (1979) have compared radio maps at 2695MHz, obtained at different epochs, and concluded that any net expansion of the radio shell is less than $3,000\text{kms}^{-1}$. At an assumed distance of 2.8kpc (Van der Bergh 1971) and for a period of 21 months over which the observations were made (see Table 3.4), the increase in width of Cassiopeia A is approximately 0.8 arcsec. for an assumed maximum expansion rate of $3,000\text{kms}^{-1}$. The effect of such an increase in width is negligible compared with the uncertainty in the width of the main body of the nebula, ± 6.3 arcsec., derived from the model fitting (see Table 6.4).

The effect of the low frequency anomaly, referred to in Section 1.1.3, is of much greater difficulty to ascertain. The last published value of the ratio $S_{\text{Cas}}/S_{\text{Cyg}}$ is 1.31 ± 0.05 at epoch 1977.2 (Read 1977ii). However, with the time-scale of the variability as short as 2 to 6 years, the ratio at the epoch of the present study was likely to have been

anywhere between 1.0 (the value derived by extrapolating the time variation of the ratio before any anomaly was noticed, to epoch 1980-81), and 1.6 (the maximum value reported by Erickson and Perley in 1975).

To obtain some estimate of the flux density ratio at the present epoch, measurements were made over consecutive days during March 1981 of the total power deflection for meridian transits of Cassiopeia A and Cygnus A. The peak deflections, when each source was directly overhead, was measured and the ratios calculated, resulting in a mean of 1.57 ± 0.08 . The effect of the variation of gain of the aerial at the two declinations was corrected for by multiplying the ratio by 0.97, since Cassiopeia A and Cygnus A transit the meridian approximately $+6^\circ$ and -12° from the zenith at the basestation. It must however, be strongly emphasized that the value obtained is only a rough estimate of the true ratio since neither gain variations with time nor differences in ionospheric absorption between the two source transits, were compensated for. The four most recently published flux density ratios of Cassiopeia A to Cygnus A at 38MHz are listed in Table 6.13 (see page 125), together with the value determined in the present study. Although the most recent value cannot be regarded in the same light as the others because of the measurement technique, it is reasonable to view it as an indication of a possible cosinusoidal secular variation of the flux density of Cassiopeia A at 38MHz. If this is the case, an estimate of the secular variation over the approximately linear part of the cosinusoid can be derived by comparing

Epoch	Flux ratio ($S_{\text{Cas}}/S_{\text{Cyg}}$)	Reference
1966.9	1.42 ± 0.05	Parker (1968)
1974.8	1.60 ± 0.07	Erickson and Perley (1975)
1975.9	1.48 ± 0.07	Read (1977i)
1977.2	1.31 ± 0.05	Read (1977ii)
1981.3	1.52 ± 0.08	Present study

TABLE 6.13 : Flux Density Ratio of Cassiopeia A to
Cygnus A at 38MHz

the flux ratios obtained over the years 1974 to 1977. Over a period of 1 year:

$$\Delta S_{\text{Cas}} = 0.12 S_{\text{Cyg}}$$

This gives rise to a total flux variation of approximately 14% of the nebula flux density at epoch 1981.3 over the time period over which the closure visibilities were obtained.

However, if the anomaly is associated with the main body of Cassiopeia A, or with the nebula as a whole, the ratio of the jet flux density to the main body flux density does not vary greatly over the time period in question. It is only in the case of an association between the jet and the anomaly, where the variation is of significance. Since the most significant results defining the asymmetry of the source were obtained at spacings of 600λ and 715λ , it is reasonable to further reduce the time period to 8 months,

in which case the total flux variation becomes approximately 5%.

A 5% variation is greater than the uncertainties in the jet flux density obtained as a result of the model fitting of the previous sections, and therefore, the flux density of the jet may be consistent with an upper limit of 10% of the total flux of the source rather than 4 to 6%.

Nevertheless, a cosinusoidal secular variation is but one of several interpretations and it is equally likely that the anomaly was either a symptom of the nebula reaching a new phase of activity (Read 1977i), or simply represents the change recorded between the flux density decreasing until 1968 and then increasing (Chevalier et. al. 1978) or even, the flux remaining constant over the last 20 years (Chevalier et. al. 1978). For all of the latter interpretations the results presented earlier in this chapter remain unmodified, since the change in flux density derived above is no longer an accurate description of the secular variation over the last few years.

CHAPTER 7

CONCLUSIONS

7.1 THE LOW FREQUENCY STRUCTURE OF CASSIOPEIA A

Up to the time of writing the resolution of the present study has not permitted an unambiguous determination of the parameters of the source of the Cassiopeia A asymmetry. However, it is still possible to discuss the general consequences of the source distributions presented as solutions of the least squares model fitting. The results of Chapter 6 are generally consistent with a symmetrical nebula of radius 135 ± 3 arcsec. with a jet of indeterminate width, containing between 4 to 6% of the total flux at a distance of 200 ± 20 arcsec. east of the source phase centre.

Rosenberg (1970 i and ii) has calculated from his maps at 2.7GHz and 5GHz, that most of the observed radio emission can be fitted by a shell of outer radius 130 ± 5 arcsec. Allowing for a net expansion rate of the radio shell of $3,000 \text{ km s}^{-1}$ (see Section 6.7), the outer radius at the epoch of the present observations becomes 135 ± 5 arcsec., in excellent agreement with the results of the present study.

It should also be noted that Rosenberg (1970i) proposed a second, double shell model to account for the

emission plateau spreading beyond the edge of the shell. His best fit corresponded to a thick shell of outer radius 150 ± 5 arcsec. and thickness 60 ± 10 arcsec. together with a thin shell of outer radius 110 ± 5 arcsec. and thickness 5 arcsec. Such a model corresponds reasonably well with the X-ray images of Cassiopeia A that show a bright ring at a radius of approximately 140 arcsec. (Fabian et. al. 1980). Without the use of a more complex 3-component, 7-parameter distribution to model the source structure, it is impossible to comment on the ability of a double shell model to fit the results at 38MHz.

It is of somewhat greater difficulty to comment on the asymmetrical component of Cassiopeia A, due to the uncertainty in its width. However, it is not surprising to find that such a component should exist in the light of studies at optical and X-ray frequencies. Although the present work has been an attempt to determine the structure of the nebula in one dimension, it seems reasonable to conclude that the asymmetrical component is related in position to the jet illustrated in the map of the distribution of the nebulosity in which [SII] is strong relative to [OIII] (as shown in Fig. 2 of Kamper and Van der Bergh (1976)), and to the X-ray jet of Fabian et. al. (1980).

The formation of the optical jet has been much commented on and is believed to have been caused by either an asymmetrical explosion or inhomogenities in the interstellar medium. In particular, Chevalier and Kirshner (1979) have suggested that it is possible that the jet may be the

outcome of a highly asymmetric core collapse that led to the explosion and Arnett (1975) considers that inhomogeneous ejection is a possibility if rotation or a Rayleigh-Taylor instability is important in the explosion. Of relevance to such an explosion is the likelihood of the remnant tending towards spherical symmetry (as observed for the main body of the Cassiopeia A nebula), once the accreted mass is greater than the ejected mass, if the external medium is uniform (Chevalier 1974). The deceleration of the radio shell (Bell 1977) would certainly suggest that the accreted mass is now larger than the ejected mass. On the other hand, the jet and the gap in the radio shell which aligns in position angle with the flare, can be interpreted as having been caused by a band of less dense interstellar medium (Minkowski 1968; Rosenberg 1970i). Jennison (1965) considers such a conclusion unlikely since the general expansion of the main body seems remarkably symmetrical, but with the possibility of the presupernova star having lost its envelope (Chevalier 1976), the homogeneity of the interstellar medium is much in doubt.

The absence of any significant asymmetry in higher frequency radio maps, however, is puzzling and requires the jet spectrum to be very steep, as suggested by Jennison (1965) commenting on his detection of a 10% flare at 127MHz (Jennison and Latham 1959). An estimate of the minimum spectral index, α , of the jet defined by

$$S(\nu) = k\nu^\alpha \quad (7.1)$$

can be obtained by equating a maximum 2% with the flux density of the jet at 151MHz, a result considered by Matheson (1974) to be just consistent with his readings. For a 5% jet at 38MHz, a spectrum with spectral index of at least -1.47 results. With a more reasonable figure of 1% for the percentage flux density of the flare at 151MHz, the jet spectral index increases to approximately -2.0. The spectral index of the main body of the nebula has been well established (e.g. Baars and Hartsuijker 1972; Baars et. al. 1977) and the value is close to the median value of -0.75 derived from the distribution of spectral indices for sources with non-thermal spectra (Pacholczyk 1970). In general, for supernova remnants the spectral index ranges from -0.1 to -0.8 (Hogg 1974) and hence it is clear that the jet spectrum is anomalously steep.

The good agreement between the present results and those of Hutton et. al. (1974) has already been commented on in Chapter 6. Their solutions imply a point source asymmetrical component which requires a very steep spectrum with spectral index of approximately -2.5, in general agreement with the likely spectral index referred to above. Hutton et. al. point out that the required steep spectrum is suggestive of a Crab-like pulsar. If the 'zero' width results of the model fitting are taken to represent the location of a possible collapsed core ejected in the supernova explosion, a simple calculation based on an explosion date of 1657AD and a distance of 2.8kpc to the remnant (see Chapter 1) results in a pulsar 'runaway' velocity of 7,000 to 9,000 kms^{-1} , assuming no deceleration. Studies of

observed pulsars have given rise to estimates of their proper motions of several hundreds of kilometres per second (Andersen et. al. 1975) and suggestions have been made that they may be as high as $1,000\text{kms}^{-1}$ (e.g. Prentice 1970). Both of these figures are considerably lower than the implied velocity of the low frequency jet, suggesting it most unlikely that it is associated with a neutron star.

However, space velocities of up to over $8,000\text{kms}^{-1}$, are observed for fast moving knots in the optical jet (Van der Bergh 1971) and naturally it is a reasonable possibility that the asymmetrical component is associated with one or more of these knots. The optical knots have sizes typically of the order of a few arcseconds (Minkowski 1968) which, in fact, is also similar in angular extent to the compact radio peaks at high frequencies in the radio shell (e.g. Bell et. al. 1975), although it should be made clear that there is no known correlation between the fast optical knots and the radio peaks (Dickel and Greisen 1979; Rosenberg 1970ii).

For small but intense sources, radiating by the synchrotron mechanism, self absorption may be of importance, and the formula connecting the maximum flux density $S(\nu_m)$ and the cut-off frequency, ν_m , associated with the maximum, with the angular size of the source, θ , is given by, e.g. equation (18.33) of Kaplan and Pikelner (1970). This equation can be written:

$$\theta \sim 81.2 [S(\nu_m) \nu_m^{-5/2} B^{1/2}]^{1/2} [1+z]^{1/4} \quad (7.2)$$

where θ is in arcsec., ν_m is in MHz, $S(\nu_m)$ is in flux units, B (the magnetic flux density) is in Gauss and z takes into account the effect of the red shift.

If the asymmetrical component is optically thick at $\nu_m = 38\text{MHz}$, such that the flux density below 38MHz behaves as:

$$S(\nu) = k_1 \nu^{5/2} \quad (7.3)$$

...from Pacholczyk (1970)

and above 38MHz behaves as:

$$S(\nu) = k_2 \nu^{-2.0}$$

where -2.0 is an estimate of the spectral index obtained above, then with a 5% jet of flux density approximately 1670f.u. and a magnetic field of $3 \times 10^{-4}\text{G}$ (Bychov 1974), the angular size of the emitting region must be of the order of 4.5 arcsec. Such a value seems acceptable for the proposed mechanism but does assume the same value of the magnetic field in the jet as in the shell of the nebula. Such an assumption implies that the processes leading to the amplification of the magnetic field, generally believed to be caused by compression by the supernova shock and by turbulence (e.g. Bell 1978; Cowsik and Sarkar 1980) must also apply to the new asymmetrical component.

The synchrotron radiation also requires a source of

relativistic electrons, the distribution of which can be assumed to follow the usual power law:

$$N(E) = N_0 E^{-\gamma} \quad (7.4)$$

where $N(E)$ is the number of electrons, E is the energy of an electron and γ is the energy spectral index.

The radio spectrum in the optically thin region is then represented by equation (7.1) where

$$\gamma = 1 - 2\alpha$$

The form of the equations, thus requires the energy spectral index for the jet to be twice as steep as for the nebula main body.

The possibility of a relationship between the asymmetrical component and the low frequency anomaly has been mentioned in Section 6.7. Read (1977 i and ii) has already illustrated the remarkably short period for the time-scale of the anomaly, stating that it may be compared with the ten year variability of the optical knots. Equating the mean speed of the fast optical knots with the rate governing changes in the source, Read further calculates that the variability implies a region of angular size 4.5 arcsec. Such a value coincides well with the earlier calculation of the size of the emitting region that may be connected with the low frequency asymmetry.

A number of mechanisms have been proposed to explain the variability, but those summarised in Section 1.1.3 do not rely on the source of the anomaly arising from a restricted region of the nebula. Read (1977ii) has, however, suggested that "a single compact feature may be responsible for the 38MHz radio flare", having calculated that a component of angular dimensions approximately 6 arcsec. could be contained by ram pressure and radiate with the required luminosity.

Most of the above conclusions tentatively support the 'point' source solutions of Chapter 6, which because of the limited resolution of the present study have by no means been established unambiguously. It is also difficult to reconcile the various results of previous low frequency studies (see Chapter 1) with some of the conclusions presented. However, there is no particular reason to accept that a single compact component is the source of the asymmetry.

If 'n' independent compact sources, each of size approximately 4 arcsec. and lifetime up to 10 years, positioned in the region of the optical jet, can be associated with the radiation, then a fairly random fluctuation of the flux may result, which at different epochs can explain a variety of results. If each knot is assumed optically thick at 38MHz then the magnetic field which is required has to be increased by n^2 over the assumed field for a single knot. Since a magnetic field of 2×10^{-3} G can be maintained in Cassiopeia A (Chevalier et. al.

1978), the association of several 'knots' with the low frequency jet remains a possibility.

Steep spectra are also associated with extragalactic radio sources approximately 10^9 to 10^{10} years old, the steep spectrum caused by synchrotron radiation losses (Slingo 1974). That the jet is such a source and hitherto has remained undetected because of its proximity to Cassiopeia A cannot be ruled out. However, the coincidence of the jet with the projection of the X-ray and optical flare onto the position angle of the present study, suggests such an interpretation is misleading. The absence of the low frequency jet in other studies, such as those of Slee and Wraith (1967) at 38MHz and Erickson et. al. (1972) at 121.6MHz seems to imply that the jet is related with the Cassiopeia A supernova remnant and perhaps with the flux anomaly associated with the nebula. Of course, both the studies referred to, would have resolved the source if the extended rather than point source solutions of Chapter 6 represent the general form of the true brightness distribution. In such a case the absence of fringes in the two studies is of no significance.

Finally, and for completeness, it should be noted that the association of a jet with a supernova remnant is not unique. Emerging from the supernova remnant G348.5+0.1 (CTB 37A) there is a jet with a similar spectrum to the rest of the remnant itself (Milne et. al. 1979). The similarity of the spectrum over the whole remnant leads Milne et. al. to favour the interpretation that their jet

is not an unrelated source but part of the supernova remnant. Clearly, the spectrum of the Cassiopeia A jet cannot be used as similar, favourable evidence of a direct, physical relation between the main body and the asymmetrical component.

7.2 FURTHER WORK IN PROGRESS

As has been implied in the conclusions above, the determination of the width of the eastern component has important astrophysical consequences, therefore the first priority of any further work is to increase the resolution of the observations, and determine the parameters of the asymmetry unambiguously. It is also of interest to measure the visibility function in several orientations and justify the claim that the asymmetrical component is coincident with the optical and X-ray jet.

Work is continuing to further these aims, and it is hoped to introduce an improved system in the near future based on a 4-station, digital, closure visibility interferometer developed by P.Avon. In particular, the implementation of the present system becomes difficult at long baselines because of the extremely long lengths of cable needed to produce the required delay times. In the new system the use of long lengths of cable is avoided by employing digital delays (P.Avon private communication).

APPENDICES

APPENDIX 1 - CIRCUIT DIAGRAMS

The following circuit diagrams, referred to in the main text, have been included for completeness.

1. The Basic Receiver System

- Fig. Al.1 R.F. amplifier and mixer.
Fig. Al.2 10.7MHz i.f. amplifier.
Fig. Al.3 27.3 MHz crystal oscillator.
Fig. Al.4 Emitter follower buffers.

2. The Correlator and Fringe Output System

- Fig. Al.5 Multiplier.
Fig. Al.6 Integrator and d.c. amplifier.

3. Additional Outstation Circuitry

- Fig. Al.7 Narrow band amplifier tuned to outstation oscillator frequency.
Fig. Al.8 Assembly filtering the radio link output into its constituent components.
Fig. Al.9 38MHz filter and mixer.

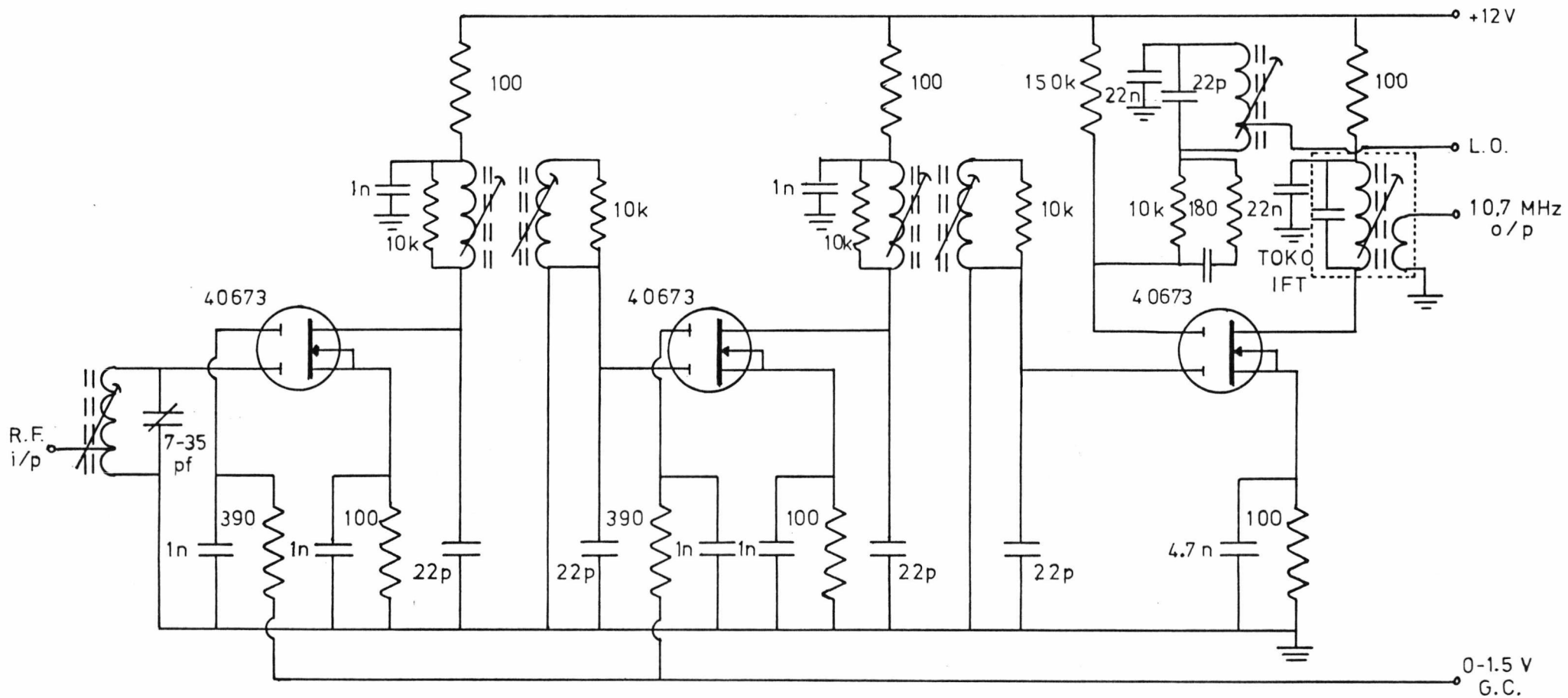


FIG. A1.1 R.F. Amplifier & Mixer

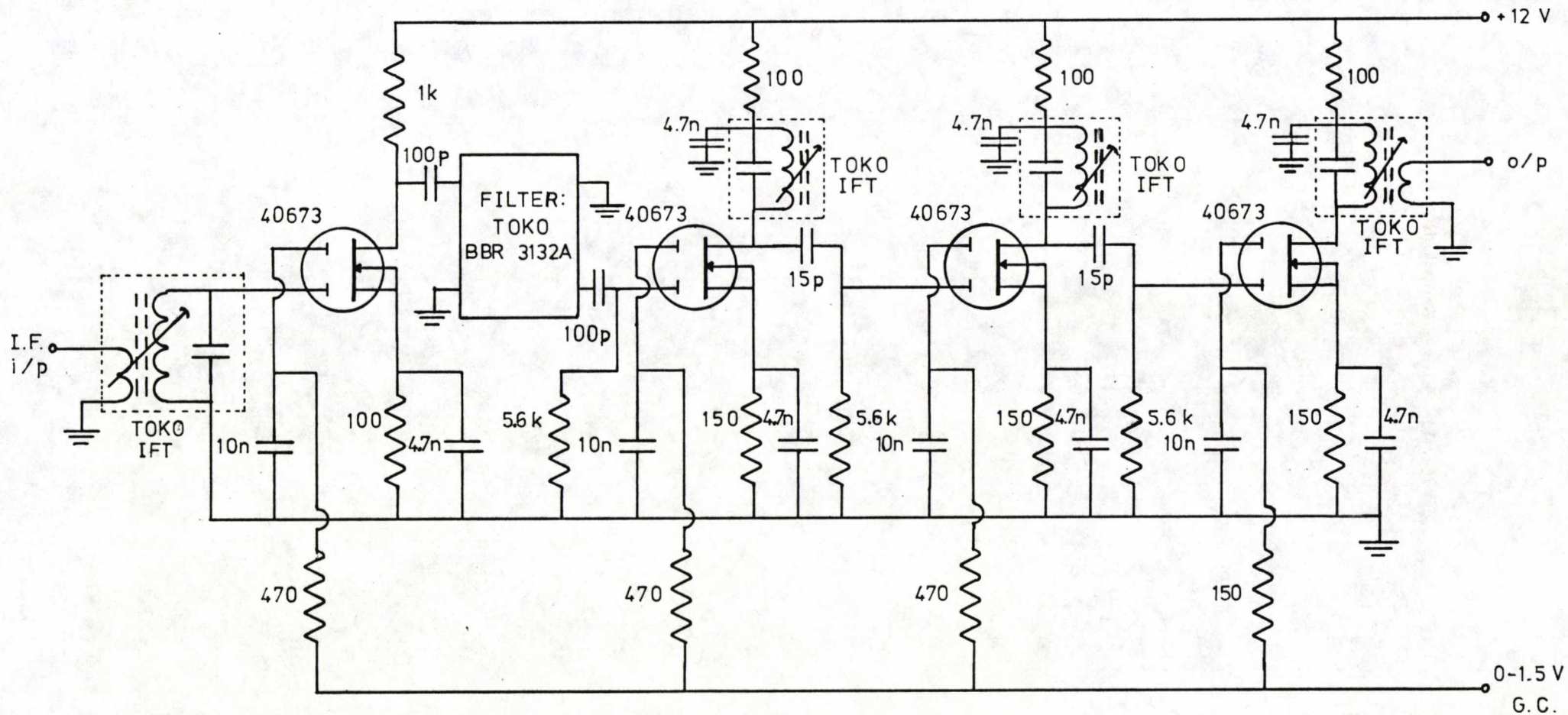


FIG. A1.2 I.F. Amplifier

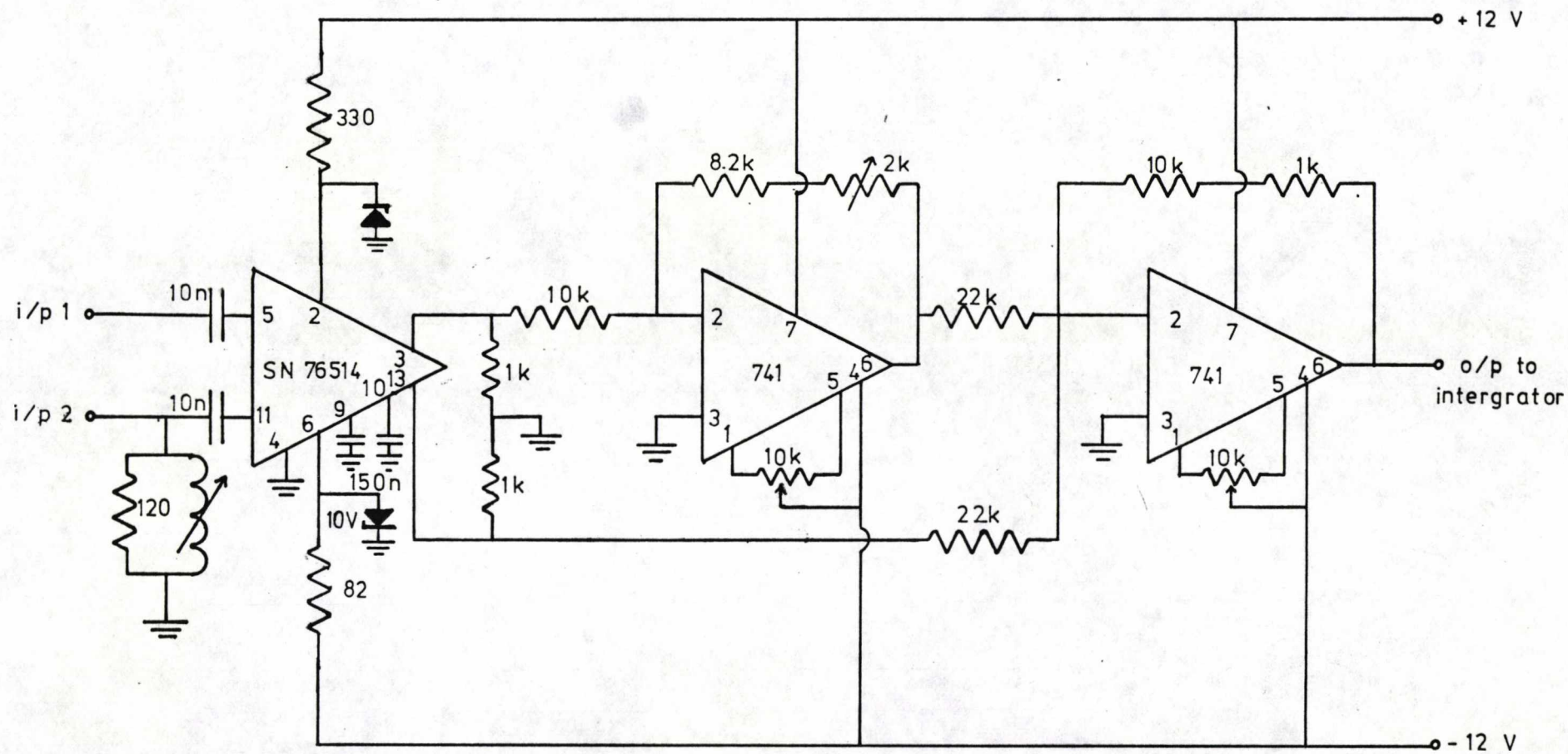


FIG. A1.5 The Multiplier

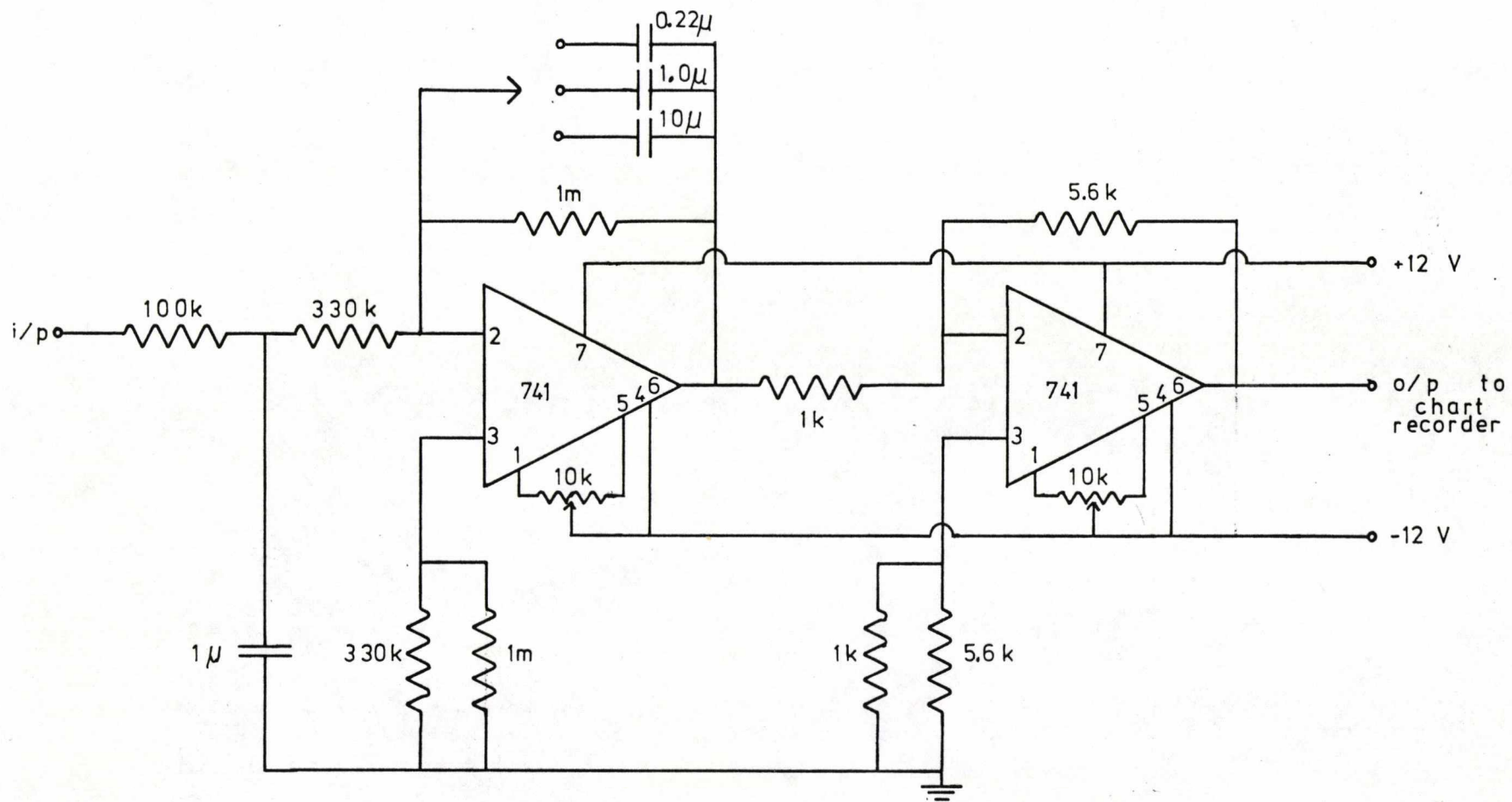


FIG. A1.6 Integrator & D.C. Amplifier

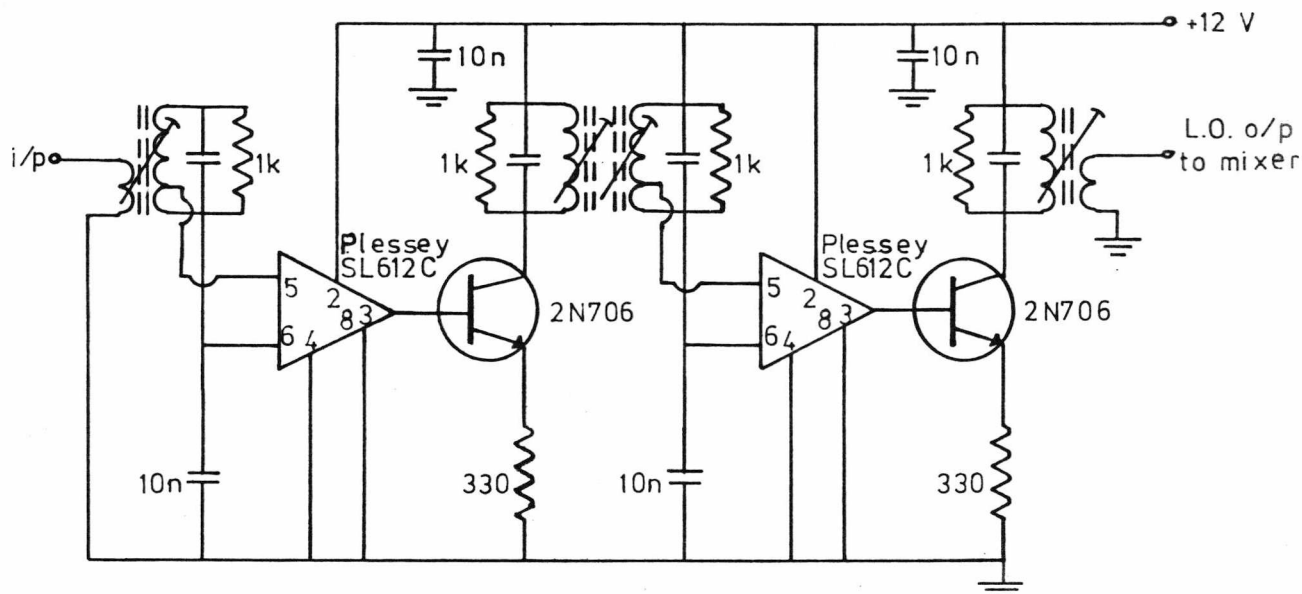


FIG. A1.7 Amplifier tuned to Outstation Oscillator Frequency

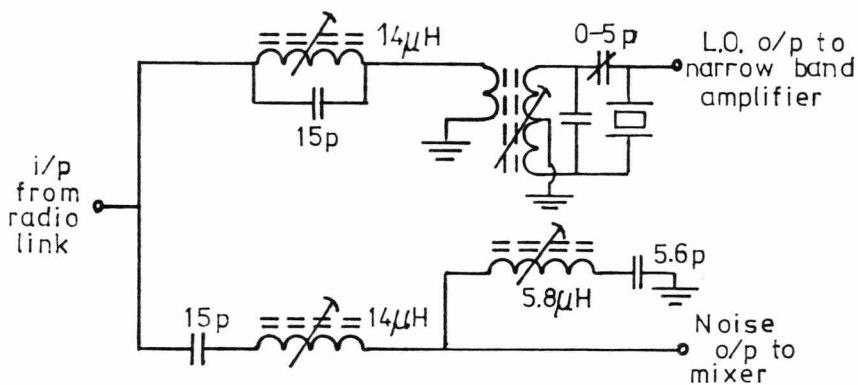


FIG. A1.8 Radio Link Output Filter

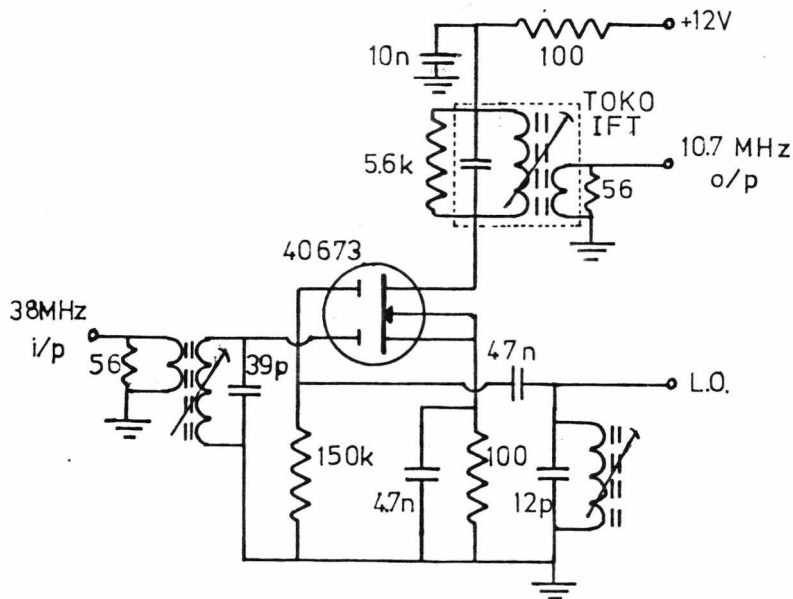


FIG. A1.9 38MHz Filter & Mixer

APPENDIX 2 - THEORY OF THE 2-STATION INTERFEROMETER

The following analysis is to a great extent based on that of Fomalont and Wright's in their chapter "Interferometry and Aperture Synthesis", in "Radio Astronomy and the Galactic System" (1974).

Fig. A2.1 charts the response at various stages of a 2-station interferometer system to incoming radiation. At each of the two stations 'i' and 'j', a signal due to the source is generated at slightly different times, the time difference, τ , given by:

$$\tau = (1/c) \underline{B} \cdot (\underline{s} + \underline{a})$$

where \underline{B} is the physical spacing of the interferometer, and \underline{s} is the position vector of the phase centre of the source, such that any other point is denoted by $\underline{s} + \underline{a}$.

Hence after passing through receivers 'i' and 'j', the voltages at the multiplier can be represented by:

$$V_1 = \sqrt{I(\underline{a})d\underline{a}} A_i \cos(2\pi\nu(t - \tau - \tau_i) + \psi_i)$$

and

$$V_2 = \sqrt{I(\underline{a})d\underline{a}} A_j \cos(2\pi\nu(t - \tau_j) + \psi_j)$$

where A_i and A_j are the gain factors of the i-th and j-th channels respectively, τ_i and τ_j represent the time delay

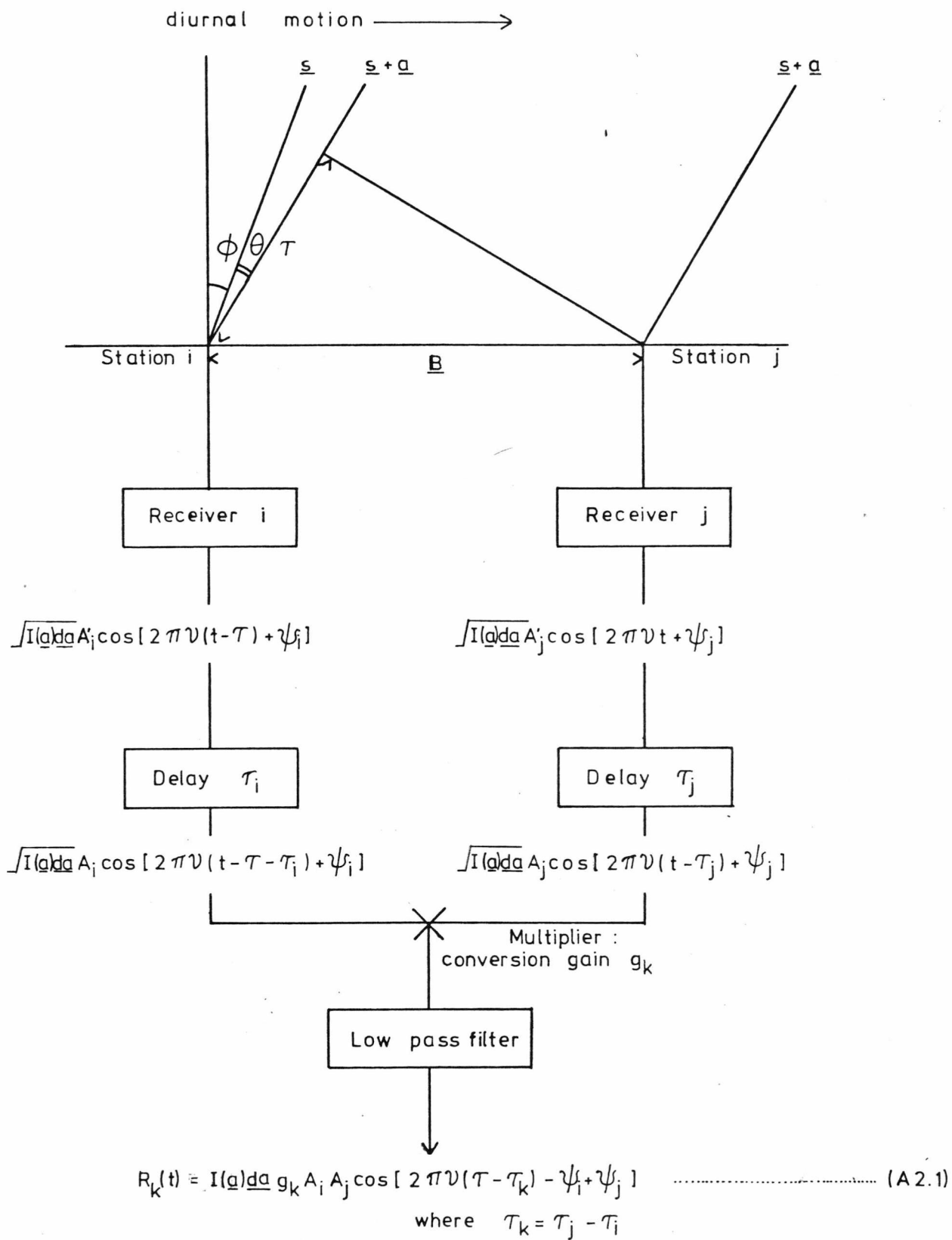


FIG. A2.1 Response Of A Two Station Interferometer

in each limb of the interferometer including any cable delays since the signal was received at each aerial, and ψ_i and ψ_j represent the phase errors in each channel due to the ionosphere and receiver systems.

The output of the interferometer can thus be represented by equation (A2.1). In this equation, the phase term can be expanded to first order if the source is assumed small:

$$\underline{B}(\underline{s} + \underline{a}) \quad \underline{B} \cdot \underline{s} + \underline{b} \cdot \underline{a}$$

where only the projected spacing, \underline{b} , is used in the second term, since \underline{a} is nearly perpendicular to \underline{s} . Hence, the interferometer output can be written:

$$R_k(t) = g_k A_i A_j \exp i \left[2\pi \nu \left(\frac{\underline{B} \cdot \underline{s}}{c} - \tau_k \right) - \psi_i + \psi_j \right] \int_{-\infty}^{\infty} I(\underline{a}) \exp i \left[2\pi \nu \frac{\underline{b} \cdot \underline{a}}{c} \right] \underline{d}\underline{a} \quad (\text{A2.2})$$

where the real part of equation (A2.2) is implied.

Since the complex visibility function, V , can be written:

$$V = \int_{-\infty}^{\infty} I(\underline{a}) \exp i \left[2\pi \frac{\underline{b} \cdot \underline{a}}{\lambda} \right] \underline{d}\underline{a} \quad (\text{A2.3})$$

where V can be written in terms of its amplitude and phase, $V = |F(n)| \exp(i \Psi(n))$, the interferometer output becomes:

$$R_k(t) = g_k A_i A_j V \exp i \left[2\pi \nu \left(\frac{\underline{B} \cdot \underline{s}}{c} - \tau_k \right) - \psi_i + \psi_j \right] \quad (\text{A2.4})$$

Using the equatorial system of co-ordinates, the vectors

\underline{B} and \underline{s} can be rewritten in terms of a baseline B of declination D and hour angle H , and a source of declination δ and hour angle h :

$$\underline{B} = \begin{pmatrix} B \cos D \cos H \\ B \cos D \sin H \\ B \sin D \end{pmatrix} \quad \underline{s} = \begin{pmatrix} \cos \delta \cos h \\ \cos \delta \sin h \\ \sin \delta \end{pmatrix}$$

where a unit vector:

\underline{e}_x points towards the point $\delta = 0^\circ$, $h = 0\text{hr.}$;

\underline{e}_y points towards the point $\delta = 0^\circ$, $h = 6\text{hr.}$ and

\underline{e}_z points towards the point $\delta = 90^\circ$.

For an east-west baseline $D = 0^\circ$ and $H = 6\text{hr.}$, and therefore the interferometer output can be written:

$$R_k(t) = g_k A_i A_j \exp i [2\pi \frac{B}{\lambda} (\cos \delta \sin h) - 2\pi \nu \tau_k - \psi_i + \psi_j] \int_{-\infty}^{\infty} I(\theta) \exp i [2\pi \frac{B}{\lambda} \theta] d\theta \quad (\text{A2.5})$$

where θ is the angle from the phase centre to another point on the source.

For an ideal interferometer, with no phase errors and normalised gain, $R(t)$ becomes the usual interferometer equation:

$$R(t) = \exp i [2\pi \frac{B}{\lambda} \sin \phi] \int_{-\infty}^{\infty} I(\theta) \exp i [2\pi \frac{B}{\lambda} \theta] d\theta \quad (\text{A2.6})$$

where ϕ (see Fig. A2.1) is the angle between the vertical and the source phase centre, itself given by:

$$\sin \phi = (\underline{B} \cdot \underline{s}) / B$$

APPENDIX 3 - FOURIER TRANSFORM PROGRAM

```

1.  # include "transform.h"
2.
3.  main ()    /* Discrete Fourier Transform Of Sampled Visibility Data */
4.  {
5.      double sin(), cos();
6.      double p,x,y,z,co,si,angle,second;
7.      char data();
8.      double arr [NOP][2];
9.      double out [OUT][2];
10.     double nt, base, nop;
11.     int i,a,b,o;
12.
13.     p = 3.14159;
14.     nt = INT;
15.     base = BASE;
16.     nop = NOP;
17.     second = (180 / nt) * (3600 / base) / nop / p;
18.     o = INT * NOP;
19.
20.     for (b = 0; b < NOP ; b++)
21.         scanf ("%f %f",&arr[b][0],&arr[b][1]);
22.     for ( b = 0; b < NOP; b++)
23.         printf ("%3d:  R%6.3f  I%6.3f\n", b, arr [b][0], arr [b][1]);
24.     printf (2,"Data successfully read in\n");
25.     arr[0][0] = arr[0][0] / 2 ;
26.     arr[0][1] = arr[0][1] / 2 ;
27.     for (a = 0; a <= o / 2; a++) {
28.         x = 0;
29.         y = 0;
30.         for (i = 0; i < NOP; i++){
31.             angle = 2 * p * i * a / (INT * NOP);

```

```

32.         co = cos(angle);
33.         si = sin(angle);
34.         x += arr [i][0] * co + arr [i][1] * si;
35.         y += arr [i][0] * co - arr [i][1] * si;
36.     }
37.     if (a == 0)
38.         z = x;
39.     out[a][0] = x / z;
40.     out[a][1] = y / z;           /* Phase centre normalisation */
41. }
42. printf (2,"Transform successfully completed\n");
43. printf ("\n\n\tRESULTS\n");
44. printf ("\t~~~~~\n\n");
45. printf (" Incremental Angle : %6.3f secs. of arc\n\n",second);
46. for (a = 0; a <= o / 2; a++)
47.     printf ("%3.0d %6.3f\t-%2.0d %6.3f\n",a,out[a][0],a,out[a][1]);
48. cflush (1);
49. printf (2,"Results ready\n");
50. }
51.
52. /*
53. transform.h:
54.
55. #define LIM      10
56. #define NOP      8      /* NOP : no. i/p data points
57. #define INT      8      /* INT * NOP : no. o/p data points
58. #define BASE    100    /* BASE: i/p data sampling interval in wavelengths
59. #define OUT     32    /* OUT : INT * NOP / 2
60.
*/

```

APPENDIX 4 - THE MODEL FITTING PROGRAM

1. /*

2.

3. NAME

4. table - tabulate least squares values

5.

6. SYNOPSIS

7. table [-a] [-f option no. filename] [-s] ...

8.

9. DESCRIPTION

10. Table is a program which performs model fitting least squares tests,
11. based on three sets of data:

12.

13. 1) der[i][j] : The complex visibility results for baseline space
14. gridded every 100 wavelengths; derived from a graph of inp[i][j].

15.

16. 2) inp[i][j] : The complex visibility function reconstructed
17. from the closure results.

18.

19. 3) res[i][j] : The closure amplitude and closure phase results
20. calculated from the actual runs of the source transiting.

21.

22. COMMAND LINE OPTIONS

23. -a Prints out to the standard error o/p the available options
24. and requests one from the standard input.

25. Depending on the option number chosen the output tabulates
26. either the results and the complex visibility function
27. derived for one set of model parameters, or the least squares
28. for small increments in the original model parameters.

29.

30. -f Input from a file. Output, depending on the second argument,
31. is a comparison of the results with the complex visibility

32. function derived for various model parameters.

33. Must be followed by two arguments :

34. 1) the required option number (1-8).

35. 2) the filename from which the model parameters
36. are read.

37.

38. -s Search program - gives least squares values for all the
39. permutations of the model parameters.

40. Can be followed by a second argument:

41. 1 : Model() search only

42. 2 : Trial() search only

43. 3 : Close() search only

44.

45. Can be used with the input from a file. The latter must
46. then have the following form:

47.

48. line 1) Normalised Cas. flux

49. MIN: ___??___ MAX: ___??___ INCR: ___??___

50. line 2) Cas. width

51. MIN: ___??___ MAX: ___??___ INCR: ___??___

52. line 3) Distance to extra source

53. MIN: ___??___ MAX: ___??___ INCR: ___??___

54. line 4) Width extra source

55. MIN: ___??___ MAX: ___??___ INCR: ___??___

56. line 5) Max. limit of Chi**2 for printing

57. TEST: ___??___ SQU: ___??___ LEAST: ___??___

58.

59. INTERNAL OPTIONS

60. 0 : Search program . For an input of source model parameters and
61. increments, outputs the parameters and the corresponding least
62. squares values. Not as exhaustive as the -s option above.

63.
 64. 1-8 : For a single set of source model parameters, 1-8 chooses
 65. which of the corresponding complex visibilities are printed
 66. for the three sets of data. The least squares value for each
 67. set of data is printed in all cases.

68.	1	Real results only
69.	2	Derived results only
70.	3	Closure results only
71.	4	Real and derived results
72.	5	Real and closure results
73.	6	Derived and closure results
74.	7	Real, derived and closure results
75.	8	Least squares o.p. only

76.
 77. -1 : The program aborts.

78.
 79.
 80. */
 81.
 82. main (argc,argv)
 83. int argc;
 84. char *argv[];
 85. {
 86. double model();
 87. double trial();
 88. double close();
 89. double r,w,y,e,test,square,least;
 90. double rt,rit,wt,wit,yt,yit,et,eit;
 91. int atoi();
 92. int fp,nl,c,i,dim,q,flag,z;
 93.

```
94.         input();
95.
96.         if (argc != 2 && argc != 3 && argc != 4){
97.             printf(2,"Usage: table [-a] [-f option no. filename]");
98.             printf(2," [-s] ...\n");
99.             exit(1);
100.        }
101.        if (argv[1][0] == '-' && argv[1][1] == 'a'){
102.            if (argc != 2){
103.                printf (2,"table -a: too many arguments\n");
104.                exit(1);
105.            }
106.            flag = 0;
107.        }
108.        else if (argv[1][0] == '-' && argv[1][1] == 'f')
109.            flag = 1;
110.        else if (argv[1][0] == '-' && argv[1][1] == 's'){
111.            z = 0;
112.            if (argc != 2 && argc != 3){
113.                printf (2,"Usage: table -s [option no.] ...\n");
114.                exit(1);
115.            }
116.            if (argc = 3)
117.                z = atoi(argv[2]);
118.            search(z);
119.            exit(0);
120.        }
121.        else{
122.            printf (2,"This option does not exist\n");
123.            exit(1);
124.        }
```

```
125.
126.     if (flag == 0){
127.         printf (2,"Choose option 0 - 8\n\n");
128.         printf (2,"For search program type\t\t'0'\n");
129.         printf (2,"Real results only type\t\t'1'\n");
130.         printf (2,"Derived results only type\t\t'2'\n");
131.         printf (2,"Closure results only type\t\t'3'\n");
132.         printf (2,"Real and derived type \t\t'4'\n");
133.         printf (2,"Real and closure type\t\t'5'\n");
134.         printf (2,"Derived and closure type\t\t'6'\n");
135.         printf (2,"Real,derived and closure type\t\t'7'\n");
136.         printf (2,"Least squares o.p. only type\t\t'8'\n");
137.         printf (2,"TO ABORT type\t\t\t'-1'\n\n");
138.         printf (2,"Enter preferred program please\t");
139.         scanf ("%d",&q);
140.         printf (2,"\n");
141.     }
142.
143.     if (flag == 1){
144.         if (argc != 4){
145.             printf (2,"Usage: table -f option no. ");
146.             printf (2,"filename ...\n");
147.             exit(1);
148.         }
149.         q = atoi( argv[2]);
150.         if (q <= 0 || q > 8){
151.             printf (2,"table: program aborted\n");
152.             exit(1);
153.         }
154.     }
155.     if (flag == 0){
```

```
156.         if (q < 0 || q > 8){
157.             printf (2,"table: program aborted\n");
158.             exit(1);
159.         }
160.     }
161.
162.     if (q != 0 && flag == 0){
163.
164.         printf (2,"Normalised Cas. flux please\t");
165.         scanf ("%f",&r);
166.         printf (2,"Cas. width please\t\t");
167.         scanf ("%f",&w);
168.         printf (2,"Distance to extra source please\t");
169.         scanf ("%f",&y);
170.         printf (2,"Width extra source please\t");
171.         scanf ("%f",&e);
172.         printf (2,"\n");
173.
174.             /* least squares values based on */
175.         test = model (r,w,y,e,q); /* test : real results */
176.         square = trial (r,w,y,e,q); /* square: derived graph results */
177.         least = close (r,w,y,e,q); /* least : closure results */
178.
179.         printf("\n%6.3f\t%6.3e %6.3e %6.3e\t: %6.2f %6.2f %6.2f\n"
180.             ,r,w,y,e,test,square,least);
181.         fflush(1);
182.     }
183.
184.
185.     else if (q != 0 && flag == 1){
186.         if ((fp = fopen(argv[3], 'r')) == -1){
```

```
187.         printf(2,"table: can't open %s\n",argv[3]);
188.         exit(1);
189.     }
190.     while ((c = cgetc(fp) ) != 0)
191.         if (c == '\n')
192.             ++nl;
193.     rew (fp);
194.
195.     for (i = 0 ; i < nl ; i++){
196.         scanf (fp,"%f %f %f %f", &r,&w,&y,&e);
197.         if (q == 1 || q == 4 || q == 5 || q == 7 || q == 8)
198.             test = model (r,w,y,e,q);
199.         if (q == 2 || q == 4 || q == 6 || q == 7 || q == 8)
200.             square = trial (r,w,y,e,q);
201.         if (q == 3 || q == 5 || q == 6 || q == 7 || q == 8)
202.             least = close (r,w,y,e,q);
203.         printf("\n%6.3f\t%6.3e %6.3e %6.3e\t:",r,w,y,e);
204.         printf(" %6.2f %6.2f %6.2f\n\n\n",test,square,least);
205.     }
206.     fflush(1);
207. }
208.
209. else {
210.
211.     printf (2,"Normalised Cas. flux please\t\t");
212.     scanf ("%f",&rt);
213.     printf (2,"Cas. flux increment please\t\t");
214.     scanf ("%f",&rit);
215.     printf (2,"Cas. width please\t\t\t");
216.     scanf ("%f",&wt);
217.     printf (2,"Cas. width increment please\t\t");
```

```
218.      scanf ("%f",&wit);
219.      printf (2,"Distance to extra source please\t\t");
220.      scanf ("%f",&yt);
221.      printf (2,"Dist. extra source incr. please\t\t");
222.      scanf ("%f",&yit);
223.      printf (2,"Width extra source please\t\t");
224.      scanf ("%f",&et);
225.      printf (2,"Width ext. source incr. please\t\t");
226.      scanf ("%f",&eit);
227.      printf (2,"No. of incrs. per dimension please\t");
228.      scanf ("%d",&dim);
229.
230.
231.      for (r = rt - rit * dim; r <= rt + rit * dim; r = r + rit){
232.          w = wt ;
233.          y = yt ;
234.          e = et ;
235.          test = model (r,w,y,e,q);
236.          square = trial (r,w,y,e,q);
237.          least = close (r,w,y,e,q);
238.          printf ("%6.3f\t%6.3e %6.3e %6.3e\t: ",r,w,y,e);
239.          printf ("%6.2f %6.2f %6.2f\n",test,square,least);
240.      }
241.
242.      for (w = wt - wit * dim; w <= wt + wit * dim; w = w + wit){
243.          r = rt;
244.          y = yt;
245.          e = et;
246.          test = model (r,w,y,e,q);
247.          square = trial (r,w,y,e,q);
248.          least = close (r,w,y,e,q);
```

```
249.         printf ("%6.3f\t%6.3e %6.3e %6.3e\t: ",r,w,y,e);
250.         printf ("%6.2f %6.2f %6.2f\n",test,square,least);
251.     }
252.
253.     for (y = yt - yit * dim; y <= yt + yit * dim; y = y + yit){
254.         r = rt;
255.         w = wt;
256.         e = et;
257.         test = model (r,w,y,e,q);
258.         square = trial (r,w,y,e,q);
259.         least = close (r,w,y,e,q);
260.         printf ("%6.3f\t%6.3e %6.3e %6.3e\t: ",r,w,y,e);
261.         printf ("%6.2f %6.2f %6.2f\n",test,square,least);
262.     }
263.
264.     for (e = et - eit * dim; e <= et + eit * dim; e = e + eit){
265.         r = rt;
266.         w = wt;
267.         y = yt;
268.         test = model (r,w,y,e,q);
269.         square = trial (r,w,y,e,q);
270.         least = close (r,w,y,e,q);
271.         printf ("%6.3f\t%6.3e %6.3e %6.3e\t: ",r,w,y,e);
272.         printf ("%6.2f %6.2f %6.2f\n",test,square,least);
273.     }
274.     fflush(1);
275. }
276. }
277.
278.
279. search(z)
```

```
280.   int z;
281.   {
282.       double model();
283.       double trial();
284.       double close();
285.       double r,w,y,e,test,square,least;
286.       double rnt,wnt,ynt,ent,rxt,wxt,yxt,ext,rit,wit,yit,eit;
287.       double q[3];
288.
289.       test = square = least = 0;
290.       q[0] = q[1] = q[2] = 0;
291.
292.       printf (2,"1\\ \tNormalised Cas. flux please\n");
293.       printf (2," \tMIN:\t\t");
294.       scanf ("%f",&rnt);
295.       printf (2," \tMAX:\t\t");
296.       scanf ("%f",&rxt);
297.       printf (2," \tINCR:\t\t");
298.       scanf ("%f",&rit);
299.       if (rit == 0){
300.           printf (2,"table: program aborted\n");
301.           return;
302.       }
303.       printf (2," \n2\\ \tCas. width please\n");
304.       printf (2," \tMIN:\t\t");
305.       scanf ("%f",&wnt);
306.       printf (2," \tMAX:\t\t");
307.       scanf ("%f",&wxt);
308.       printf (2," \tINCR:\t\t");
309.       scanf ("%f",&wit);
310.       if (wit == 0){
```

```
311.         printf (2,"table: program aborted\n");
312.         return;
313.     }
314.     printf (2,"\n3)\tDistance to extra source please\n");
315.     printf (2,"\tMIN:\t\t");
316.     scanf ("%f",&ynt);
317.     printf (2,"\tMAX:\t\t");
318.     scanf ("%f",&yxt);
319.     printf (2,"\tINCR:\t\t");
320.     scanf ("%f",&yit);
321.         if (yit == 0){
322.             printf (2,"table: program aborted\n");
323.             return;
324.         }
325.     printf (2,"\n4)\tWidth extra source please\n");
326.     printf (2,"\tMIN:\t\t");
327.     scanf ("%f",&ent);
328.     printf (2,"\tMAX:\t\t");
329.     scanf ("%f",&ext);
330.     printf (2,"\tINCR:\t\t");
331.     scanf ("%f",&eit);
332.         if (eit == 0){
333.             printf (2,"table: program aborted\n");
334.             return;
335.         }
336.     printf (2,"\nPlease enter Chi-square limits\n");
337.     if (z == 1 || z == 0){
338.         printf (2,"\tTEST:\t\t");
339.         scanf ("%f",&q[0]);
340.     }
341.     if (z == 2 || z == 0){
```

```

342.         printf (2, "\tSQUARE:\t\t");
343.         scanf ("%f",&q[1]);
344.     }
345.     if (z == 3 || z == 0){
346.         printf (2, "\tLEAST:\t\t");
347.         scanf ("%f",&q[2]);
348.     }
349.
350.
351.     for (r = mt; r <= rxt ; r = r + rit){
352.         for (w = wnt; w <= wxt; w = w + wit){
353.             for (y = ynt; y <= yxt; y = y + yit){
354.                 for (e = ent; e <= ext; e = e + eit){
355.                     if (z == 1)
356.                         test = model(r,w,y,e);
357.                     else if (z == 2)
358.                         square = trial(r,w,y,e);
359.                     else if (z == 3)
360.                         least = close(r,w,y,e);
361.                     else {
362.                         test = model (r,w,y,e);
363.                         square = trial (r,w,y,e);
364.                         least = close (r,w,y,e);
365.                     }
366.                     if (test < q[0] || square < q[1] || least < q[2]){
367.                         printf ("%6.3f\t%6.3e %6.3e %6.3e\t: ",r,w,y,e);
368.                         printf ("%6.2f %6.2f %6.2f\n",test,square,least);
369.                     }
370.                 }
371.             }
372.         }

```

```

373.         }
374.         cflush(1);
375.     }
376.
377.
378.
379.     double model (r,w,y,e,q)           /* least squares values based */
380.     double r,w,y,e;                   /* on 'real' data - the      */
381.     int q;                             /* visibility fn. reproduced */
382.                                         /* from closure results     */
383.
384.     {
385.         double sin(), cos(), sqrt(), atan();
386.         double arr[8][2];
387.         double ang[8][2];
388.         extern double inp[ 8 ][5];
389.         int i;
390.         double p,a,b,c,g,l,m,n,h;
391.
392.         p = 3.14159;
393.         m = 0;
394.
395.
396.         b = 2 * p * y * (1 - r) / r ;
397.         c = 2 * p * y ;
398.
399.         for (i = 0 ; i < 8 ; i++){
400.             h = inp[i][4];
401.             a = p * h * w ;
402.             if (a == 0)
403.                 a = r ;

```

```

404.         else
405.             a = (sin(a) / a) * r ;
406.         g = p * h * e ;
407.         if (g == 0)
408.             g = 1 - r ;
409.         else
410.             g = (sin(g) / g) * (1 - r) ;
411.         arr[i][0] = a * cos(b * h) + g * cos(c * h) ;
412.         arr[i][1] = a * sin(b * h) - g * sin(c * h) ;
413.         n = (inp[i][0] - arr[i][0]) / inp[i][2];
414.         l = (inp[i][1] - arr[i][1]) / inp[i][3];
415.         n = n * n;
416.         l = l * l;
417.         m = m + n + l;
418.     }
419.
420.     if (q == 1 || q == 4 || q == 5 || q == 7){
421.         printf ("Base\t\tReal\t\t\tImag\t\t\t Model");
422.         printf ("\nline\t\t actual model\t\t actual ");
423.         printf ("model\t\t amp\t\t phase\n\n");
424.         for (i = 0; i < 8; i++){
425.             ang[i][0] = sqrt(arr[i][0]*arr[i][0] + arr[i][1]*arr[i][1]);
426.             ang[i][1] = atan(arr[i][1] / arr[i][0]) * (180 / p);
427.             printf ("%4.1f :\tR %6.3f %6.3f\tI %6.3f %6.3f\t",
428.                 inp[i][4],inp[i][0],arr[i][0],inp[i][1],arr[i][1]);
429.             printf ("%6.3f\t%6.2f\n",ang[i][0],ang[i][1]);
430.         }
431.     }
432.     return (m);
433. }
434.

```

```

435.
436. double trial (r,w,y,e,q)          /* least squares values based */
437. double r,w,y,e;                  /* on the derived data - */
438. int q;                            /* the visibility function at a */
439.                                  /* regular grid interval inter- */
440.                                  /* polated from graphs */
441.
442. {
443.     double sin(), cos(), sqrt(), atan();
444.     double arr[8][2];
445.     double ang[8][2];
446.     extern double der[ 8 ][2];
447.     int i;
448.     double p,a,b,c,g,l,m,n;
449.
450.     p = 3.14159;
451.     m = 0;
452.
453.
454.     b = 2 * p * 100 * y * (1 - r) / r ;
455.     c = 2 * p * 100 * y ;
456.
457.     for (i = 0 ; i < 8 ; i++){
458.         a = i * p * 100 * w ;
459.         if (a == 0)
460.             a = r ;
461.         else
462.             a = (sin(a) / a) * r ;
463.         g = i * p * 100 * e ;
464.         if (g == 0)
465.             g = 1 - r ;

```



```
497. double r,w,y,e; /* on closure data */
498. int q;
499.
500. {
501.     double sin(), cos(), sqrt(), atan();
502.     double arr[13][2];
503.     double fin[9][2];
504.     double del[9][2];
505.     double ang[13][2];
506.     extern double res[13][5];
507.     int base[9][1];
508.     int i;
509.     double p,a,b,c,g,l,m,n,h;
510.
511.     base[0][0] = 44;
512.     base[1][0] = 104;
513.     base[2][0] = 172;
514.     base[3][0] = 143;
515.     base[4][0] = 247;
516.     base[5][0] = 247;
517.     base[6][0] = 352;
518.     base[7][0] = 600;
519.     base[8][0] = 715;
520.
521.     p = 3.14159;
522.     m = 0;
523.
524.
525.     b = 2 * p * y * (1 - r) / r ;
526.     c = 2 * p * y ;
527.
```

```

528.     for (i = 0 ; i < 13 ; i++){
529.         h = res[i][4];
530.         a = p * h * w ;
531.         if (a == 0)
532.             a = r ;
533.         else
534.             a = (sin(a) / a) * r ;
535.         g = p * h * e ;
536.         if (g == 0)
537.             g = 1 - r ;
538.         else
539.             g = (sin(g) / g) * (1 - r) ;
540.         arr[i][0] = a * cos(b * h) + g * cos(c * h) ;
541.         arr[i][1] = a * sin(b * h) - g * sin(c * h) ;
542.         ang[i][0] = sqrt(arr[i][0]*arr[i][0] + arr[i][1]*arr[i][1]);
543.         ang[i][1] = atan(arr[i][1] / arr[i][0]) * (180 / p);
544.     }
545.
546.     fin[0][0] = ang[8][0];
547.     fin[1][0] = ang[1][0] * ang[8][0] / ang[9][0];
548.     fin[2][0] = ang[3][0] / ( ang[10][0] * ang[1][0] );
549.     fin[3][0] = ang[2][0] * ang[10][0] / ang[11][0];
550.     fin[4][0] = ang[4][0] / ( ang[1][0] * ang[2][0] );
551.     fin[5][0] = ang[4][0] * ang[2][0] / ang[1][0];
552.     fin[6][0] = ang[5][0] / (ang[1][0] * ang[4][0] );
553.     fin[7][0] = ang[6][0] * ang[4][0] / ang[5][0];
554.     fin[8][0] = ang[7][0] * ang[6][0] / ang[12][0];
555.     fin[0][1] = ang[8][1];
556.     fin[1][1] = ang[1][1] - ang[8][1] - ang[9][1];
557.     fin[2][1] = ang[3][1] - ang[10][1] - ang[1][1];
558.     fin[3][1] = ang[2][1] - ang[10][1] - ang[11][1];

```

```

559.     fin[4][1] = ang[4][1] - ang[1][1] - ang[2][1];
560.     fin[5][1] = ang[4][1] - ang[2][1] - ang[1][1];
561.     fin[6][1] = ang[5][1] - ang[1][1] - ang[4][1];
562.     fin[7][1] = ang[6][1] - ang[4][1] - ang[5][1];
563.     fin[8][1] = ang[7][1] - ang[6][1] - ang[12][1];
564.
565.     if (q == 3 || q == 5 || q == 6 || q == 7){
566.         printf ("\nBase\t Least Squares\t\t\tReal");
567.         printf ("\t\t\tImag\nline\t\t\t\t actual");
568.         printf (" model\t actual model\n\n");
569.     }
570.     for (i = 0; i < 9; i++){
571.         del[i][0] = fin[i][0] * cos(fin[i][1] * p / 180);
572.         del[i][1] = fin[i][0] * sin(fin[i][1] * p / 180);
573.         n = (res[i][0] - del[i][0]) / res[i][2];
574.         l = (res[i][1] - del[i][1]) / res[i][3];
575.         n = n * n;
576.         l = l * l;
577.         m = m + n + l;
578.         if (q == 3 || q == 5 || q == 6 || q == 7){
579.             printf ("%3.0d : R %6.3f\tI %6.3f\t",base[i][0],n,l);
580.             printf ("R %6.3f %6.3f\tI %6.3f %6.3f\n",
581.                 res[i][0],del[i][0],res[i][1],del[i][1]);
582.         }
583.     }
584.     return (m);
585. }
586.
587. /*
588. double inp[8][5];
589. double der[8][2];

```

```

590. double res[13][5];
591.
592. input()
593. {
594.     extern double inp[8][5];
595.     extern double der[8][2];
596.     extern double res[13][5];
597.
598.     inp[i][j] : Matrix defines complex visibility function results
599.                derived from the closure results.(Rectangular co-ordinates).
600.
601.     inp[i][j] = enter visibility or error as defined below.
602.
603.     i      : 0 <= i <= 7 , as defined by inp[i][4] below.
604.     j = 0 : real component of complex visibility for ith baseline.
605.     j = 1 : img. component of complex visibility for ith baseline.
606.     j = 2 : estimated error for inp[i][0].
607.     j = 3 : estimated error for inp[i][1].
608.
609.     inp[0][4] = 0.0;
610.     inp[1][4] = 104;
611.     inp[2][4] = 143;
612.     inp[3][4] = 172;
613.     inp[4][4] = 247;
614.     inp[5][4] = 352;
615.     inp[6][4] = 600;
616.     inp[7][4] = 715;
617.
618.     der[i][j] : Matrix defines complex visibility results for baseline
619.                space gridded every 100 wavelengths; derived from graph
620.                of inp[i][j].(Rectangular co-ordinates).

```

621.

622.

der[i][j] = enter visibility as defined below.

623.

624.

i : 0 ≤ 7 ; baseline = 100i.

625.

j = 0 : real component of complex visibility for ith baseline.

626.

j = 1 : img. component of complex visibility for ith baseline.

627.

628.

res[i][j] : Matrix defines actual closure amplitude and closure phase

629.

results. (Polar co-ordinates).

630.

631.

res[i][j] = enter visibility or error as defined below.

632.

633.

i : as defined by res[i][j] below.

634.

j = 0 : real component of complex visibility for ith baseline.

635.

j = 1 : img. component of complex visibility for ith baseline.

636.

j = 2 : estimated error for res[i][0].

637.

j = 3 : estimated error for res[i][1].

638.

639.

res[0][j]= baseline = 44

640.

res[1][j]= baseline = 104

641.

res[2][j]= baseline = 172

642.

res[3][j]= baseline = 143

643.

res[4][j]= baseline = 247a

644.

res[5][j]= baseline = 247b

645.

res[6][j]= baseline = 352

646.

res[7][j]= baseline = 600

647.

res[8][j]= baseline = 715

648.

649.

res[1][4] = 104;

650.

res[2][4] = 143;

651.

res[3][4] = 172;

```
652.         res[4][4] = 247;
653.         res[5][4] = 352;
654.         res[6][4] = 600;
655.         res[7][4] = 715;
656.         res[8][4] = 44;
657.         res[9][4] = 60;
658.         res[10][4] = 67;
659.         res[11][4] = 76;
660.         res[12][4] = 115;
661.     }
662.
```

*/

REFERENCES

- ANDERSON B., LYNE A.G. and PECKHAM R.J., 1975, *Nature*, 258, 215.
- ARNETT W.D., 1975, *Astrophys. J.*, 195, 727.
- ASHWORTH W.B., 1980, *J. Hist. Astron.*, 11, 1.
- BAADE W. and MINKOWSKI R., 1954, *Astrophys. J.*, 119, 206.
- BAARS J.W.M., GENZEL R., PAULINY-TOTH I.I.K. and WITZEL A., 1977, *Astron. and Astrophys.*, 61, 99.
- BAARS J.W.M. and HARTSUIJKER A.P., 1972, *Astron. and Astrophys.*, 17, 172.
- BALDWIN J.E., JENNINGS J.E., SHAKESHAFT J.R., WARNER P.J., WILSON D.M.A. and WRIGHT M.C.H., 1970, *Mon. Not. R. astr. Soc.*, 150, 253.
- BELL A.R., 1977, *Mon. Not. R. astr. Soc.*, 179, 573.
- BELL A.R., 1978, *Mon. Not. R. astr. Soc.*, 182, 443.
- BELL A.R., GULL S.F. and KENDERDINE S., 1975, *Nature*, 257, 463.
- BEVINGTON P.R., 1969, *Data Reduction and Error Analysis for the Physical Sciences*, (Mc.Graw-Hill, New York).
- BRACEWELL R.N., 1958, *Proc. I.R.E.*, 46, 97.
- BRAUDE S.Ya., LEBEDEVA O.M., MEGN A.V., RYABOV B.P. and ZHOUCK I.N., 1969, *Mon. Not. R. astr. Soc.*, 143, 301.
- BRIDLE A.H. and CASWELL J.L., 1970, *Nature*, 225, 356.

- BYCHOV K.V., 1974, *Sov. Astron.*, 17, 577.
- CHEVALIER R.A., 1974, *Astrophys. J.*, 188, 501.
- CHEVALIER R.A., 1976, *Astrophys. J.*, 208, 826.
- CHEVALIER R.A. and KIRSHNER R.P., 1979, *Astrophys. J.*, 233, 154.
- CHEVALIER R.A., OEGERLE W.R. and SCOTT J.S., 1978, *Astrophys. J.*, 222, 527.
- COWSIK R., 1979, *Astrophys. J.*, 227, 856.
- COWSIK R. and SARKAR S., 1980, *Mon. Not. R. astr. Soc.*, 191, 855.
- DAVIES J.G. and LARGE M.I., 1970, *Mon. Not. R. astr. Soc.*, 149, 301.
- DICKEL J.R. and GREISEN E.W., 1979, *Astron. and Astrophys.*, 75, 44.
- ERICKSON W.C., KUIPER T.B.H., CLARK T.A., KNOWLES S.H. and BRODERICK J.J., 1972, *Astrophys. J.*, 177, 101.
- ERICKSON W.C. and PERLEY R.A., 1975, *Astrophys. J.*, 200, L83.
- EVANS D.S. and JESSOP G.R., 1976, *VHF/UHF Manual*, Ch. 7, (R.S.G.B., London).
- FABIAN A.C., WILLINGALE R., PYE J.P., MURRAY S.S. and FABBIANO G., 1980, *Mon. Not. R. astr. Soc.*, 193, 175.
- FEDORENKO V.N., 1979, *Sov. Astron.*, 23, 1235.
- FOMALONT E.B. and WRIGHT M.C.H., 1974, *Galactic and Extra-Galactic Radio Astron.*, eds. VERSCHUUR G.L. and KELLERMAN K.I., (Springer-Verlag, New York).

- HOGG D.E., 1974, Galactic and Extragalactic Radio Astron., eds. VERSCHUUR G.L. and KELLERMAN K.I., (Springer-Verlag, New York).
- HOGG D.E., MACDONALD G.H., CONWAY R.G. and WADE C.M., 1969, Astron. J., 74, 1206.
- HOLT S.S., BOLDT E.A., SERLEMITSOS P.J. and BRISKEN A.F., 1973, Astrophys. J., 180, L69.
- HOROWITZ P., PAPALIOLIOS C., and CARLETON N.P., 1971, Astrophys. J., 163, L5.
- HUTTON L.K., CLARK T.A. and CRONYN W.M., 1973, Bull. Am. astr. Soc., 5, 35.
- HUTTON L.K., CLARK T.A., ERICKSON W.C., RESCH G.M., VANDENBERG N.R., KNOWLES S.H. and YOUMANS A.B., 1974, Astrophys. J., 79, 1248.
- JENNISON R.C., 1953, Ph.D. Thesis, University of Manchester.
- JENNISON R.C., 1958, Mon. Not. R. astr. Soc., 118, 276.
- JENNISON R.C., 1959, 9th IAU Symp. - URSI Symp., 1, 309, (Stanford Press).
- JENNISON R.C., 1965, Nature, 207, 740.
- JENNISON R.C. and DAS GUPTA M.K., 1956, Phil. Mag. Series 8, 1, 65.
- JENNISON R.C. and LATHAM V., 1959, Mon. Not. R. astr. Soc., 119, 174.
- KAMPER K., 1980, Observatory, 100, 3.
- KAMPER K. and VAN DER BERGH S., 1976, Astrophys. J. Suppl. Series, 32, 351.

- KAPLAN S.A. and PIKELNER S.B., 1970, The Interstellar Medium, Ch. 4, (Harvard University Press).
- KRAUSS J.D., 1966, Radio Astronomy, (Mc Graw-Hill, New York).
- LATHAM V., 1957, Ph.D. Thesis, University of Manchester.
- LEQUEUX J., 1962, Annales d' Astrophys., 25, 221.
- MARTIN B.R., 1971, Statistics for Physicists, (Academic Press, London).
- MATHESON D.N., 1973, Ph.D. Thesis, University of Kent.
- MATHESON D.N., 1974, Observatory, 94, 181.
- MEISEL D.P., 1978, Astron. J., 83, 538.
- MILNE D.K., GOSS W.M., HAYNES R.F., WELLINGTON K.J., CASWELL J.L. and SKELLERN D.J., 1979, Mon. Not. R. astr. Soc., 188, 437.
- MINKOWSKI R., 1959, 9th. IAU Symp. - URSI Symp., 1, 315, (Stanford Press).
- MINKOWSKI R., 1968, Nebulae and Interstellar Gas, eds. MIDDLEHURST B. and ALLER L., (University of Chicago Press).
- MURRAY S.S., FABBIANO G., FABIAN A.C., EPSTEIN A. and GIACONNI R., 1979, Astrophys. J., 234, L69.
- NORRIS B. (ed.), 1976, MOS and Special Purpose Bipolar I.C. and R.F. Power Transistor Circuit Design, 113, (McGraw-Hill, New York).
- PACHOLCZYK A.G., 1970, Radio Astrophys., (Freeman and Co., San Francisco).

- PARKER E.A., 1968, Mon. Not. R. astr. Soc., 138, 407.
- PEIMBERT M. and VAN DER BERGH S., 1971, Astrophys. J.,
167, 223.
- PETERSON F.W., 1976, Astrophys. J., 210, 723.
- PRENTICE A.J.R., 1970, Nature, 225, 438.
- READ P.L., 1977i, Mon. Not. R. astr. Soc., 178, 259.
- READ P.L., 1977ii, Mon. Not. R. astr. Soc., 181, 63P.
- READHEAD A.C.S. and WILKINSON P.N., 1978, Astrophys. J.,
223, 25.
- READHEAD A.C.S., WALKER R.C., PEARSON T.J. and COHEN M.H.,
1980, Nature, 285, 137.
- REIFENSTEIN III E.C., BRUNDAGE N.D. and STAELIN D.H.,
1969, Astrophys. J., 156, L125.
- RHODES W.T. and GOODMAN J.W., 1973, J. opt. Soc. Am.,
63, 647.
- ROGERS A.E.E., HINTEREGGER H.F., WHITNEY A.R., COUNSELMAN C.C.,
SHAPIRO I.I., WITTELS J.J., KLEMPERER W.K., WARNOCK W.W.,
CLARK T.A., HUTTON L.K., MARANDINO G.E., RÖNNÄNG B.O.
and RYDBECK O.E.H., 1974, Astrophys. J., 193, 293.
- ROGSTAD D.H., 1968, Applied Optics, 7, 585.
- ROSENBERG I., 1970i, Mon. Not. R. astr. Soc., 147, 215.
- ROSENBERG I., 1970ii, Mon. Not. R. astr. Soc., 151, 109.
- RYLE M., ELSMORE B. and NEVILLE A.C., 1965, Nature, 205, 1259.
- SCOTT P.F., SHAKESHAFT J.R. and SMITH M.A., 1969, Nature,
223, 1139.

SHKLOVSKY I.S., 1979, Nature, 279, 703.

SLEE O.B. and WRAITH P.K., 1967, Nature, 214, 971.

SLINGO A., 1974, Mon. Not. R. astr. Soc., 168, 307.

STROM R.G. and DUIN R.M., 1973, Astron. and Astrophys.,
25, 351.

SWENSON G.W., 1969, Ann. Rev. Astron. and Astrophys.,
7, 353.

TWISS R.Q., CARTER A.W.L. and LITTLE A.G., 1960, Observatory,
80, 153.

TWISS R.Q., CARTER A.W.L. and LITTLE A.G., 1962,
Aust. J. of Physics, 15, 378.

VAN DER BERGH S., 1971, Astrophys. J., 165, 457.

VAN DER BERGH S. and DODD W.W., 1970, Astrophys. J., 162, 485.

VAN DER BERGH S., MARSCHER A.P. and TERZIAN Y., 1973,
Astrophys. J. Suppl. Series, 26, 19.

VINER M.R., 1975, Astron. J., 80, 83.

WILKINSON P.N., READHEAD A.C.S., ANDERSON B. and PURCELL G.H.,
1979, Astrophys. J., 232, 365.

WINTER A.J.B., WILSON D.M.A., WARNER P.J., WALDRAM E.M.,
ROUTLEDGE D., NICOL A.T., BOYSEN R.C., BLY D.W.J. and
BALDWIN J.E., 1980, Mon. Not. R. astr. Soc., 192, 931.

WITTELS J.J., SHAPIRO I.I., COTTON W.D., COUNSELMAN C.C.,
HINTEREGGER H.F., KNIGHT C.A., ROGERS A.E.E.,
WHITNEY A.R., CLARK T.A., HUTTON L.K., NIELL A.E.,
RÖNNÄNG B.O. and RYDBECK O.E.H., 1976, Astron. J.,
81, 933.

